國 立 交 通 大 學

材料科學與工程學系

碩 士 論 文

電鍍氧化亞銅經退火處理於光解水製氫應用之探討

Effect of Annealing on the Electrodeposited Cu_2O Films for Photoelectrochemical Hydrogen Generation

研 究 生：梁茹夢

指導教授：林　鵬 教授

吳樸偉 教授

中華民國九十八年七月

電鍍氧化亞銅經退火處理於光解水製氫應用之探討

Effect of Annealing on the Electrodeposited Cu_2O Films for Photoelectrochemical Hydrogen Generation

研究生： 梁茹夢　　Student： Ru-Meng Liang

指導教授： 林　鵬　教授　　Advisor： Dr. Pang Lin

吳樸偉　教授　　Dr. Pu-Wei Wu

國立交通大學

材料科學與工程研究所

碩士論文

A Thesis
Submitted to Department of Material Science and Engineering
College of Engineering
National Chiao Tung University
in Partial Fulfillment of Requirements for
the Degree of Master
in Material Science and Engineering
July 2009
Hsin-Chu, Taiwan, Repubic of China

中華民國九十八年七月

電鍍氧化亞銅經退火處理於光解水製氫應用之探討

學生：梁茹夢　　指導教授：林　鵬 博士

吳樸偉 博士

國立交通大學 材料科學與工程研究所

中文摘要

本研究利用電化學沉積法沉積氧化亞銅薄膜，由控制鍍液酸鹼值、沉積時間及過電位大小來控制氧化亞銅薄膜的成長。在 pH 值為 9 的鍍液中能得到擇優方向以(200)方向為主的結構，pH 值為 11 的鍍液中則能得到擇優方向為(111)方向的結構。取其中以 pH 值為 9 的鍍液，過電位為-0.3 V，電鍍時間為 100 分鐘的薄膜，以及 pH 值為 11 的鍍液，過電位為-0.3 V，電鍍時間為 60 分鐘的薄膜作為研究其退火影響的對象。

退火溫度為 150、200、250、300、350 ℃等五個溫度，持溫時間分別為 10、30 及 60 分鐘。兩種不同擇優方向的薄膜在其樣貌形狀上皆產生了晶粒變小的變化，但其電阻值則呈現兩種相反的趨勢。在擇優方向為(200)方向的薄膜，其電阻值隨著溫度的上升及持溫時間的延長，皆有下降的趨勢。相反的，在擇優方向為(111)方向的薄膜，其電阻值隨著溫度的上升及持溫時間的延長，皆有些微增加的趨勢。再經由 350 ℃ 退火 30 分鐘的處理後，擇優方向為(200)方向的薄膜其電阻值由 1.602 Ωcm大幅下降至 3.96E-4 Ωcm。

最後分別研究不同退火條件對於氧化亞銅薄膜的光電性質的影響，以 Photoelectrochemical solar cell (PEC)量測其光電流造氫的表現。結果兩種擇優方向的膜薄都以在 350 ℃ 退火 60 分鐘的處理後，能有最佳的光電轉換造氫效率。擇優方向為(200)方向的薄膜，其最佳光電流表現為-141 μA cm^{-2}；擇優方向為(111)方向的薄膜，其最佳光電流表現為-119 μA cm^{-2}。退火對其光電轉換造氫效率的影響，主要反映出退火處理後其導電度的變化，結果證明退火處理能增進半導體薄膜的結晶性與導電度，而能得到較好的光電表現。

Effect of Annealing on the Electrodeposited Cu_2O Films for Photoelectrochemical Hydrogen Generation

Student: Ru-Meng Liang

Advisor: Dr. Pang Lin
Dr. Pu-Wei Wu

Department of Materials Science and Engineering
National Chiao Tung University

Abstract

The Cu_2O films were electrodeposited in two different pH values of plating bath. We controlled the deposition times and overpotentials to study the growth of Cu_2O films. The film deposited in pH 9 bath demonstrated a preferred orientation in (200) plane, and in pH 11 bath revealed a preferred orientation of (111). The film deposited in pH 9 bath under -0.3 V for 100 min and the film deposited in pH 11 bath under -0.3 V for 60 min were used to study the annealing effect.

The annealing temperatures were 150, 200, 250, 300, and 350 ℃, and the annealing times were 10, 30, and 60 min. The grain sizes for these two films were both decreased after annealing. However, their resistivity exhibited an opposite direction. The pH 9 films after annealing revealed a reduced resistivity as the temperature and annealing time were increased. On the other hand, the pH 11 films after annealing showed increased as the temperature and annealing time were increased. The pH 9 film after annealing at 350 ℃ for 30 min demonstrated a stable resistivity reduction decreased from 1.602 to 3.96E-4 Ω ㎝.

We studied the photoelectrochemical properties of Cu_2O film for H_2 generation before and after annealing process. The photocurrents were collected to explore the effect of annealing. The results indicated that both films had best performance at 350 ℃ annealing for 60 min. The photocurrent of pH 9 film annealed at 350 ℃ for 60 min was -141 μA $㎝^{-2}$, and the pH 11 film annealed at 350 ℃ for 60 min was -119 μA $㎝^{-2}$. The photocurrents revealed the resistivity transition of Cu_2O films which was affected by the annealing process. The results exhibited that the annealing process could improve the crystallinity and was greatly enhanced conductivity of Cu_2O film. As a result, enhanced the photoelectrochemical performance.

Acknowledgements

終於完成了！努力奮鬥了兩年，能拿出來見人的成果竟是這麼薄薄的一本，研究真的是一件深不見底事情啊！學習了很多東西卻總是還覺得不夠，想了很多卻永遠有思慮不周的地方，而實驗永遠都有未知的事物等著我們去了解，時常覺得頭痛，回想起來卻總有令人開心的地方。從化學系一路走到這裡，這兩年來在生活、研究上跌跌撞撞學習了好多。感謝林鵬教授與吳樸偉教授兩年來給我的教導，對我的耐心與關心，並充分的給予我設計與進行實驗上的自由，讓我對於研究與未來都有了新的想法與期許。感謝高嘉駿、林映眉、葉耕余學長姐在生活及實驗上給我的支持與關心，即使畢業了也還回來督促我替我打氣。感謝張雲閔、謝育淇、黃苡叡、謝怡凡、林勝結各位大學長們給我許多建議及實驗上的幫助，總能幫助我從不同的角度切入來思考問題，在你們身上學習到了許多經驗及知識是我進步的捷徑。以及致源與詠策在實驗與生活上的給我協助與包容，還有貼心的于凡、立忠、儷曄、儷尹，謝謝各位學弟妹們帶來的歡笑與趣事。最重要的是與我一路相伴努力的戰友兼貴人們，瀠方、佑慈、境妤、俊翰、佳勳與哲毅，謝謝你們的鼓勵與幫助，總是要先安撫我的抱怨與牢騷，還要再提供我繼續向前的動力，不論在實驗或精神上都是我動力的來源。還有許多幕後的貴人好友們，謝謝郁璇、立筠、妍如、大銘、暐翰、于政、昀錚以及許多朋友的朋友，還有台大化工所的佩吟。最後是永遠愛我支持我的家人，親愛的爸媽謝謝你們，我愛你們。

也許研究的本身並不有趣，知識也沒有學完的一天，有趣的是能認識你們這群實事求是、認真開朗、聰明貼心的朋友，與你們討論切磋、互相學習，才是豐富這研究生活的來源。相信科技始終來自於人性，與你們認識，讓我相信未來會愈來愈好，謝謝你們的愛與力量，在下個階段裡繼續努力吧！

Table of contents

List of Figures

List of tables

Chapter 1

Introduction

1.1. Materials Characteristics of Cuprous Oxide

Cuprous oxide has been receiving attention as a semiconductor material since the invention of Cu_2O rectifier by Grondhal in 1920s [1]. Since then, considerable progress were made on Cu_2O characterization from 1930 to 1940. To date, the Cu_2O is still of potential interests in application of homojuction solar cells, heterojuction solar cells, and photoelectrochemical (PEC) cells.

Cu_2O is a relatively stable compound that is insoluble in organic solvent and water. However, it can be dissolved in dilute acid such as nitric acid and sulfuric acid to form copper nitrate and copper sulfate. In addition, the Cu_2O can also be dissolved in concentrated ammonia solution to form colorless $[Cu(NH_3)_2]^+$, which easily oxidizes in air becoming blue $[Cu(NH_3)_4(H_2O)_2]^{2+}$.

Cu_2O is known as a p-type semiconductor with a direct band gap about 2 eV. The p-type character is due to copper vacancies in the Cu_2O structure. The resistivity of Cu_2O depends on its synthetic routes. For example, resistivity value which has been reported in literature varies from a few Ω・cm to 10^4 Ω・cm. The crystal structure of Cu_2O is shown in Fig 1.1. With a lattice constant of 4.27 Å, the oxygen anions are located at the body-centered sites and the copper cations are at the face-centered sites. The theoretical density and melting point of the Cu_2O were 6.0 gcm^{-3} and the is 1235℃, respectively.

1.2. Motivation

Cu_2O is a promising material for applications in photovoltaic devices since its theoretic solar energy conversion efficiency was estimated up to 18%. However, the highest conversion efficiency reported so far is a modest 2% [32]. This reduced value is attributed to the poor crystallinity in conjunction with numerous defects present in the Cu_2O structure.

In this research, we electrodeposited Cu_2O films under different pH values, potentials, and deposition times. Next, we attempted to improve the photoelectrochemical performance of for hydrogen generation by a post-annealing process with the aim to reduce the inherent defects. Afterward, we recorded the properties for solar energy conversion using a simple photoelectrochemical measurement in hydrogen evolution.

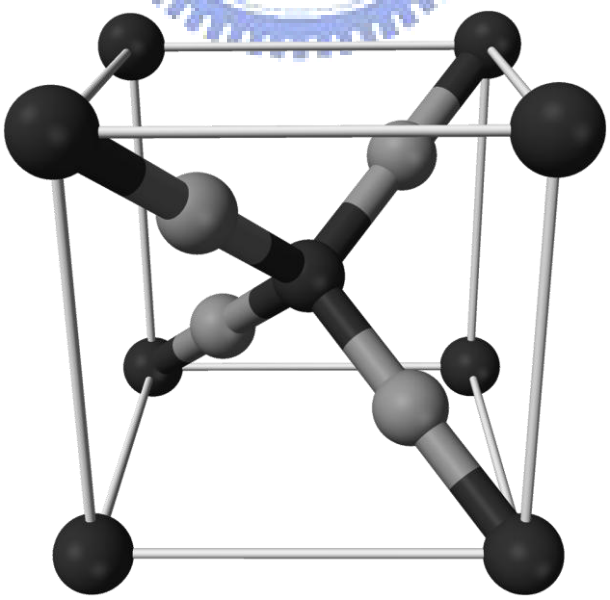

Figure 1.1 A schematic of crystal structure of cubic Cu_2O. The dark atoms are O and the remaining ones are Cu atoms.

Chapter 2

Literature Review

2.1. Fabrication of Cu_2O

2.1.1. Method of Chemical Synthesis

Fabrication of semiconducting nanoparticles has attracted significant attention these years for their unique chemical and physical properties. Various routes have been developed to synthesize narrow-sized, well-distributed, highly crystalline particles with a variety of morphologies. We are interested in the Cu_2O due to its self-assembling character, and its potential application in solar energy conversion. A typical chemical synthetic route for the Cu_2O listed below;

$$Cu^{2+}_{(aq)} + 2OH^{-}_{(aq)} \rightarrow Cu(OH)_{2(s)} \quad (1)$$

$$2Cu(OH)_{2(s)} + 2e^{-} \rightarrow Cu_2O_{(s)} + H_2O_{(l)} \quad (2)$$

Copper ions often form copper hydroxide first in an alkaline electrolyte, and then reduced by a reducing agent (L-ascorbic acid, hydrazine). There are many factors that might affect the crystal growth of Cu_2O. For example, a well-known determinant is the surfactant. Others variables including pH, processing step, and reducing agent also play certain roles. So far, various Cu_2O structures including spheres, cubes, octahetras, and wires have been synthesized [2-22]. A brief summary on their synthesis work is provided below.

A. Nanosphere

The Cu_2O exhibits a direct band-gap of 2 eV. It is known that the quantum size effects on the optical properties of indirect band-gap semiconductor are significantly different from that of direct band-gap one. Previously, Yin *et al.* were interested in the size effect of Cu_2O on its optoelectronic properties [2]. In 2005, they synthesized well-defined Cu_2O nanocrystals with the diameter varied from 3.6 to 10.7 nm (Fig 2.1a). They used a hydrothermal method and the reaction was initiated by two separate steps. Copper acetate, oleic acid, trioctylamine, and hexane were used as precursors and their process is shown in Fig 2.1b. The synthesized nanocrystals displayed a band gap transition attributed to the presence of CuO monolayer shell. The transition was observed to reveal a blue-shift as a function of decreasing particle size.

Similarly, Li *et al.* synthesized the Cu_2O nanospheres using copper acetate as a precursor, and $NaBH_4$ as a reducing agent in a DMF solvent [3]. The reaction temperature was about 80~90 ℃ and the resulting Cu_2O nanospheres were in diameter of 200 nm. In following gas sensor application (Fig 2.2), their results indicated that the Cu_2O nanospheres were a better gas sensor for flammable gas than CuO and Cu_2O in octahedral shapes at a reaction temperature of 210 ℃. It was concluded that the surface of Cu_2O was converted to Cu_2O_{2-x}, an active state in high temperature that makes it more active than CuO. Moreover, it is likely that the stacking arrangement of spherical structure engendered a larger surface area that delivers a higher performance.

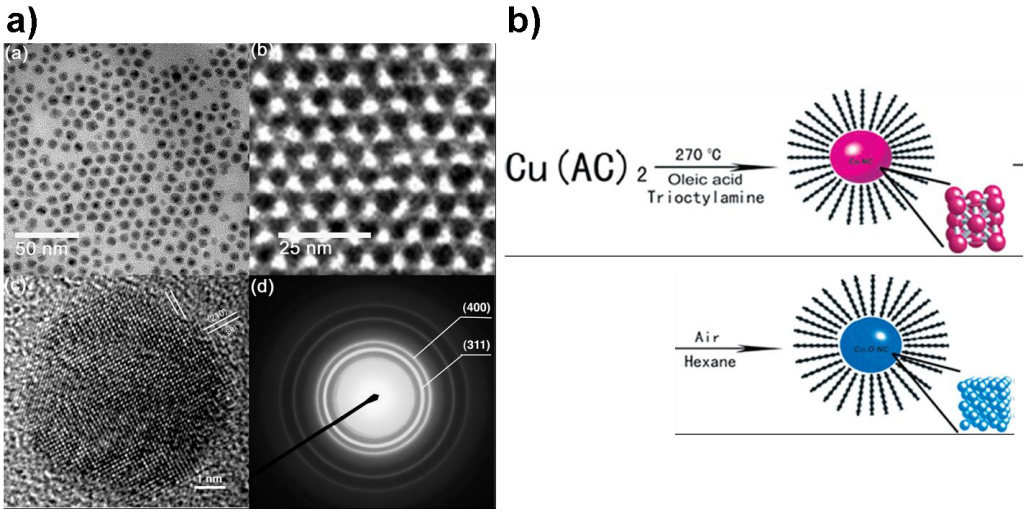

Figure 2.1 a) TEM images of self-assembled 6 nm diameter Cu_2O nanocrystals, b) synthetic procedure for Cu_2O nanocrystals [2].

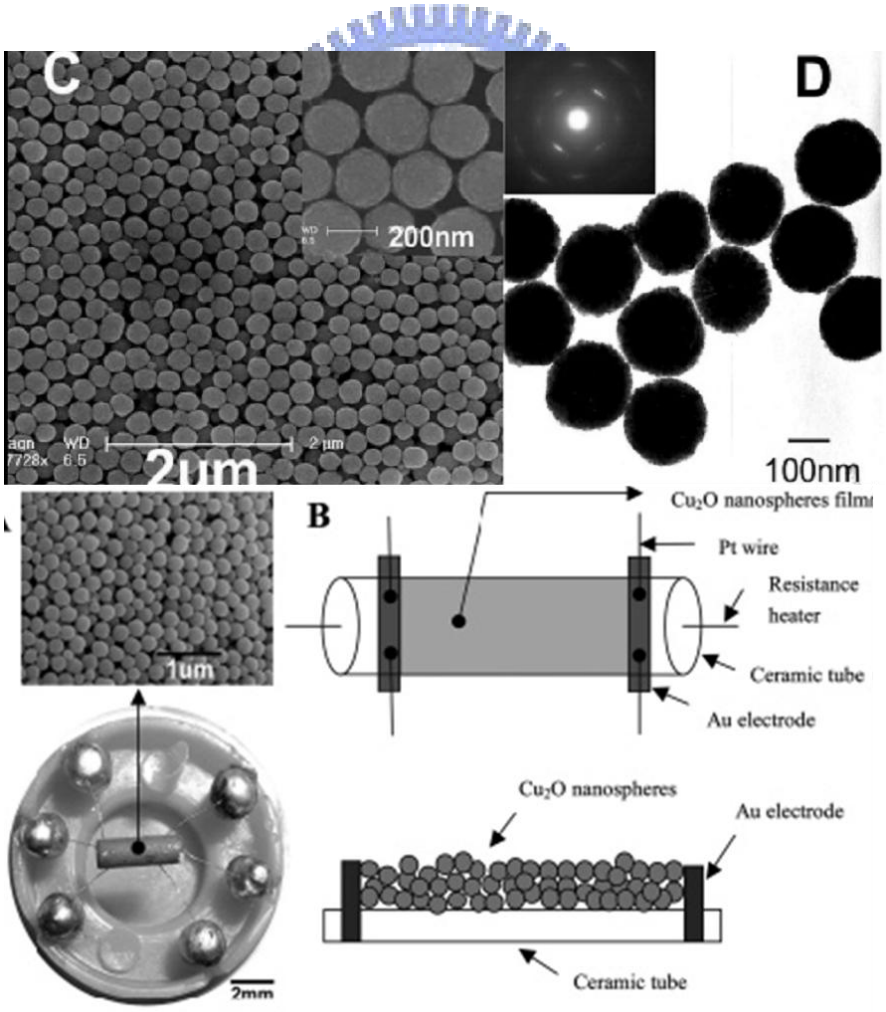

Figure 2.2 SEM images of Cu_2O nanocrystals and gas sensor system [3].

B. Nanocubes

In 2003, Murphy *et al.* synthesized the Cu_2O nanocubes using polyethylene glycol (PEG) as a surfactant [4]. They discussed the effect of synthesis steps and surfactant concentration. Their results indicated the procedure which mixed copper sulfate and PEG600 first, followed by addition of NaOH and ascorbic acid was leading to desirable uniformity and monodispersity. In addition, the cubic size was proportional to the surfactant concentration in a range of 25 to 200 nm.

Hung *et al.* adopted a seed-mediated synthesis approach to control the size of Cu_2O nanocubes in 2007 [5]. The surfactant employed was sodium dodecyl sulfate (SDS). The cubic size was controlled by aggregation of Cu_2O seed particles, and the size range could be adjusted from 40 to 420 nm with a rather high yield (Fig 2.3).

Chang *et al.* synthesized nanocubes of 28 nm in edge length by a simple one-pot route in 2008 [6]. They used fructose as both the stabilizer and weak reducing agent, which would first form Cu-fructose complexes. Subsequently, the complex was reduced to CuOH-fructose complexes at a higher pH. Then the complex was reduced further by L-ascorbic acid to form Cu_2O nanocubes. They observed that small Cu_2O nanocubes exhibited a hollow structure at first, and then the hollow structure was filled when the reaction time progressed longer. The Cu_2O nanoparticles filled the holes through typical Ostwald ripening behavior and relevant images shown in Fig 2.4

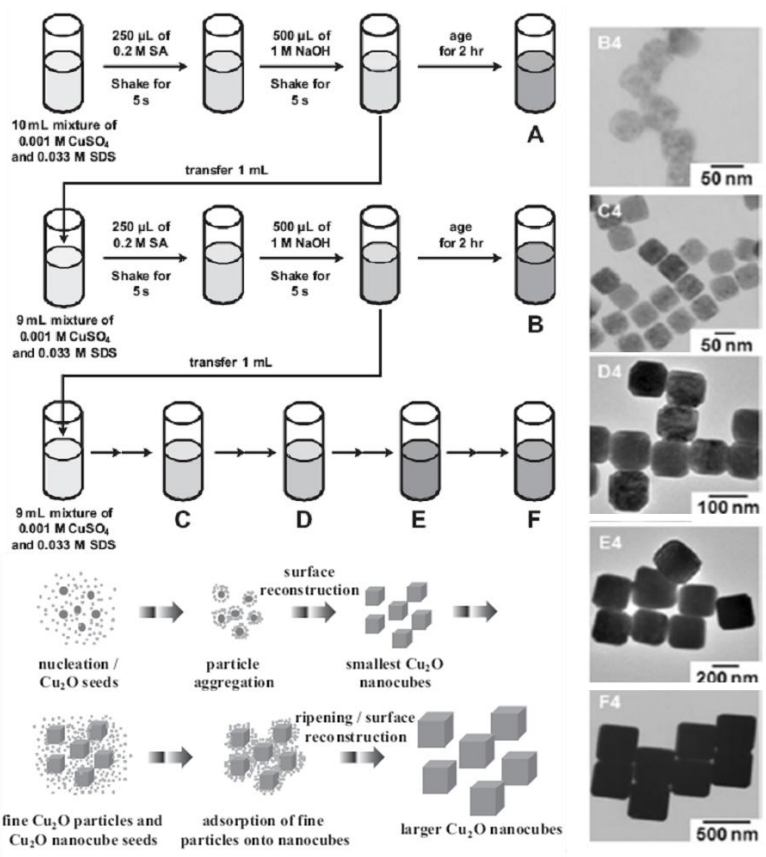

Figure 2.3 A schematic illustration of the procedure used to grow Cu_2O nanocubes and related crystal growth process [5].

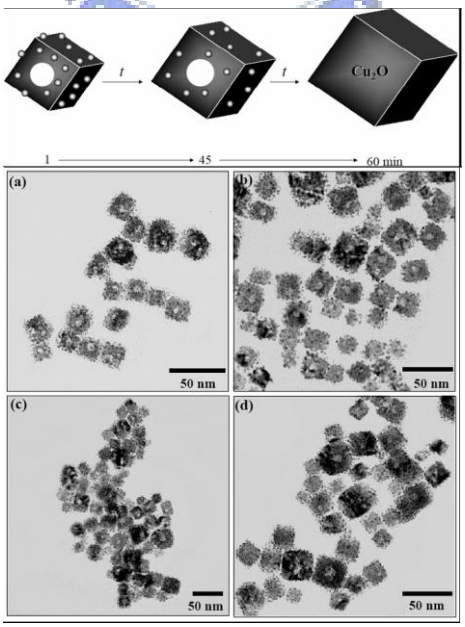

Figure 2.4 A schematic illustration of the formation of Cu_2O nanocubes from hollow to filled structures and corresponding SEM images [6].

C. Octahedrons

Shen *et al.* prepared the monodispersed Cu_2O octahedron nanocrystals with size varying from 45 to 95 nm (Fig 2.5) [7]. They reduced the copper nitrate in a Triton X-100 water-in-oil microemulsion by γ-irradiation. The Triton X-100 provided a stable environment allowing the reaction to take place without any pH adjustment.

Wang *et al.* synthesized the Cu_2O octahedron without adding surfactants or the assistance of organic compounds [8]. They found that adding NH_3 solution would affect the ratio for the growth rate along the <111> versus the <100> direction, which influenced the morphology of the product. The morphology was controlled by adjusting the ratio of NH_3 to Cu^{2+}, and distinct shapes such as spherical, porous spherical, cubic, and octahedral were obtained.

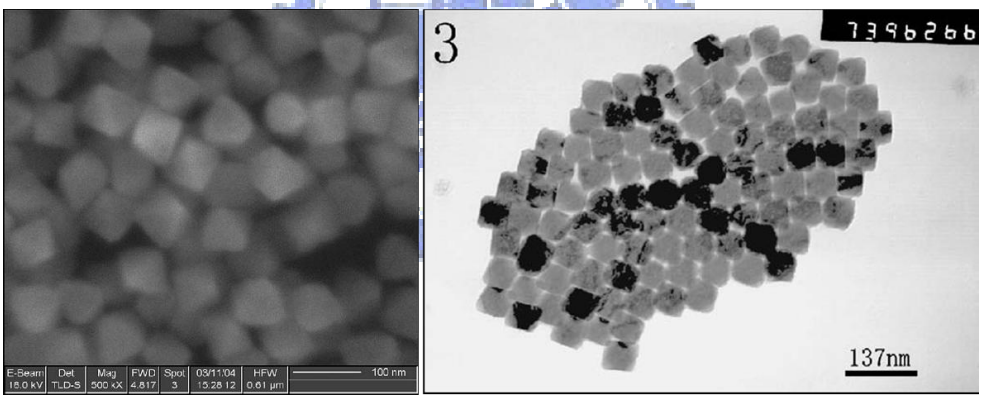

Figure 2.5 SEM image and TEM image of octahedral Cu_2O reduced by γ-irradiation in Triton X-100 [7].

D. Nanowires, Nanotubes

Wang *et al.* used a simple chemical route to synthesize the Cu_2O nanowires with a rather high yield [9]. The PEG20000 was used as a surfactant, and hydrazine was

used as a reducing agent. The reaction proceeded under constant stirring for entire time. The nanowires were 10 to 20 µm long, and their diameters were about 5 to 8 nm (Fig 2.6). Hence, the nanowires exhibited a high aspect ratio.

Hu *et al.* used cetyltrimethylammonium bromide (CTAB) as a surfactant [10]. The $Cu(OH)_4^{2-}$ precursor was selectively reduced by various methods to synthesize Cu, Cu_2O, and CuO nanotubes. The Cu and Cu_2O were reduced by a hydrazine and glucose respectively, and the CuO was reduced by a hydrothermal method. As the concentration of $Cu(OH)_4^{2-}$ was increased, the nanotubes became nanorodes with a solid structure. The TEM images for nanotubes and nanorodes of Cu, Cu_2O, and CuO are shown in Fig 2.7.

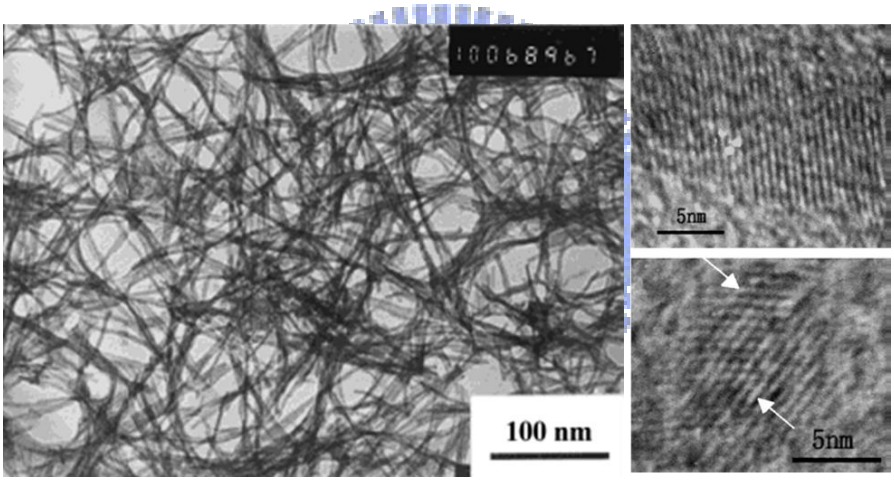

Figure 2.6 TEM images of Cu_2O nanowires [9].

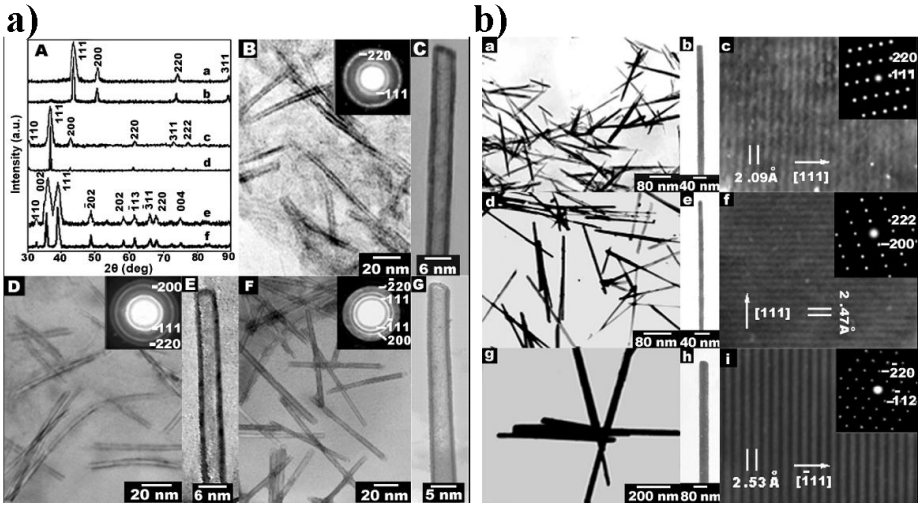

Figure 2.7 TEM images of a) nanotubes and b) nanorodes [10].

2.1.2. Method of Electrodeposition [11-12]

There are many methods to prepare Cu_2O thin films. For example, physical vapor deposition (e.g., thermal evaporation, sputtering), chemical vapor deposition (CVD), and electrochemical deposition have been studied extensively. Among them, the electrodeposition is the most attractive approach. Electrodeposition is a versatile and low-cost technique for preparing thin films of oxide semiconductors. It is possible to grow uniform thin film over large areas in unique shape. Fabrication of Cu_2O films by the electrochemical method has been successfully developed.

A. Cathodic Electrodeposition in Cuprous Oxides

Cathodic deposition of Cu_2O has been extensively studied before. It is established that electrochemical deposition is able to adjust precisely the driving force for the reaction involved in deposition. This allows the control of structure and phase composition of the resulting films. Many different electrodeposition environments, substrates, and power supply methods have been explored. It is recognized that changing these conditions would alter structure, morphology, and photoelectro-chemical properties of Cu_2O.

A commonly used bath was developed in 1987 by Rakhshoni *et al*, in which copper sulfide, lactic acid, and sodium hydroxide were used [12]. The Cu_2O films were electrodeposited successfully under galvanostatic conditions on stainless steel cathodes. It was shown that uniformly oriented Cu_2O films could be grown with robust adhesion.

The pH environment is recognized to critically influence the principal reaction route of electrodeposited Cu_2O film. The reactions steps involved for the cathodic

deposition of Cu_2O are [13];

$$2Cu^{2+}_{(aq)} + 2e^- + H_2O_{(l)} \rightarrow Cu_2O_{(s)} + 2H^+_{(aq)} \quad (3)$$

$$Cu^{2+}_{(aq)} + 2e^- \rightarrow 2Cu_{(s)} \quad (4)$$

$$Cu_2O_{(s)} + 2e^- + 2H^+_{(aq)} \rightarrow 2Cu_{(s)} + H_2O_{(l)} \quad (5)$$

Reaction (3) and (5) are pH-dependent. It is known that the Cu_2O would dissolve to copper(II) or reduce to copper metal in an acid environment.

In 1998, Switzes *et al.* identified a stable ratio of copper lactic solution, which contained 0.4 M cuprous sulfate and 3 M lactic acid [13]. The pH for the plating bath could be adjusted from 7 to 12. The copper ion would be stabilized by the lactic acid to form $Cu(CH_3CHOHCOO)_2$. As a result, it would not precipitate out in high pH environments. Potentiostatic and galvanostatic depositions both confirmed that the preferential orientation of Cu_2O film was [100] in a pH 9 bath, and [111] in a bath whose pH value was above 10 (Fig 2.8).

Cu_2O had been electrodeposited on several substrates including Cu, InP (001), ITO, Si, and stainless steel [14-15]. The out-of-plane orientation of film deposited on a polycrystalline substrate depended on the solution pH, and was only slightly affected by the single crystal substrate [16].

Wang *et al.* carefully examined the effect of pH value on the resulting crystal growth [17]. They observed a new preferred orientation, which is the (110) of Cu_2O. They concluded that the film could be obtained in a narrow pH range from 9.4 to 9.9 (Fig 2.9).

Lee *et al.* electrodeposited the Cu_2O film in a weak acidic electrolyte of 10 mM $Cu(NO_3)_2$ by a constant current mode [18]. Their results confirmed that the Cu_2O and

Cu were deposited simultaneously. Formation mechanism of Cu_2O was investigated by electrochemical analysis utilizing an electrochemical quartz crystal microbalance (EQCM). The superimposition of anodic current and mass change data suggested that the Cu exhibited a lower dissolution overpotential. Therefore, they supplied an anodic current to selectively dissolve the Cu, and obtained a pure Cu_2O film afterward. Their results provided a different preparation route for pure Cu_2O phase.

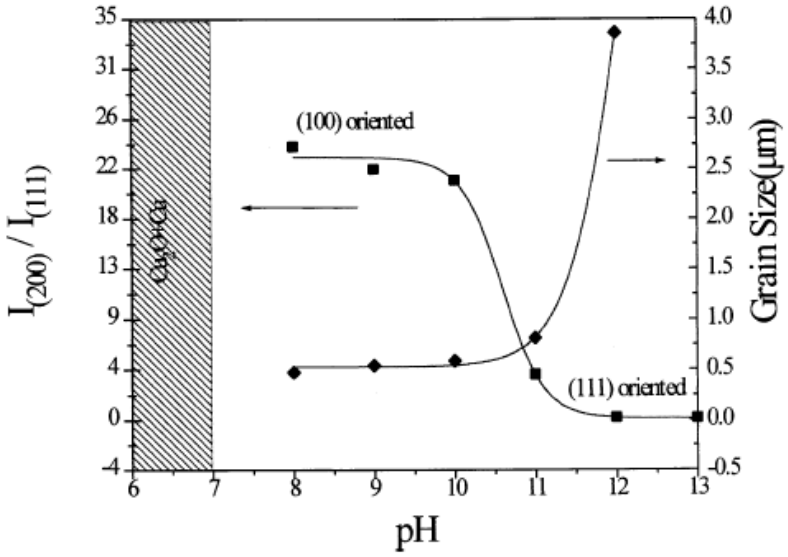

Figure 2.8 Plot of relative intensity ($I_{(200)}/I_{(111)}$) and grain size as a function of bath pH, the applied potential is -0.4 V vs. SCE, and the bath temperature is 60 ℃ on a stainless steel substrate [13].

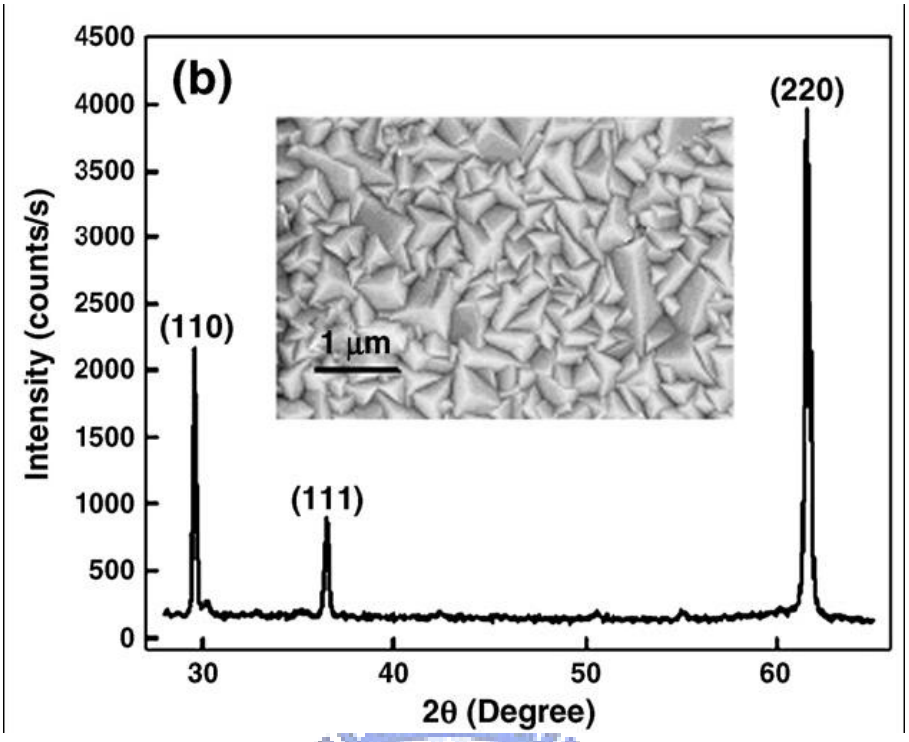

Figure 2.9 XRD of (110) oriented Cu_2O film and corresponding SEM image [17].

B. Morphology Controlled by Electrodeposition

In 2002, Huang *et al.* synthesized the Cu_2O nanowires by electrodeposition from a lyotropic reverse hexagonal liquid crystalline phase, which was used as a soft template [19]. The liquid crystalline phase was polarized, and aligned in an electric field. Its alignment could be further improved by controlling the distance between the electrodes. The deposited Cu_2O nanowires had a diameter ranging from 25 to 100 nm with a high aspect ratio (Fig 2.10).

In 2004, Choi *et al.* pointed out that the shape of a crystal was determined by the crystallographic planes on its surface [20]. They used an additive, sodium dodecyl sulfate (SDS), in order to tailor the crystal habits of electrochemically grown Cu_2O crystals. The SDS was preferentially adsorbed onto {111} faces, and impeded the

crystal growth alone the <111> direction. Its growth process is shown in Fig 2.11. Furthermore, the preferential adsorption of SDS was pH-dependence, which enabled selective tuning for the growth rate of Cu_2O crystals along the <111> directions.

In 2005, they further demonstrated a systematic and simultaneous tuning of the habit and degree of branching in the Cu_2O crystals by manipulating certain key conditions, such as electrodeposited voltage, current, temperature, and composition of the solution [21]. The deposition potential-current diagram, as shown in Fig 2.12, summarizes the effect of electrochemical conditions on branching and faceted growth of Cu_2O crystals. The crystal growth could be precisely controlled by adjusting the preference for branching or faceting growth conditions through suitable electrodeposition methods. In such way, the crystal shape could be designed and reproduced.

Adding different additives engendered a distinct preferential adsorption effect. The additives include surfactants, polymers, and specific ions. Choi *et al.* had studied the pre-grown crystals carefully in 2006 [22]. Different ions exhibited various adsorbing strengths. By adjusting the additives, the growth process could be totally reversed (Fig 2.13). Wang *et al.* studied the additives effect by adding different amounts of CTAB and cations. The structure for the bulk Cu_2O film was also affected by the additives (Fig 2.14) [23].

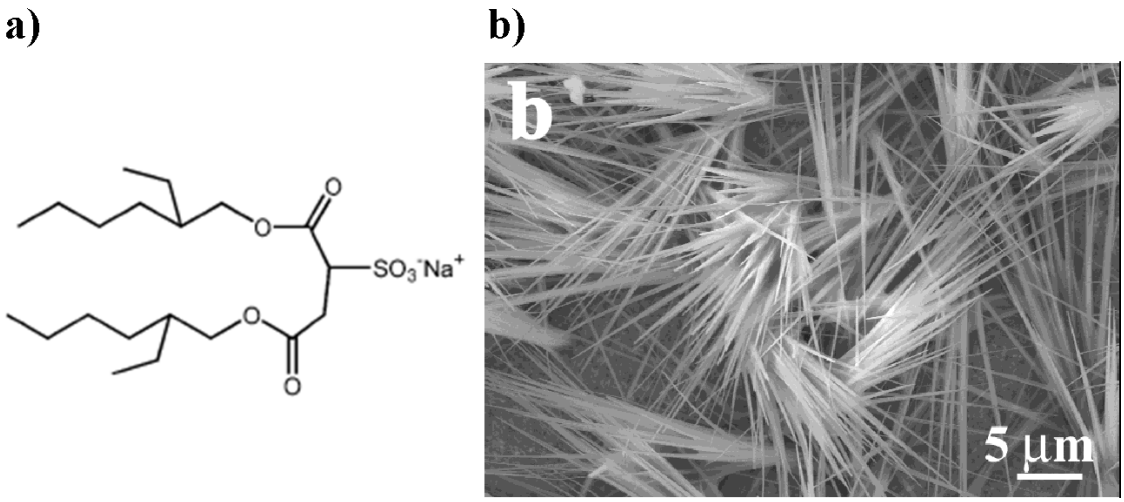

Figure 2.10 a) Structure of surfactant AOT molecule, and b) SEM image of electro-deposited Cu_2O wires [19].

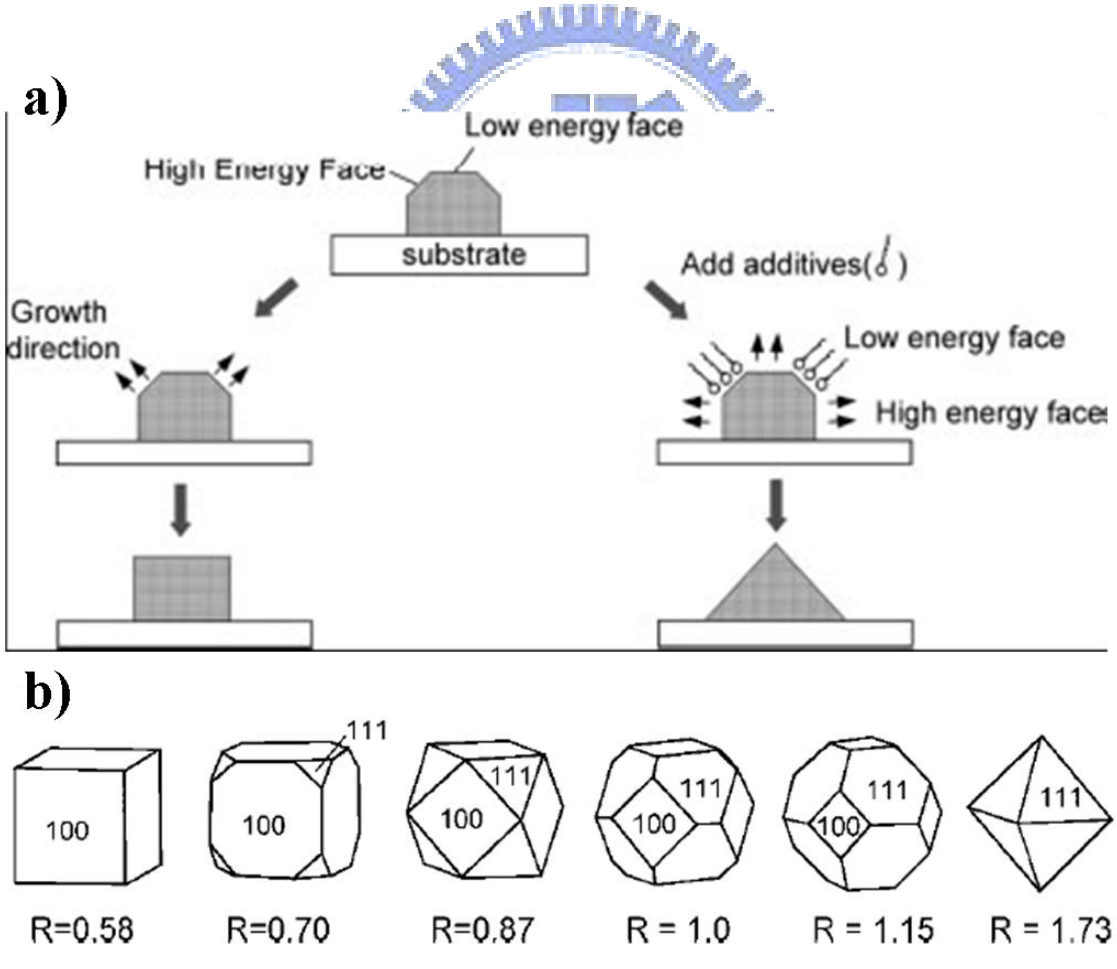

Figure 2.11 a) The scheme of crystal-habit control achieved by preferential orientation adsorption of additives during the crystal growth process and b) crystal shape evolution from cubic to octahedral [20].

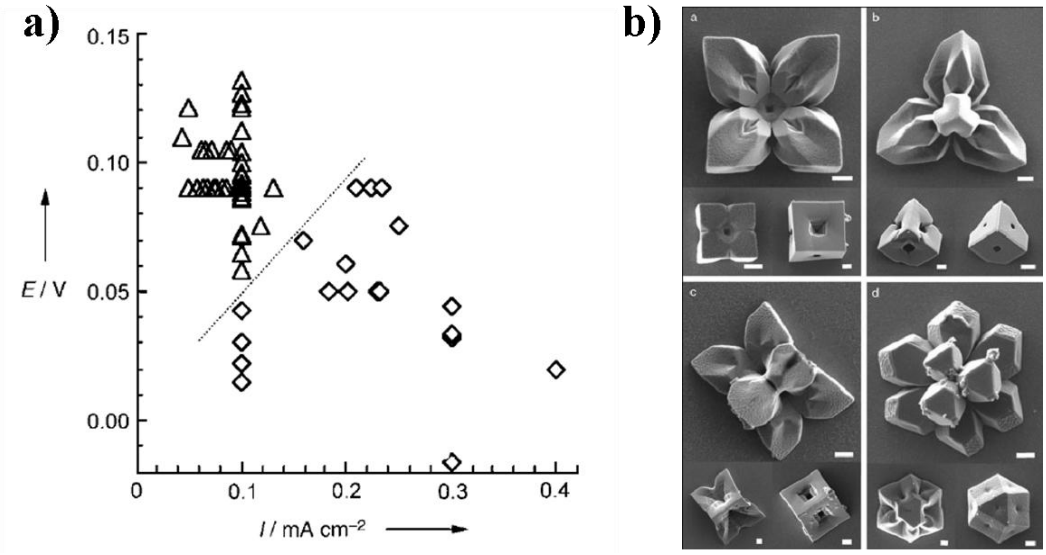

Figure 2.12 a) A deposition potential–current diagram summarizing the effect of electrochemical conditions on branching (triangle) and faceting (diamond) growth and b) SEM images of branched Cu_2O crystals with varying crystal habits [21].

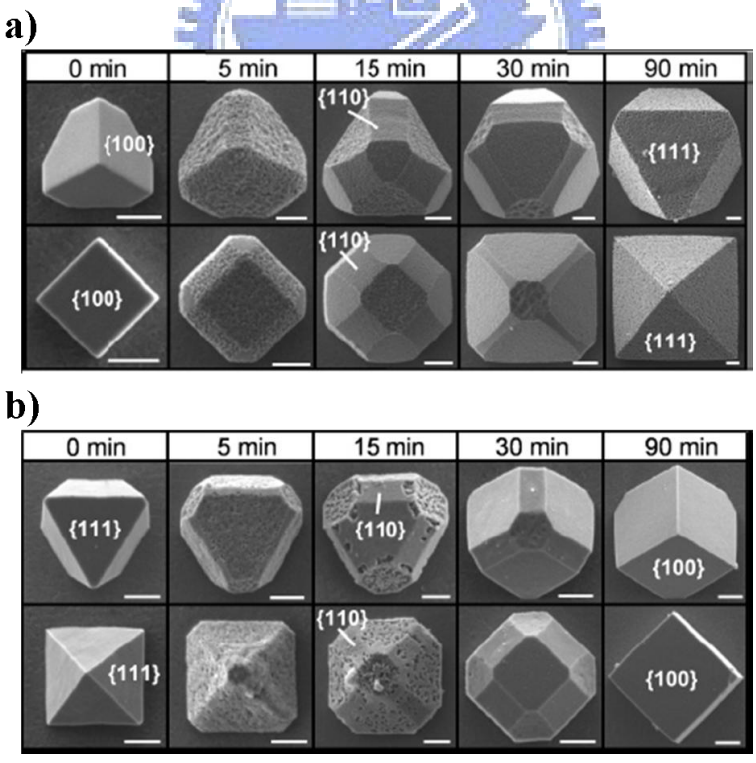

Figure 2.13 a) SEM images showing the transformation of pre-grown cubic Cu_2O crystals over time in a 0.02 M $Cu(NO_3)_2$ solution containing 0.17 M $(NH_4)_2SO_4$ and b) in a 0.02 M copper nitrate solution containing 0.17 M SDS and 0.004 M NaCl [22].

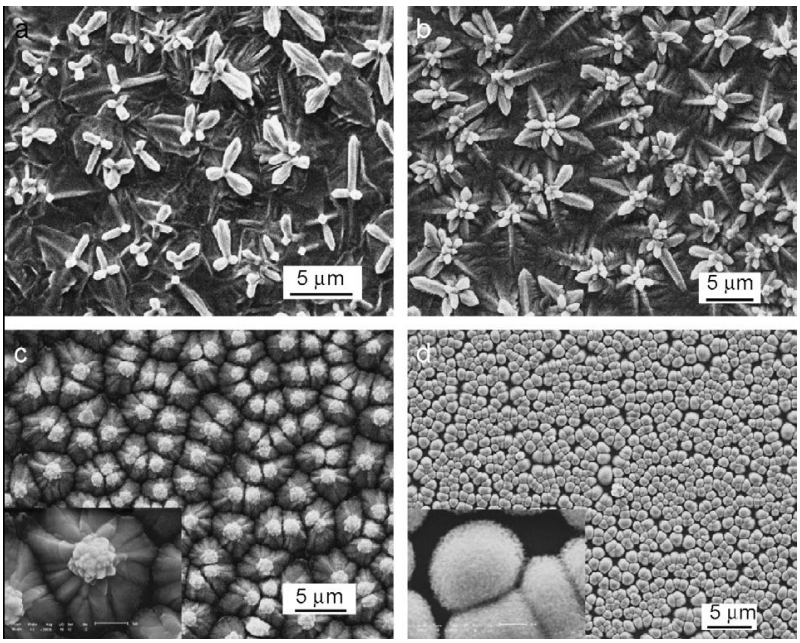

Figure 2.14 SEM images of Cu_2O micro-nanostructures deposited on ITO substrates from electrolyte containing 0.02 M $Cu(Ac)_2$, 0.1M NaAc and CTAB with different concentration; a) 0, b) 0.4, c) 0.8, and d) 2.8 mM [23].

2.2. Photoelectrochemistry

2.2.1. Fundamentals of Semiconductor Electrochemistry and Photoelectrochemistry [24-25]

Photoelectrolysis is a vast field that covers a variety of compound formation. Among them, the photoelectrolysis of water is one of the most attractive subjects. Because global consumption of energy is rapidly increasing over the years, finding the supply to meet this rising demand is a critical task in the future. Hydrogen offers a great potential for the environmental and energy supply infrastructure. Typically, it can be produced from hydrocarbons and water splitting. In order to drive this

thermodynamically uphill reaction with minimized fossil energy input, the solar energy is considered to be an ideal source.

There are several requirements for any system intended for converting and storing solar energy. First, sunlight must be efficiently absorbed to produce electrons in the excited states within the light-absorbing material. Second, to obtain desirable work either in chemical or electrical form, the photoexcited electrons and their associated vacancies must be separated in space to prevent their recombinations, which produces heat and wastes energy. Third, the photoexcited charges must be energetically and kinetically sufficient to perform a specific chemical reaction, for instance, splitting the water into H_2 and O_2. Furthermore, these charges must not produce unintended end-products. Lastly, the stability for a photocatalyst needs to be reasonably acceptable. Satisfying all of these requirements simultaneously is a tall order.

A photoelectrochemical cell is used to produce H_2 from water electrolysis under sunlight. The possibility of producing H_2 using UV light in a photoelectrochemical cell was first demonstrated by Fujishima and Honda in 1972 using a semiconductor material such as TiO_2 (Fig 2.15) [24]. Since then, a series of studies have been initiated for the photoelectrolysis of water. A popular approach is to use the semiconductor as the light absorber. Semiconducting solids generally have broad, strong optical absorption characteristics, and effective charge separation is facilitated by electric fields at the interface between the semiconductor and liquid electrolyte. Presented in Fig 2.16 are several semiconductor-based systems proposed for solar water splitting [26]. The simplest one is a semiconductor-electrolyte cell, which is also named the photoelectrochemical solar cell (PEC).

A semiconductor typically exhibits a band gap (E_g) in the 1-4 eV, which has an important bearing on its optical response. Fig 2.17 presents the band gap for several

semiconductors in contact with an aqueous electrolyte at pH 1. The band gap reflects the solar energy that a semiconductor could absorb and is the indicator for the driving force for subsequent reactions. The other important factor is the relative positions for the participating energy levels in the semiconductor and solution.

The study of semiconductor-electrolyte interfaces has both fundamental and practical motivations. The important point that distinguishes the semiconductor-electrolyte interface from the metal-electrolyte and metal-semiconductor interface is apparent. For a metal, the charge, and thus the associated potential drop, is concentrated at the surface penetrating at most a few Å into the interior. The metal can not support an electric field within itself. Thus, when a metal electrode contacts with an electrolyte, almost all the potential drop at the interface occurs within the Helmholtz region in the electrolyte phase. On the other hand, when a semiconductor is immersed in the same electrolyte, equilibration at the interface requires the flow of charge from one phase to the other and a "band bending" occurs within the semiconductor phase. The net result of equilibrium is that $E_F = E_{F,redox}$ and "built-in" voltage, V_{SC}, develop within the semiconductor phase, as illustrated in Fig 2.18. After equilibration, the Fermi levels are the same on either side of the interface.

The band bending phenomenon is by no means unique to the semiconductor -electrolyte interface. This layer is the space charge region or the depletion layer, which affects the direction of charge flow. We can see the distinct bending direction between a n-type or p-type semiconductor. Their photoelectrochemical currents flow is opposite to each other. The energy scheme for a cell with one n-type semiconductor electrode for photoelectrolysis of water is shown in Fig 2.19. It illustrates the flow of charge in a photoelectrolysis reaction.

The band gap of Cu_2O is about 2 eV. It has attracted substantial attention these years for its capability to splitting water. We summarize some studies on the

photoelectrochemical properties of Cu_2O in the next section.

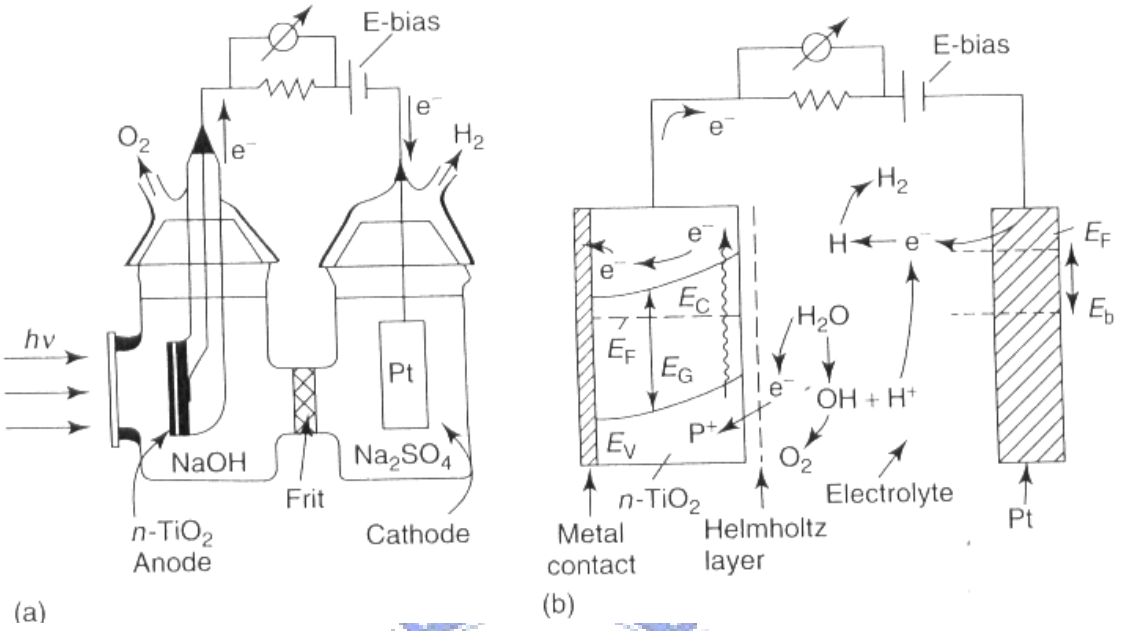

Figure 2.15 a) Fujichima-Honda cell with n-TiO_2 photoanode and Pt-cathode, as well as b) a schematic energy level diagram of the cell [24].

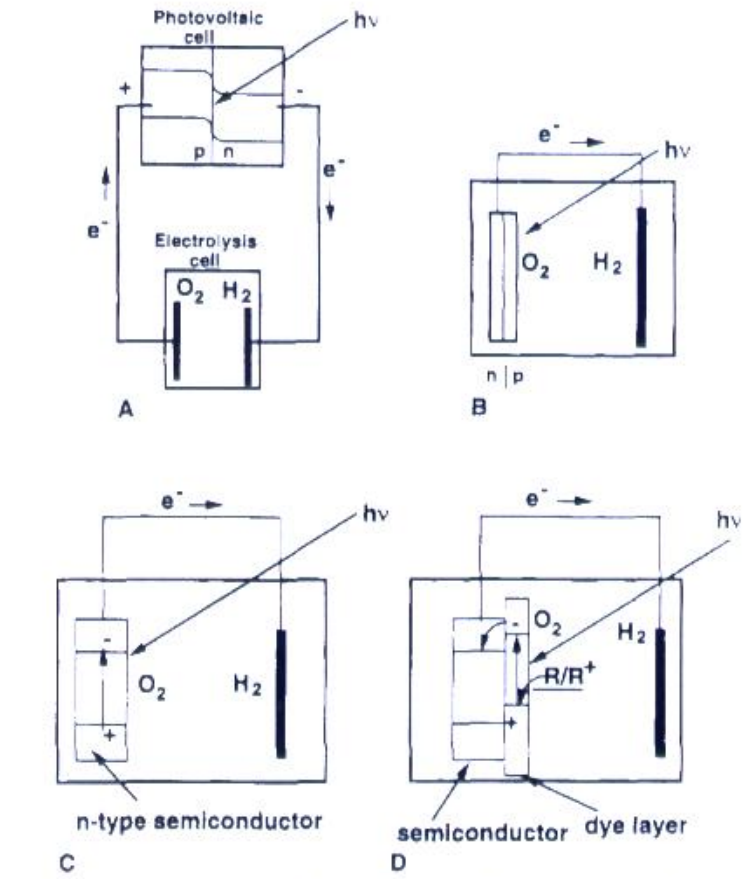

Figure 2.16 Schematic diagrams of different types of semiconductor-based systems proposed for solar water splitting; a) solid state photovoltaic cell driving a water electrolyzer, b) cell with immersed semiconductor p/n junction as one electrode, c) liquid junction semiconductor electrode cell, and d) cell with dye-sensitized semiconductor electrode [26].

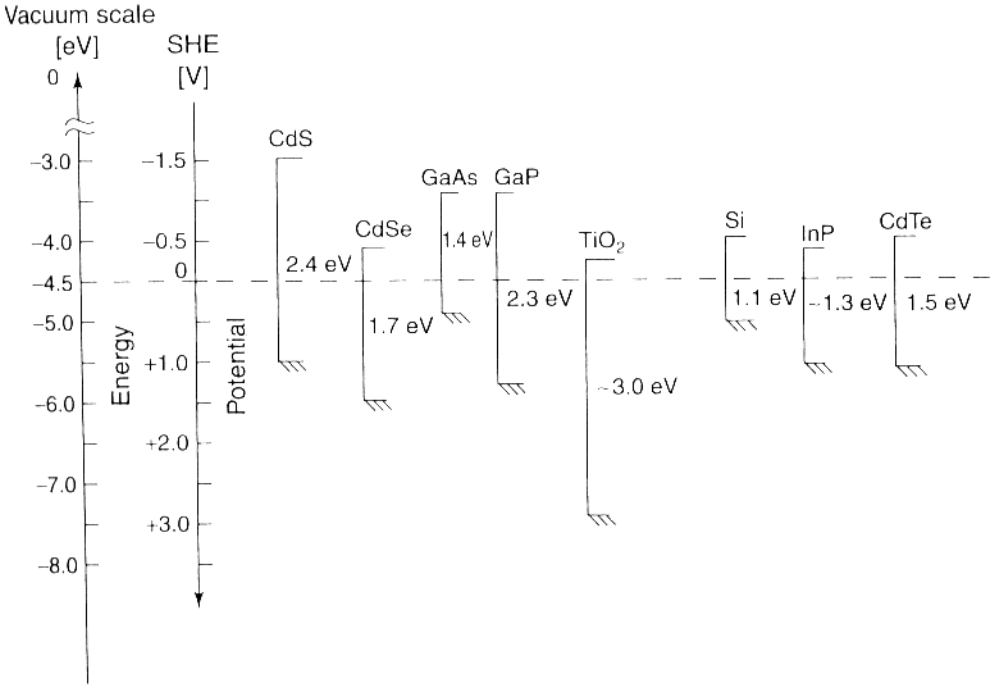

Figure 2.17 Relative dispositions of various semiconductor band edge positions shown both on the vacuum scale and with respect to the SHE reference. These band edge positions are for an aqueous medium of pH 1 [24].

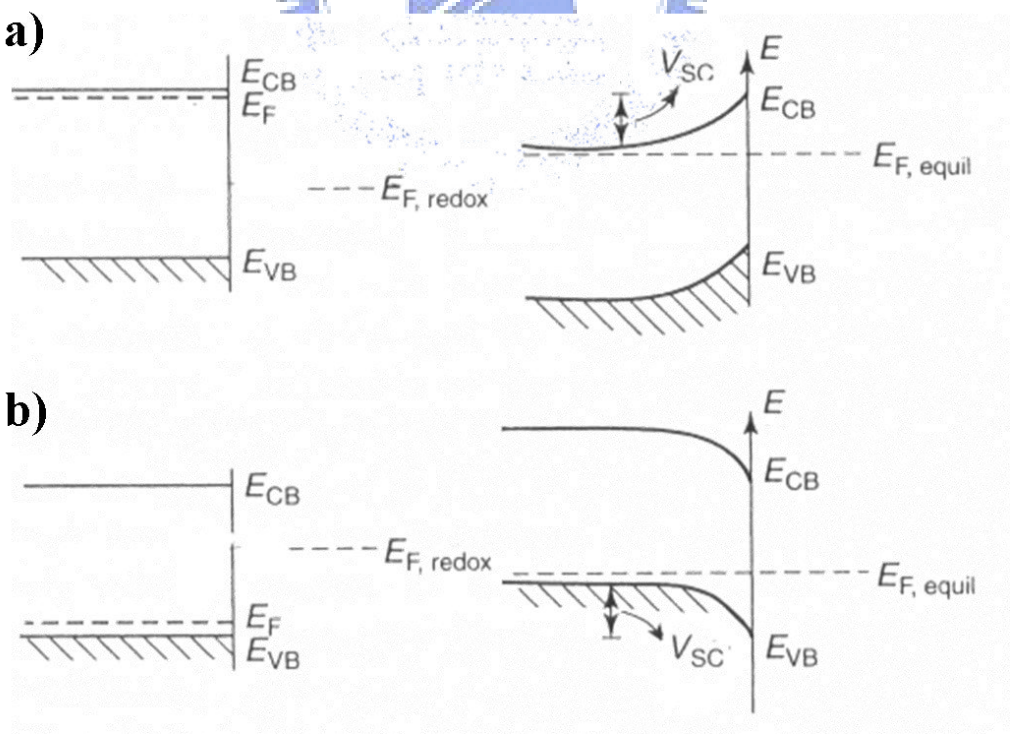

Figure 2.18 Energy level of a semiconductor-electrolyte interface before equilibrium (left-hand side) and after equilibrium (right-hand side); a) n-type and b) p-type

semiconductor [24].

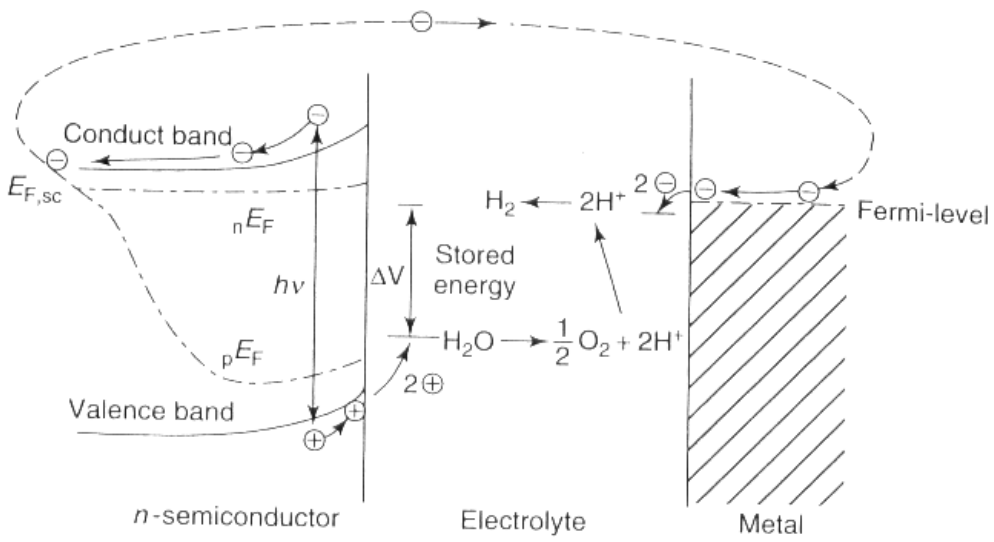

Figure 2.19 Energy scheme of a cell with one n-type semiconductor electrode for photoelectrolysis of water. ΔV is stored energy for electrolysis. $_pE_F$ is Fermi level of photogenerated holes known as quasi-Fermi level, $_nE_F$ is Fermi level of electron [24].

2.2.2. Photoelectronchemical Properties of Cuprous Oxide

A. Hydrogen Evolution of Cuprous Oxide

In 1998, Domen *et al.* were first to claim that the Cu_2O powder was capable of splitting water under visible light irradiation and its activity was recorded longer than 1900 h (Fig 2.20) [27]. However, the ability of Cu_2O was questioned next year by Joung *et al.* [28]. They used a polycrystalline Cu_2O electrode for photoelectrolysis of water but did not measure any cathodic photocurrent under illumination. Nevertheless, it seemed that the Cu_2O was able to reduce methylviologen efficiently (Fig 2.21). Their results implied that the reduction of water was highly unlikely to Cu_2O. Although, the Cu_2O is thermodynamically possible to reduce water but it is inefficient

to oxidize water. The conduction band edge of Cu_2O is +0.6 V and the oxidation potential of water is +0.57 V at pH 7. As a result, the Cu_2O could not supply adequate overpotential for water oxidation. Therefore, Joung *et al.* concluded that the Cu_2O could be a promising material, in conjunction with a suitable redox system as used a p-type photoelectrode in an electrochemical photovoltaic cell, but not for direct photoelectrochemical water splitting.

Rajeshwar *et al.* used different sacrificial electron donors to promote of Cu_2O for water oxidation [29]. They used a two-compartment (Fig 2.22), two-electrode electrochemical cell, to measure the photocurrent. The electrodeposited Cu_2O films with or without Ni modification were used as the working electrode. They explored different electrolytes in two compartments which were 0.5 M $NaSO_4$ with 40 mM methyl viologen in cathode compartment and 0.5 M $NaSO_4$ with different sacrificial electron donors in anode. Their results indicated that the hydroquinone at pH 10 delivered the highest performance as the sacrificial electron donor in their system. Ni modification exhibited a better performance, and the mass transfer of methyl viologen species was strongly affecting the resulting reaction. These electron mediators were effective in capturing the photogenerated electrons from the Cu_2O before they underwent recombination. Their results implied that after adding suitable electron mediators, the Cu_2O could be used as a catalyst for water splitting.

In the next year, Teng *et al.* also focused on improving the efficiency of Cu_2O to oxidize water by coupling the Cu_2O with a n-type semiconductor such as WO_3 [30]. The valence band edge of WO_3 was +2.54 V (vs. Ag/AgCl at pH 7) which was much more positive than the water oxidation potential. Their results showed the Cu_2O film exhibiting a (111) preferred orientation revealing a better activity. And coupling a n-type counter electrode also enhanced the photocurrent. The accumulated H_2 evolution was with reasonable agreement to the measured photocurrent (Fig 2.23).

However, the stability of Cu_2O was still being questioned. Kakuta *et al.* synthesized the Cu_2O powders as a photocatalyst for water splitting [31]. The powder was suspended in the electrolyte during illumination. The results showed that the stoichiometric splitting of water into H_2 and O_2 did not take place by Cu_2O particularly in water. In their study, only the evolution of H_2 was confirmed (Fig 2.24). However, they examined the Cu_2O after reaction and identified the presence of CuO. The proposed mechanism was:

$$Cu_2O + 2OH^- + 2h^+ \rightarrow 2CuO + H_2O \quad (6)$$

They concluded that the Cu_2O was unable to perform photocatalytic splitting of water, because the Cu_2O became inactive and self-oxidized during H_2 evolution.

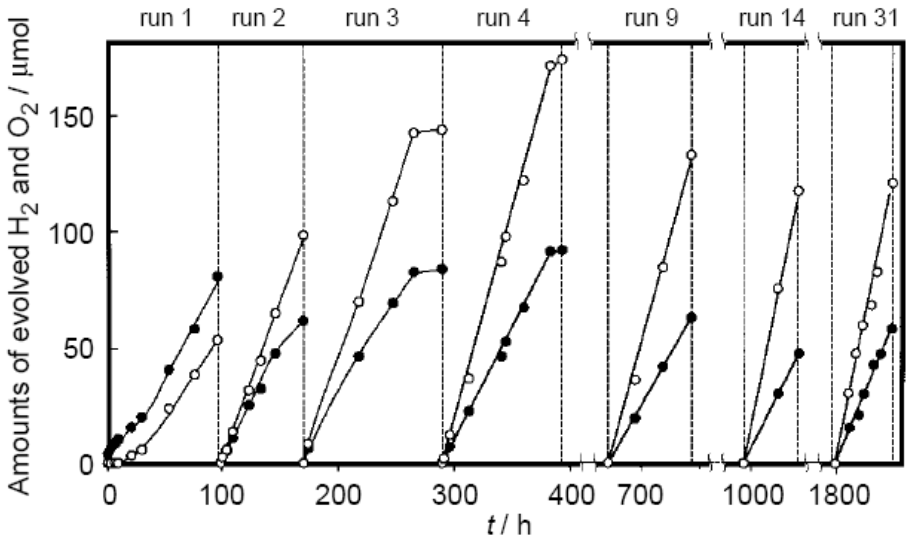

Figure 2.20 Time courses of H_2 (open circles) and O_2 (filled circles) evolution in Cu_2O under visible light ($\lambda \geqq 460$ nm) irradiation. Catalyst: 0.5 g, H_2O: 200 cm^3. The reaction system was evacuated with light irradiation after each run [27].

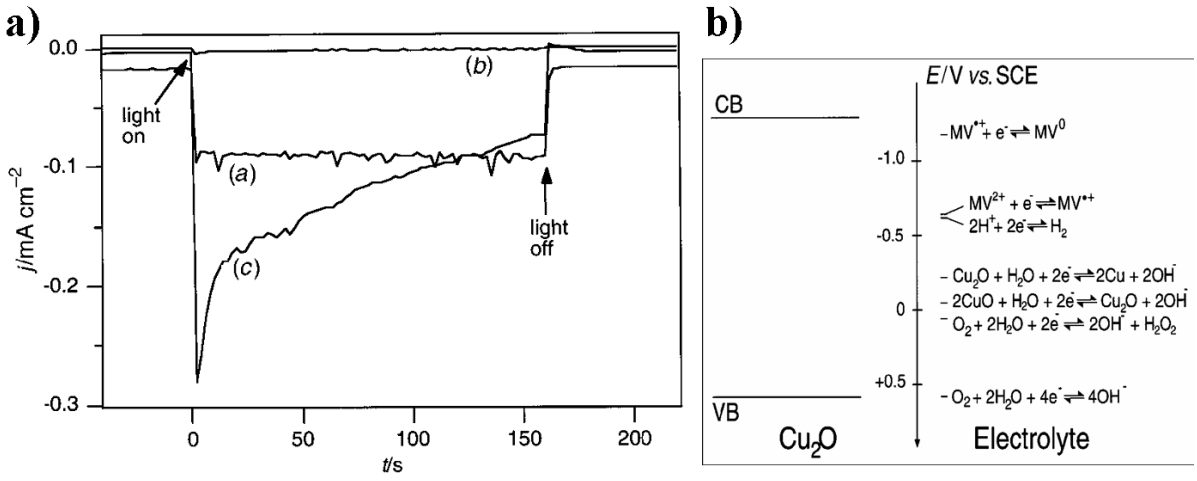

Figure 2.21 a) Current density at -0.4 V measured on a 0.5 mm thick Cu_2O electrode illuminated with 350 nm in 0.5 M Na_2SO_4 solution; (a) bubbled with air, (b) bubbled with Ar, and (c) bubbled with Ar and with 40 mM MV^{2+} added to the solution. b) The overview of the redox potentials of the relevant reactions with respect to the estimated position of the Cu_2O band edges [28].

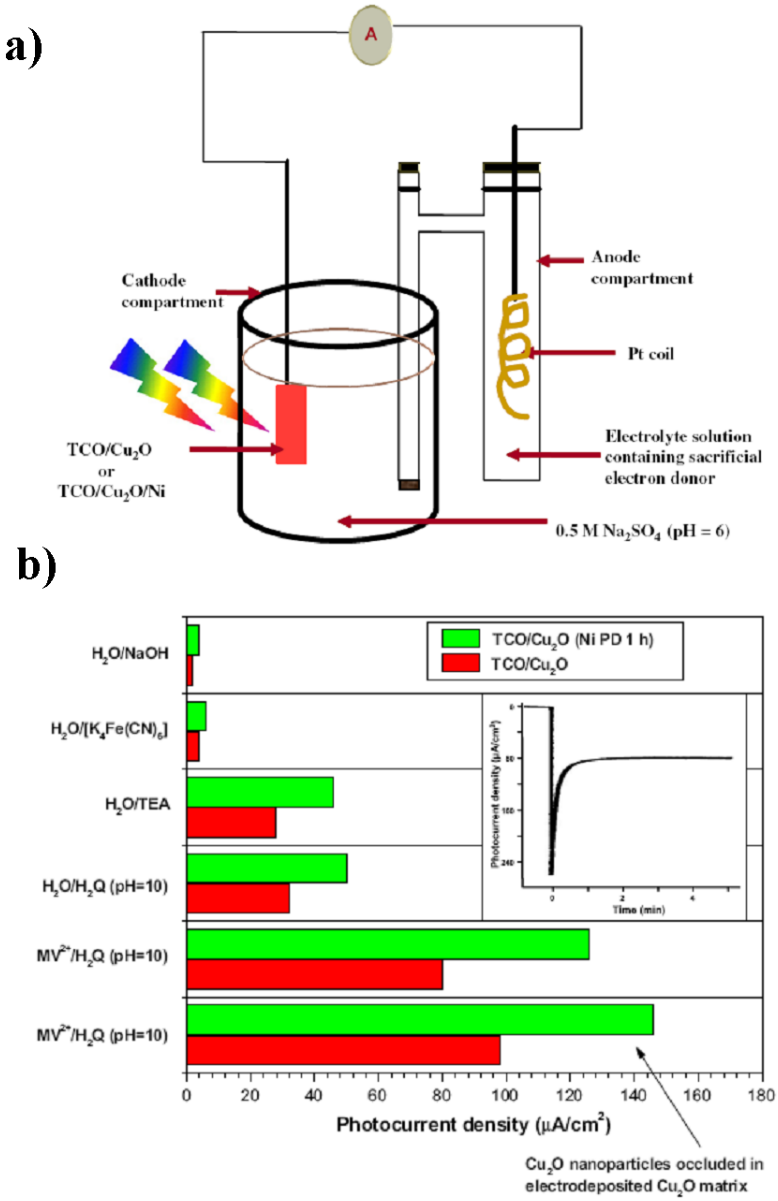

Figure 2.22 a) The set-up used for combining the photocatalytic generation of hydrogen at p-Cu_2O with the "dark" oxidation of a sacrificial electron donor (reducing agent) in the cathode chamber. b) The zero bias spontaneous photocurrents measured by connecting the p-Cu_2O photoelectrode with the Pt coil in the anode chamber. The insert shows a representative set of chronoamperometric data obtained for MV^{2+}/HQ (pH 10) [29].

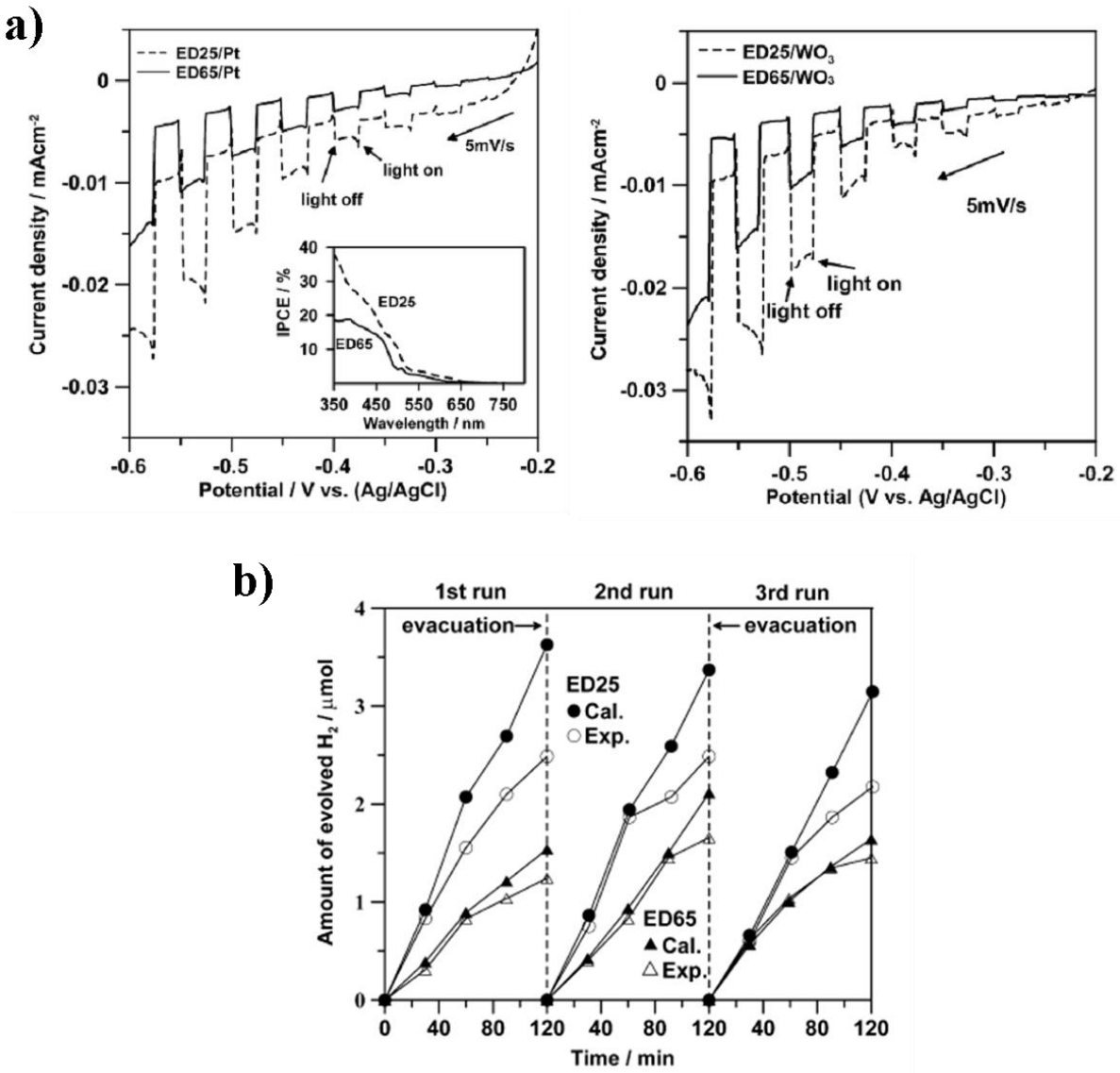

Figure 2.23 Current–potential characteristics for Cu_2O films obtained with a potentiodynamic scan of 5 mV/s and chopped visible light irradiation (50 mW/cm^2). a) Pt sheet and b) WO_3 film was used as the counter electrode and the electrolyte solution was 0.5 M Na_2SO_4 bubbled with Ar. c) Time course of H_2 evolution from the Cu_2O films biased at -0.3 V under continued visible-light irradiation. A Pt sheet was used as the counter electrode. The amounts of H_2 evolution were determined from the experimental measurement with gas chromatography (open symbols) and from the calculation based on the photocurrent (filled symbols) [30].

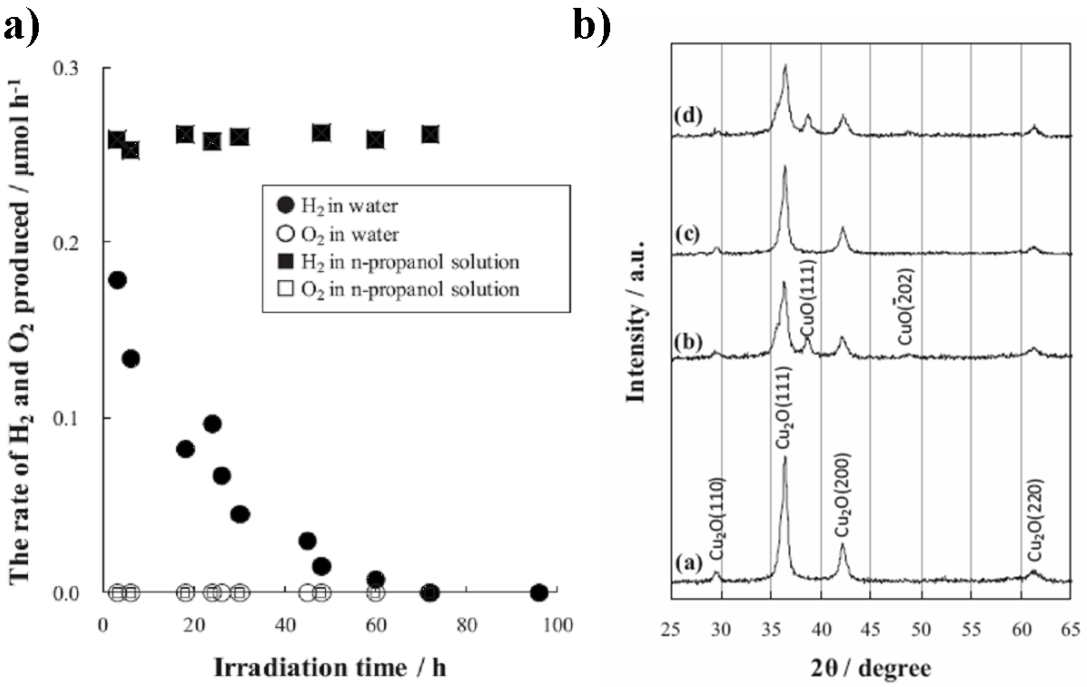

Figure 2.24 a) Time-course of the evolution rates of both H_2 and O_2 at Cu_2O in the presence and absence of 2.5 mol·dm^{-3} *n*-propanol. b) XRD patterns of Cu_2O powder (a) before irradiation, (b) after the evolution of H_2 under irradiation in water [31].

B. N-type Cuprous Oxide

There were also many studies on n-type Cu_2O, but most of them demonstrated rather poor performances. Substitutional n-type doping in the Cu_2O lattice can occur at either Cu or O sites. Based on the valence of Cu (+1) and O (-2) in Cu_2O, possible n-type dopants are group VII elements for the O sites and group II elements for the Cu sites. Tao *et al.* experimented with doping of Cu_2O by Cl using electrodeposition in 2009 [32]. In their process, they added various concentrations of $CuCl_2$ to the electrolyte. The resistivity for the Cu_2O film was reduced from 157 to 48 Ω by adjusting the Cl concentration (Fig 2.25). The resistivity was further reduced from 103 to 7 Ω by increasing the deposition temperature. After several tries, they

successfully prepared a low-resistivity n-type Cu_2O film.

It is known that the grain size strongly affects the photoelectrochemical performance of a semiconductor. As the size is increasing, the electron-hole recombination at the boundary area is largely reduced. Choi *et al.* were familiar with controlling the crystal growth of Cu_2O [33]. They grew n-type Cu_2O films and increased the crystal size by adjusting the overpotential, concentration of copper ion, and concentration of the deposition solution. An unique dendritic crystal was growing larger but without losing its surface area. Related scheme for the crystal growth is shown in Fig 2.26. The highest photocurrent came from dendritic crystals that laterally expanded ca. 1200 μm^2 while the thickness of the electrode was maintained below 5 μm. The photocurrent was enhanced 20 times larger than that of cubic crystals. Their morphologies and related photoresponses are presented in Fig 2.27.

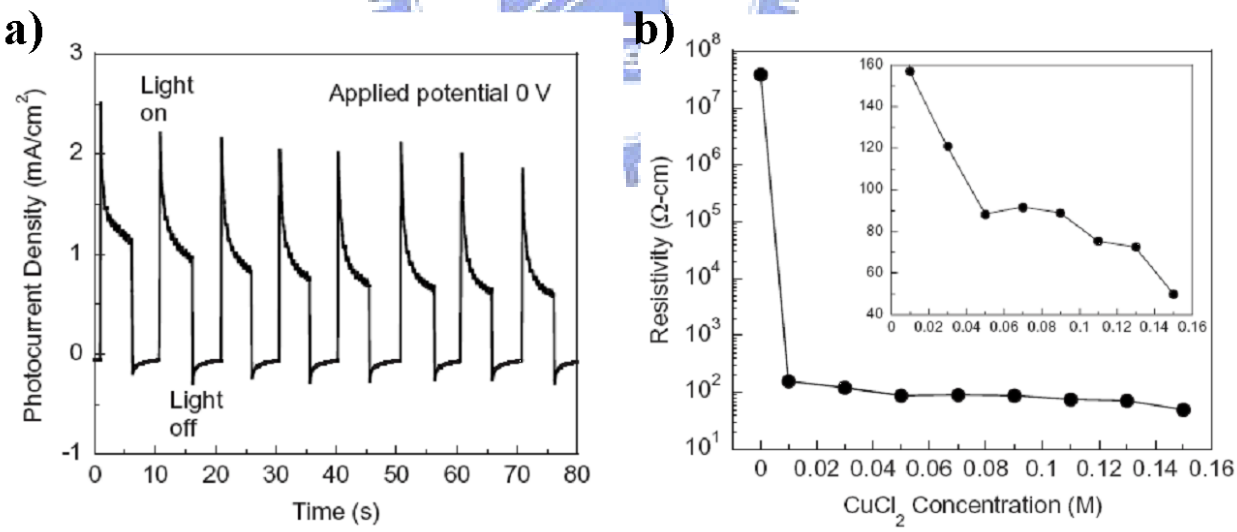

Figure 2.25 a) Photocurrent measured from Cl-doped Cu_2O under zero bias (vs. Ag/AgCl) in 0.5 M Na_2SO_4. The light source was 90 W white-light. b) The resistivity of undoped and Cl-doped Cu_2O as a function of $CuCl_2$ concentration in the solution [32].

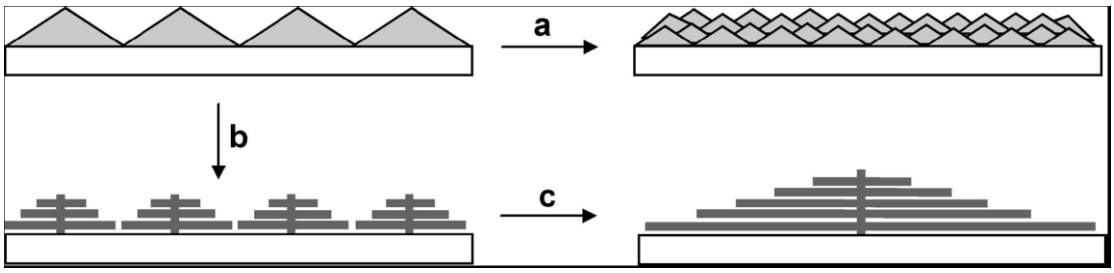

Figure 2.26 A scheme of crystal growth; a) increasing nucleation density while reducing crystal sizes, b) inducing dendritic branching growth without increasing nucleation density, and c) electrode composed of one dendritic crystal covering the entire substrate [33].

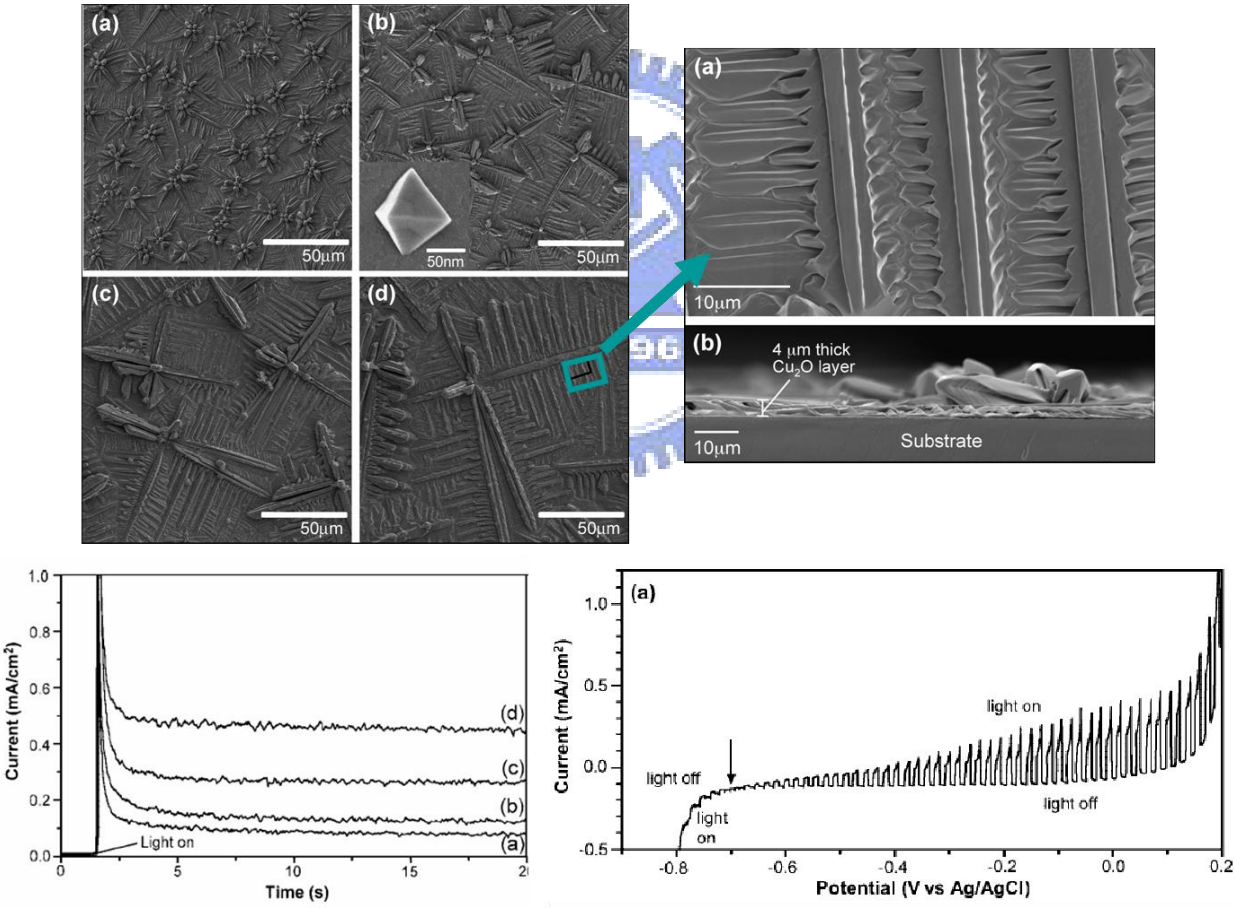

Figure 2.27 SEM images of Cu_2O electrode deposited in various concentrations of buffer. The close view on the right-hand side is the front-view and side-view of the Cu_2O with the longest dendrite which also delivers the best performance [33].

Chapter 3

Structure and Annealing Studies of Electrodeposited Cu_2O Films

3.1. Introduction

In this section, we electrodeposited two different Cu_2O films and studied the effect of thermal annealing. The annealing effect on the electrodeposited Cu_2O had only been studied on the films deposited in the pH 9 bath before. Here, we explored the films electrodeposited in pH 9 and pH 11 baths in order to fully characterize the annealing effect on two different oriented films. We also examined the photoelectrochemicalproperties for these two films and then results are discussed in chapter 4.

3.2. Experimental

3.2.1. Reagents

1.	Cu_2SO_4	SHOWA, 97.5 wt%
2.	Lactic acid	TEDIA, 85～90 wt%
3.	NaOH	SHOWA, 96 wt%

3.2.2. Setup

A. Electrodeposition

We used a power supply (MOTECH, LPS-305) for potentiostatic electro-deposition of Cu_2O films. The substrates employed were 1×3 cm^2 stainless steel (316L), which were first polished, and then cleaned by de-ionized water under supersonic vibration for 5 min twice, and then cleaned by ethanol and acetone. The electrolytes consisted of 0.4 M $CuSO_4$ and 3 M lactic acid.

The deposition temperature was 60 ℃ and the deposited potentials were -0.2, -0.3, and -0.4 V, respectively. The deposition times were 30, 60, and 100 min. Electro-plating baths were pH 9 and 11 and their pH values were adjusted by adding additional NaOH.

B. Annealing

The Cu_2O films under annealing studies were deposited in pH 9 and pH 11 baths for 100 and 60 min, respectively.

The Cu_2O films were placed in a furnace which was pre-cleaned by purging Ar gas before the annealing process. The temperatures for the annealing were maintained at 150, 200, 250, 300, and 350 ℃, respectively with a heating rate at 1 ℃/min. The duration for the annealing times was maintained for 10, 30, and 60 min, respectively.

3.2.3. Materials Characterizations

A. X-ray Diffractometer (XRD)

X-ray diffraction (XRD) (HRXRD: Bedi D1) was used to determine crystal structure and composition of the Cu_2O films..

B. Scanning Electron Microscopy

A Scanning Electron Microscopy (Hitachi JSM 6700. or JSM 6500F) was used to observe the surface and thickness of the Cu_2O films.

C. Four-Point Probe

A four-point probe (CMT-SR2000N) was used to measure the resistivity of Cu_2O films.

3.3. Results and Discussion

3.3.1. As-deposited Cuprous Oxide Films

A. Effect of Plating Bath pH

We electrodeposited Cu_2O film in two different pH environments, pH 9 and pH 11, in order to obtain crystals in two different preferred orientations. The XRD was used to identify information on phases and compositions (Fig 3.1). The XRD results confirmed that we successfully electrodeposited pure Cu_2O films from both pH 9 and

pH 11 baths and they revealed distinct orientations. According to the JCPDS data base, the orientation for the Cu_2O films electrodeposited in pH 9 and pH 11 baths were (200) and (111), respectively. Notably, both of them displayed good crystallinity.

From top-view SEM images presented in Fig 3.2, they demonstrated distinctly different morphologies of these two films. The morphology of the pH 9 film was four-sided pyramid and its grain size was below 1 μm. In contrast, the pH 11 film had a much flatter morphology but in a larger grain size. Its size distribution was from 1 to 8 μm.

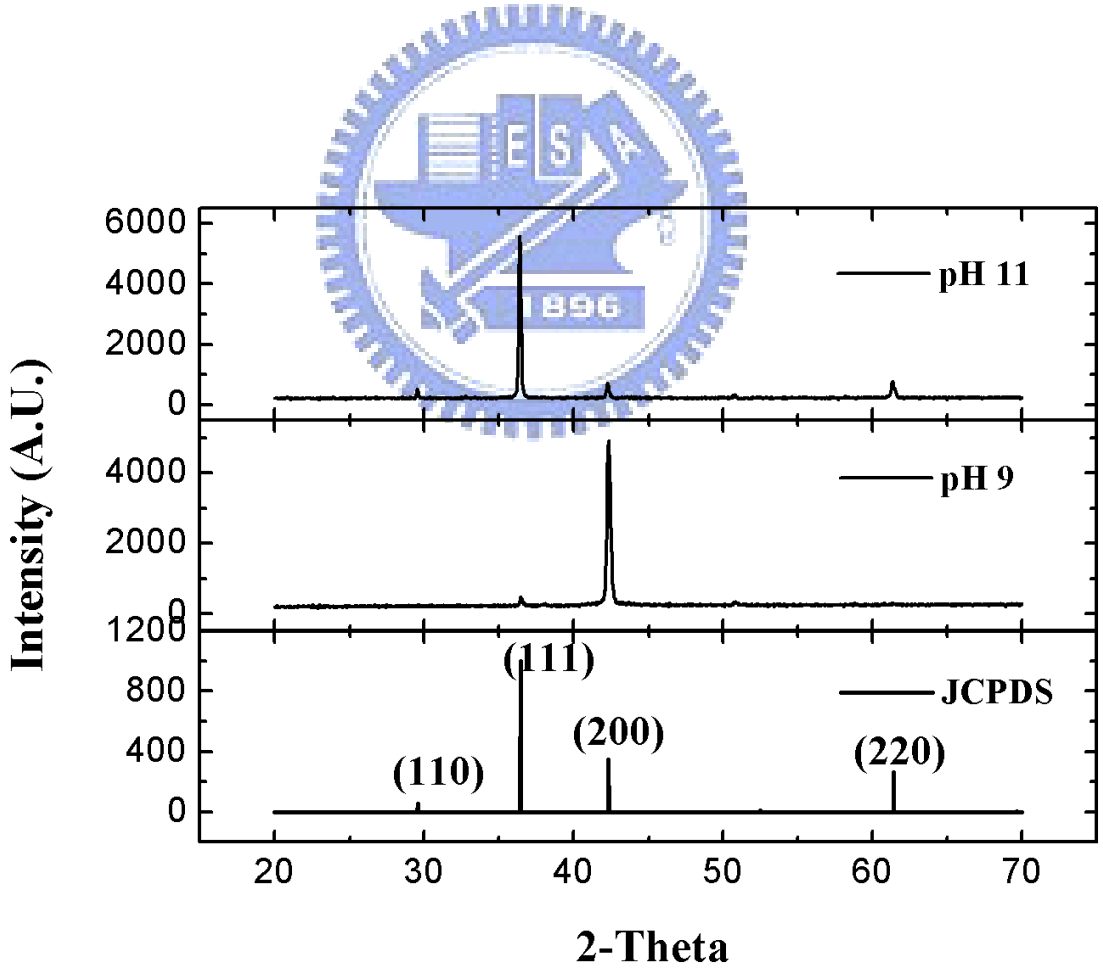

Figure 3.1 XRD patterns of Cu_2O film electrodeposited from baths of pH 9 and 11.

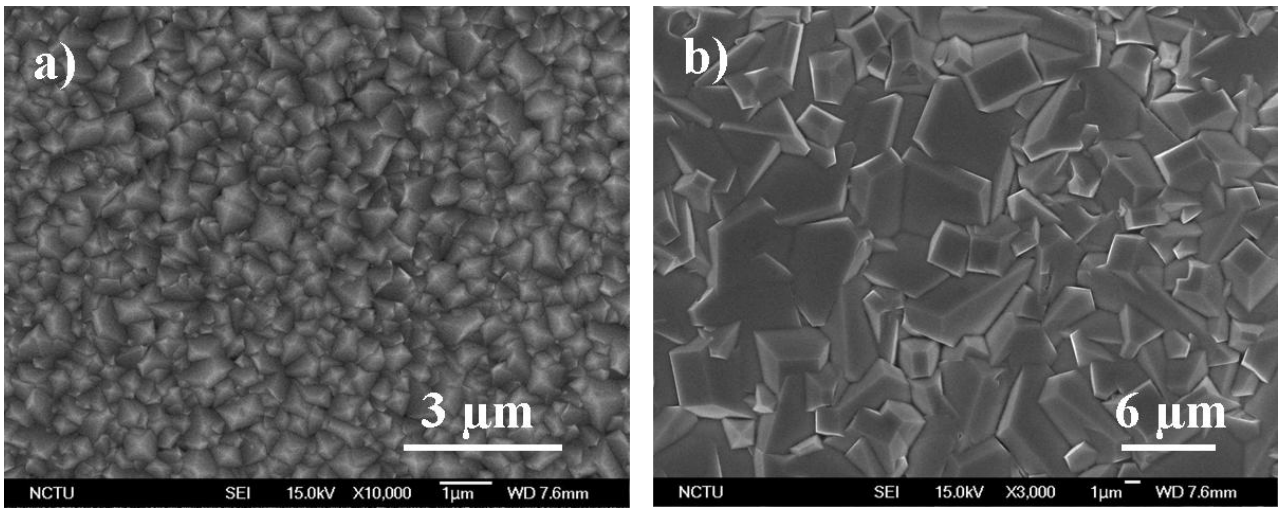

Figure 3.2 SEM images of Cu_2O films electrodeposited from baths of a) pH 9 and b) pH 11 bath.

B. Effect of the Electrodeposition Time

We adjusted different electrodeposition times of Cu_2O film to identify the relevant growth rate under these two pH conditions. The deposition times were 30, 60, and 100 min, respectively. The XRD pattern confirmed the composition for the films were pure Cu_2O in specific orientation (Fig. 3.3). We studied the top-view and side-view of these films and their images are presented in Fig 3.4 and 3.5, respectively.

From the top-view, the pH 9 films electrodeposited for 30 and 60 min demonstrated less uniformity than the film deposited for 100 min (Fig 3.4). As the deposition time was extended, the film became more uniform and thicker. The thickness for the films electrodeposited at pH 9 were 1.66, 1.87, and 2.28 µm for deposition time of 30, 60, and 100 min, respectively. On the other hand, the pH 11 film that was deposited for 30 min appeared irregular from the surface. However,

when the deposition time extended to 60 and 100 min, their top-views looked similarly (Fig 3.5). The thickness of pH 11 films were 5.63, 7.97, and 10.1 μm, respectively.

Our results indicated that the Cu_2O films electrodeposited at higher pH environments revealed a larger growth rate. The growth rate for the Cu_2O films deposited in pH 9 bath was slowing down as the deposition time became longer. Their thickness reached a plateau approximately at 2 μm. Compared with the films deposited in pH 11, they showed a higher growth rate and their thickness was proportional to the deposited time. However, the film deposited for 100 min in pH 11 bath appeared too thick to show desirable crystallinity

The difference for the growth rate was due to the pH value of the plating bath. According to Eq. (3) and Eq. (5) in Chapter 2, electrodeposition of Cu_2O is a pH-dependent process. We understood that the hydrogen formation is unfavorable to the deposition. Although we used two alkaline environments, the local pH at the working electrode was expected to decrease as the Cu_2O was deposited. A reduction in pH increased the solubility of Cu^+ ions and therefore the reversibility of Cu_2O crystallization. Our results implied that the Cu_2O deposited in pH 9 bath was strongly affected by the local pH variation as opposed to that of pH 11.

a)

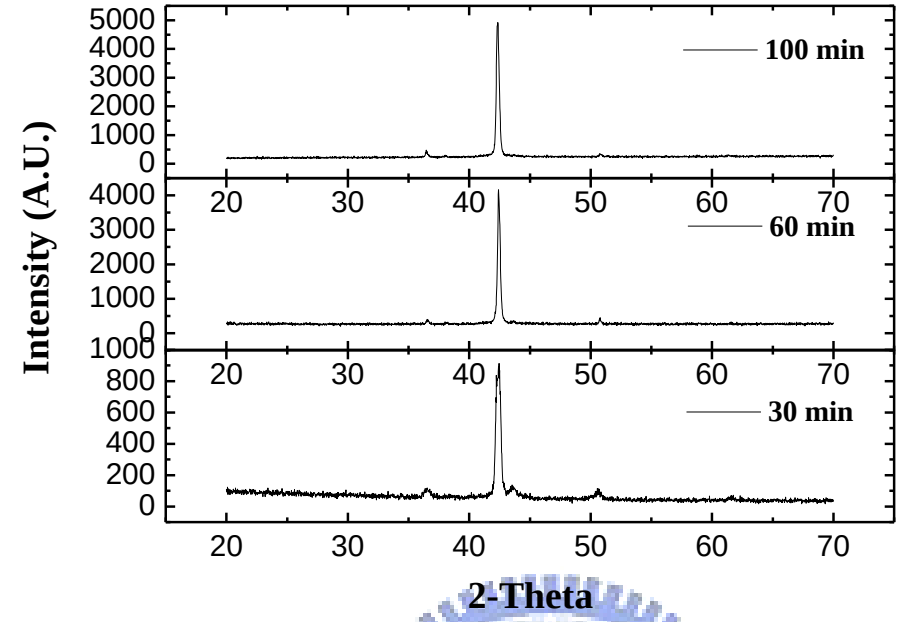

b)

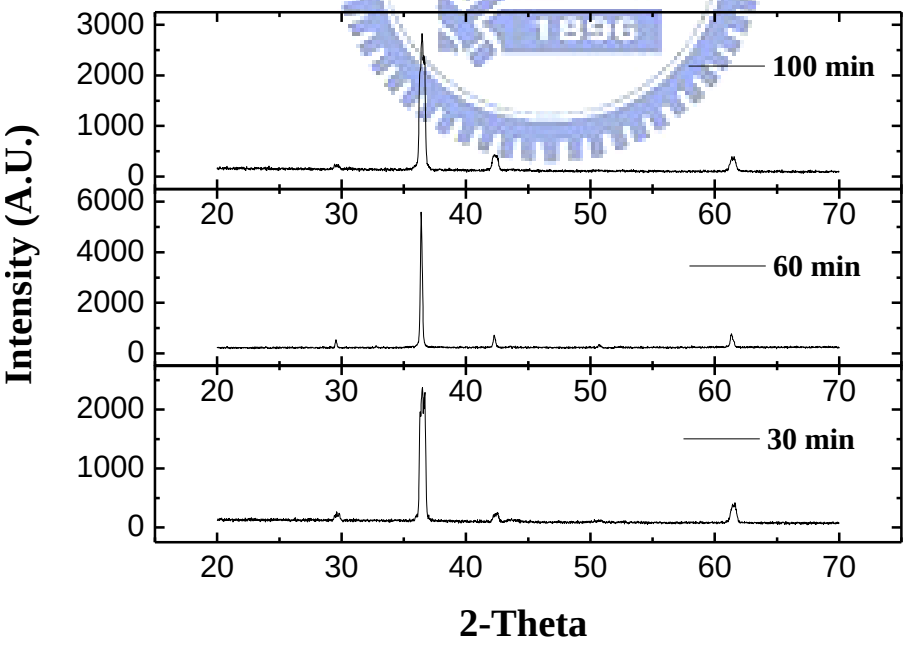

Figure 3.3 XRD patterns of Cu_2O films electrodeposited in a) pH 9 and b) pH 11 bath with different deposited time of 30, 60, and 100 min.

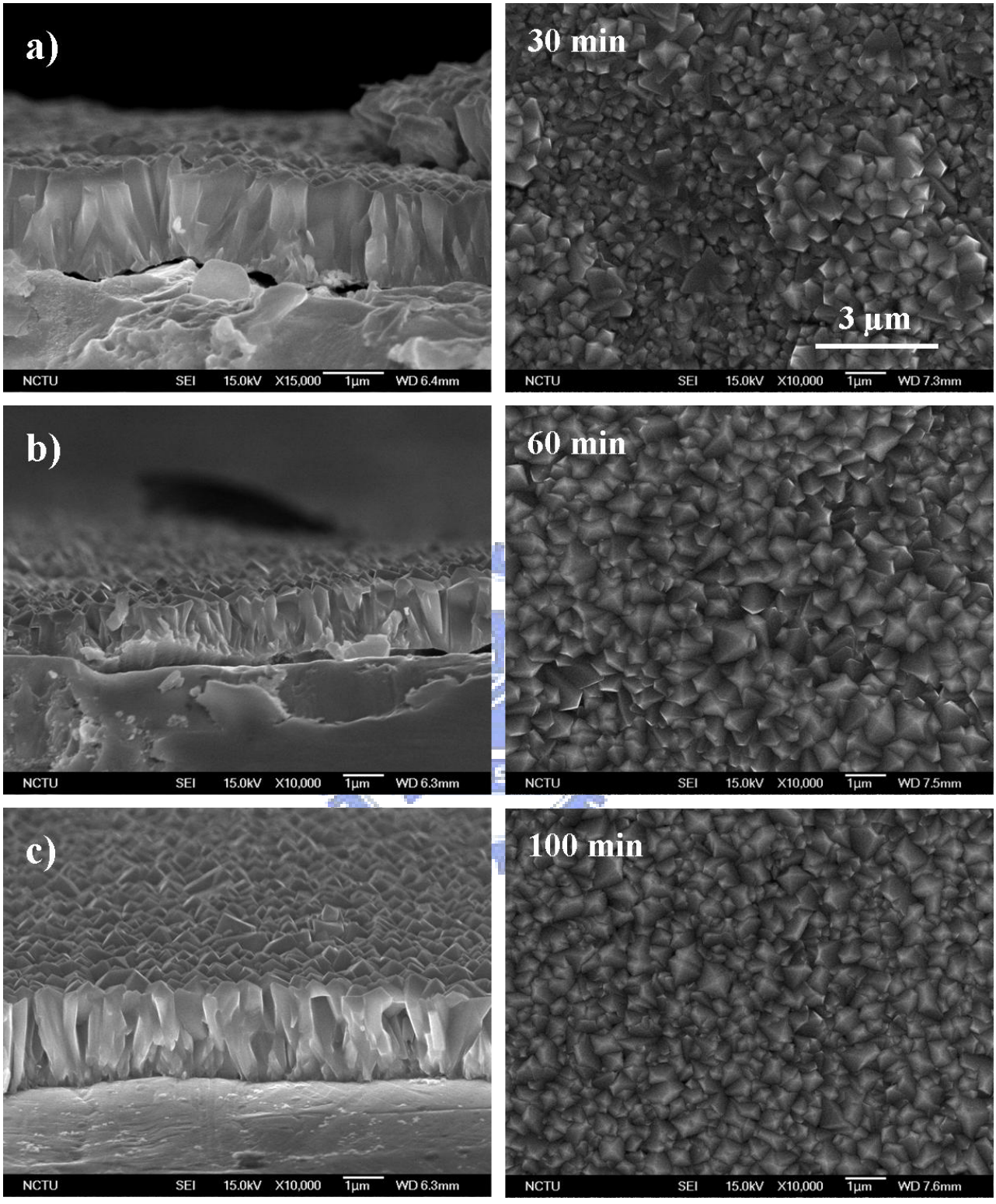

Figure 3.4 Top-view and side-view of SEM images of Cu_2O films electrodeposited under -0.3 V in pH 9 bath with deposition time of a) 30, b) 60, and c) 100 min, respectively.

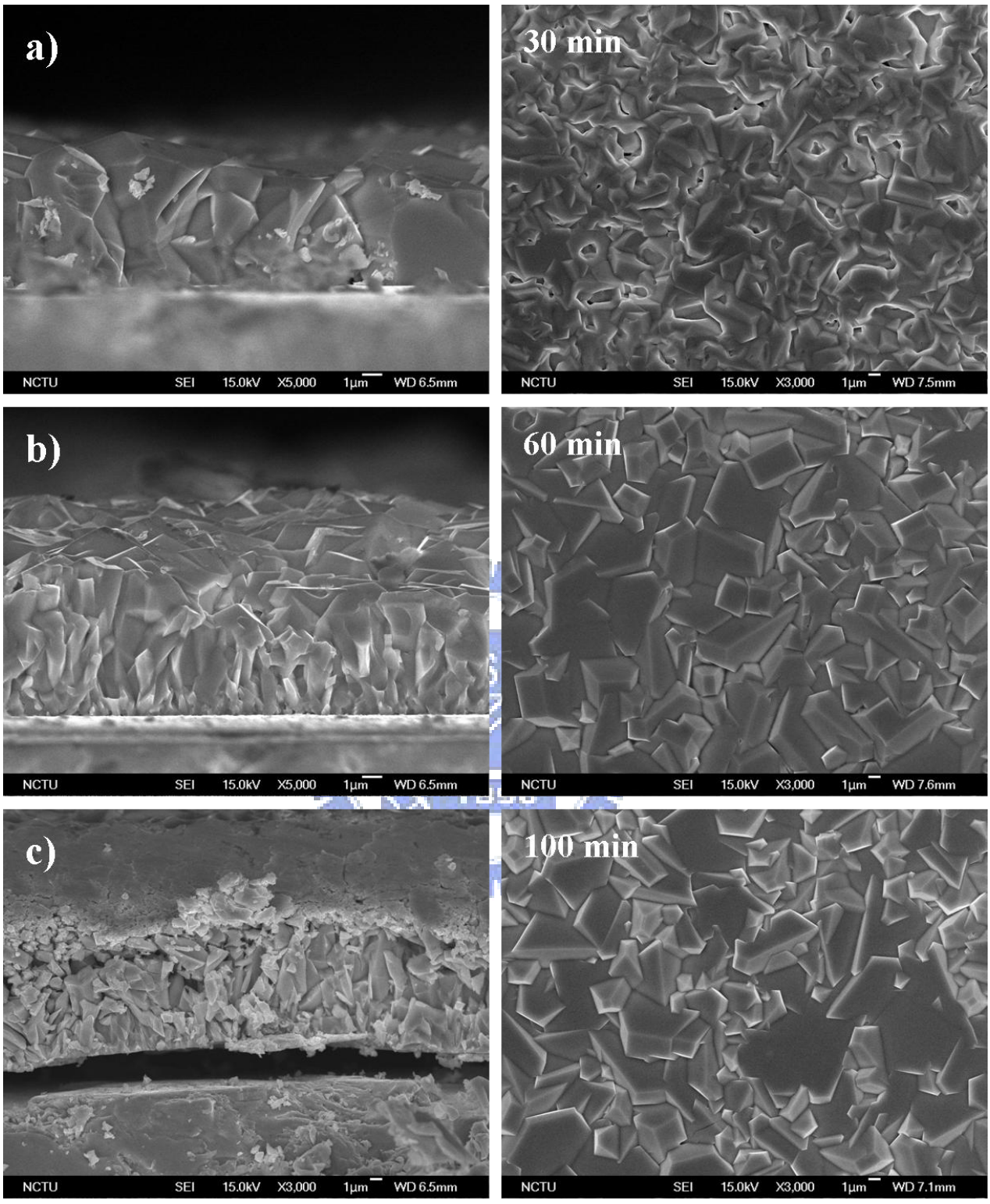

Figure 3.5 Top-view and side-view of SEM images of Cu_2O films electrodeposited under -0.3 V in pH 11 bath with deposition time of a) 30, b) 60, and c) 100 min, respectively.

C. *Effect of the electrodeposition voltage*

We electrodeposited the Cu_2O films in biases of -0.2, -0.3, and -0.4 V (vs. Ag/AgCl), respectively. It is known that the deposition overpotential (η) plays an important role in electrodeposition The η is defined as the difference between the applied deposition potential (E_{appl}) and the reduction potential of Cu^{2+} to Cu^{+} (E_{red}).

$$\eta = \left| E_{appl} - E_{red} \right| \quad (1)$$

$$E_{red} = E^0 - 0.05916 \log([Cu^+]/[Cu^{2+}]) \text{ at T = 298.15 K} \quad (2)$$

The η affects the nucleation density, growth rate, and the composition of electrodeposited Cu_2O films. Moreover, the Cu_2O is a metastable state as of Cu oxidation. According to Eq. 3-5 in Chapter 2, the Cu_2O film could only be electrodeposited at a narrow range of overpotential. When the overpotential was too large, the Cu^{2+} is reduced to Cu^0 directly or the Cu^+ is reduced to Cu^0. Consequently, accurate controlling of the driving force is critical during electrodeposition of Cu_2O.

The XRD spectra presented in Fig 3.6 confirmed the composition of Cu_2O films deposited under different overpotentials. We obtained pure Cu_2O films from pH 11 bath under -0.2, -0.3, and -0.4 V for 60 min. However, we observed the Cu (111) phase formed in the film that was deposited under -0.4 V in pH 9 bath. Our result confirmed that both Cu and Cu_2O were present from pH 9 bath under high overpotential. The Cu and Cu_2O were likely to be deposited simultaneously or the Cu_2O was deposited first then be reduced to Cu. Both electrodeposition routes were equally possible. When the deposition rate was increased, the pH 9 bath was easier to form Cu than pH 11 bath. This is because the concentration of OH^- was different in

the environment. The deposition of Cu_2O consumed the OH^- locally which caused the depletion of OH^- at working electrode. As a result, lack of O_2 caused formation of Cu instead of Cu_2O.

From the top-view in SEM images (Fig 3.7and 3.8), the films of pH 9 deposited under -0.2 V revealed slightly larger grains than the other one. The film that was deposited under -0.4 V appeared rough and irregular due to its high growth rate. All the pH 11 films looked similarly under different overpotential from the morphology.

The thicknesses of Cu_2O deposited in pH 9 under -0.2, -0.3, and -0.4 V for 60 min were 1.64, 1.97, and 2.26 μm, respectively. Their growth rate was slower in pH 9 bath and had less difference in resulting thickness. The thicknesses of Cu_2O deposited in pH 11 were 6.52, 7.97, and 12.02 μm, respectively. This suggested that pH 11 bath had a faster growth rate.

The films that were deposited for deposited 100 min in pH 9 bath as well as 60 min in pH 11 bath were used as following annealing experiments. They were chosen for their relatively improved crystallinity and reasonable thickness.

a)

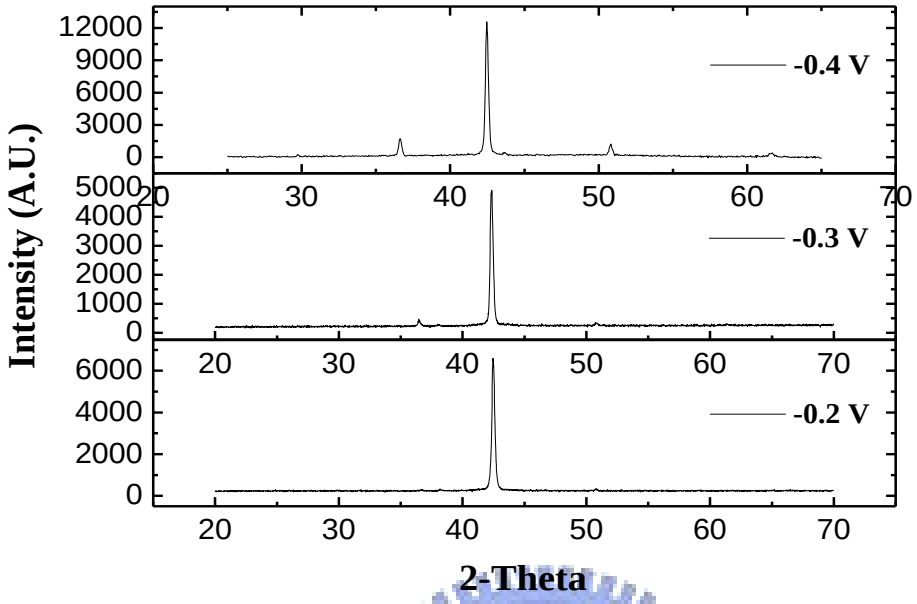

b)

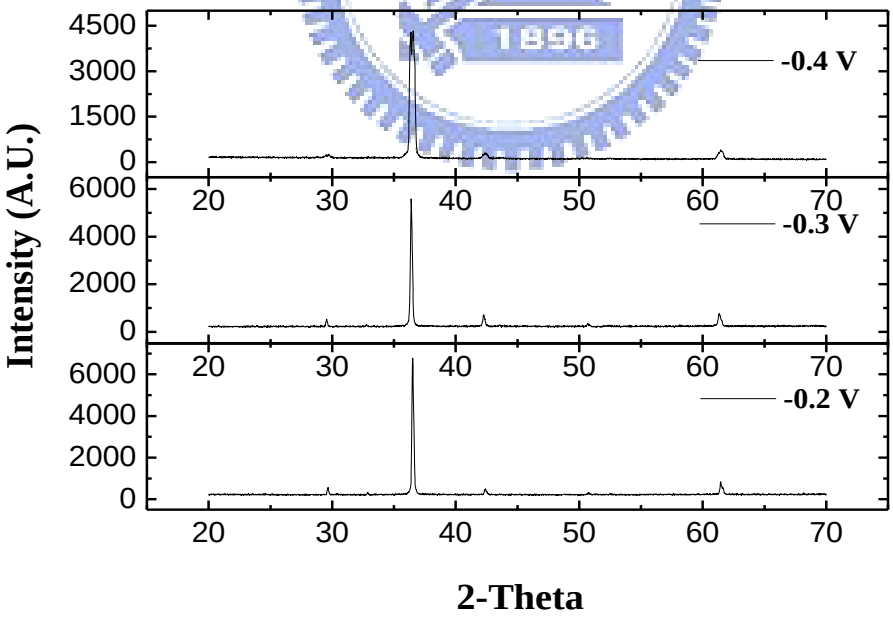

Figure 3.6 XRD patterns of Cu_2O films electrodeposited in a) pH 9 and b) pH 11 bath under -0.2, -0.3, and -0.4 V for 1 h.

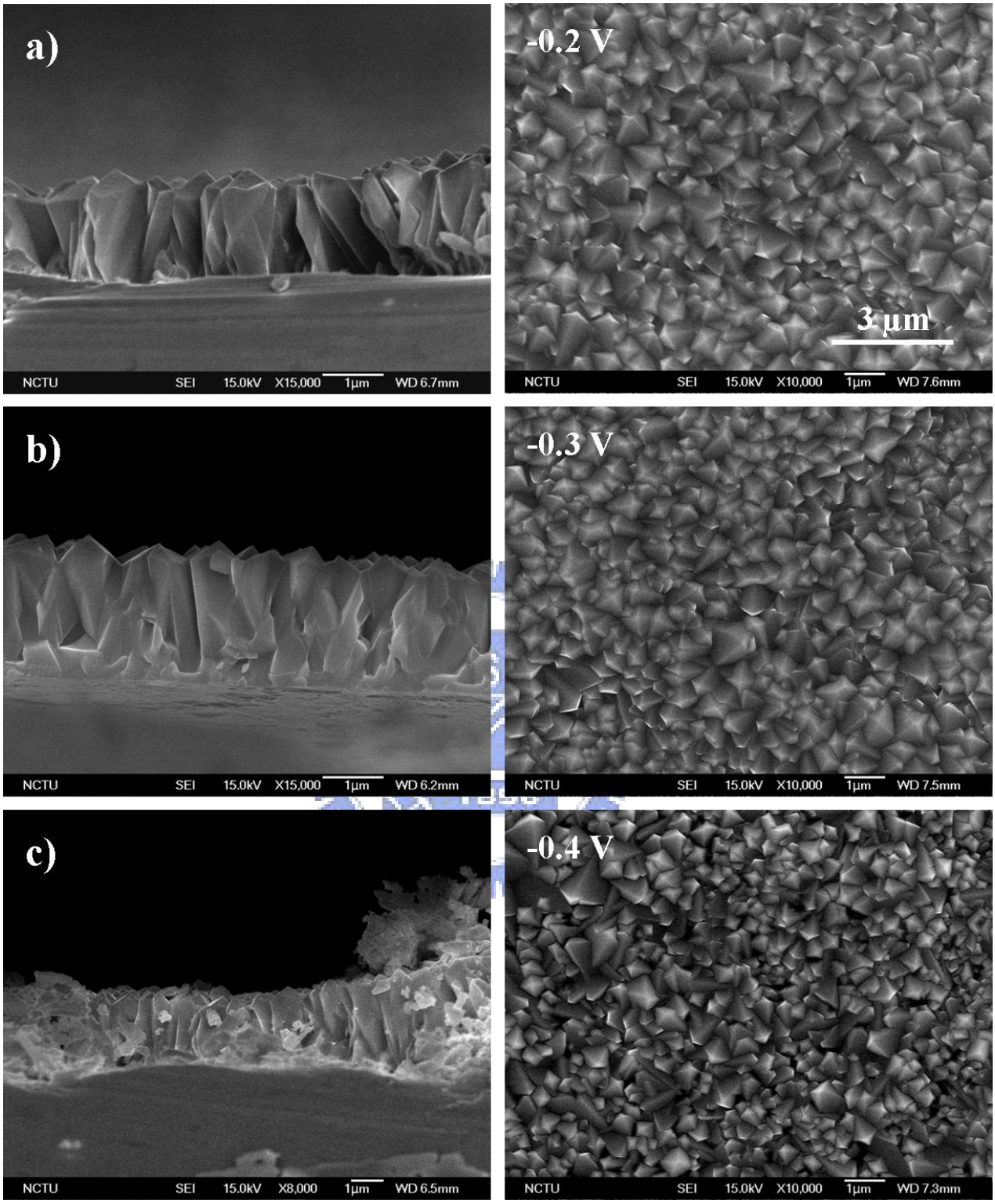

Figure 3.7 Cross-sectional SEM images of Cu_2O films electrodeposited in pH 9 bath for 60 min at a) -0.2, b) -0.3, and c) -0.4 V (vs. Ag/AgCl).

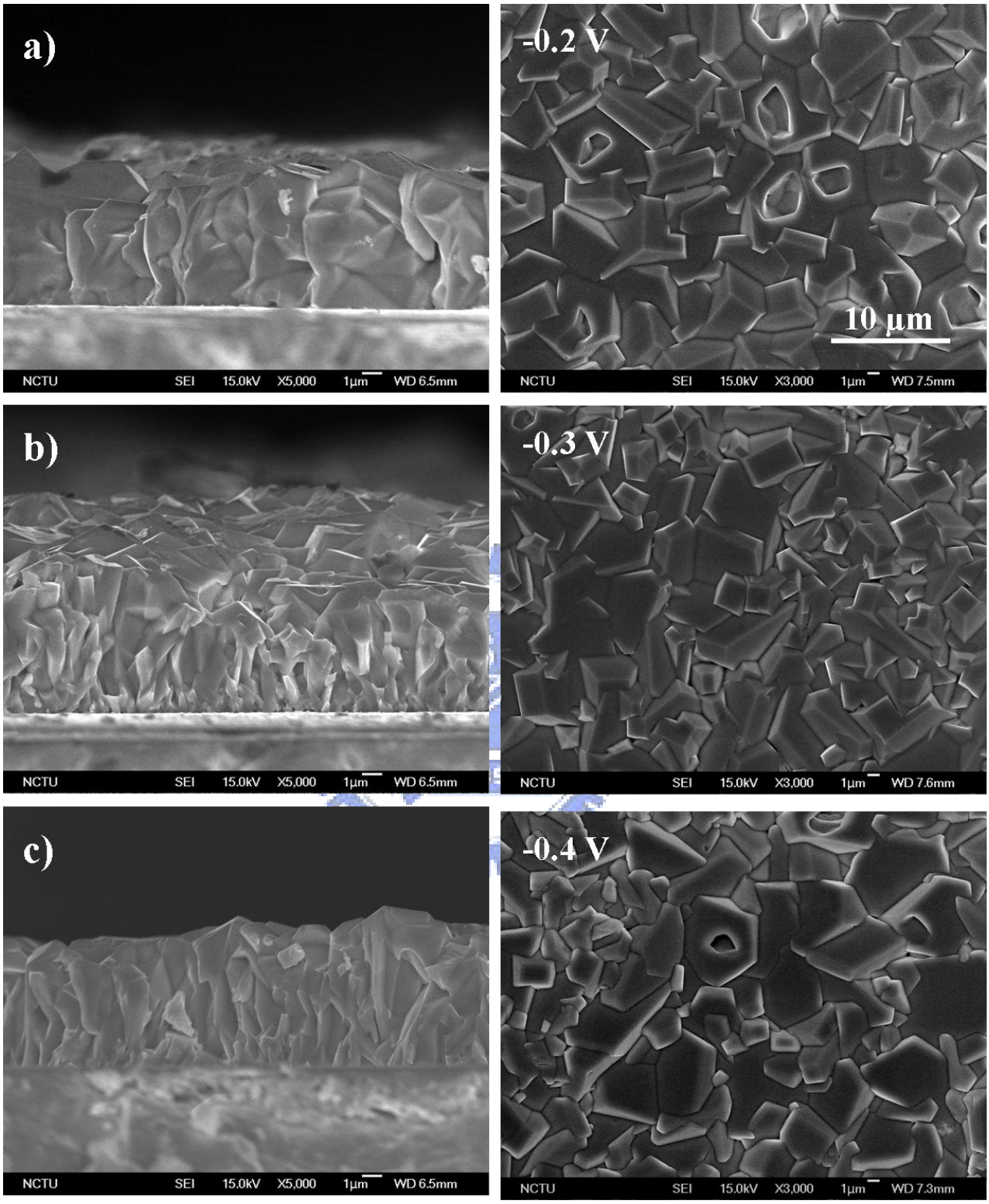

Figure 3.8 Cross-sectional SEM images of Cu_2O films electrodeposited in pH 11 bath for 60 min at a) -0.2, b) -0.3, and c) -0.4 V (vs. Ag/AgCl).

3.3.2. Annealed Cuprous Oxide Films

A. Effect of annealing temperatures

The annealed Cu_2O films were first examined by XRD in order to determine the stability of Cu_2O after heat treatments. The XRD results of pH 9 and 11 Cu_2O films annealed in different temperatures for 30 min are presented in Fig 3.9 and 3.10. We did not observe any impurity in both two kinds of films, inferring stability for the Cu_2O.

However, when the temperature was increased to 450 ℃, there was several diffraction peaks present as shown in Fig 3.11. The peaks located at 35° and 38° were (002) and (111) of CuO. This indicated that the Cu_2O would be oxidized at temperature higher than 350 ℃. The broadening backgrounds were caused by the stainless steel, which was exposed due to fall off of Cu_2O film after annealing. Formation of CuO distorted the lattice structure of Cu_2O and broke the film. This suggested that the Cu_2O was stable thermally up to 350 ℃.

The SEM images (Fig 3.12) demonstrate morphologies evolution induced by temperatures. The annealed pH 9 films looked similarly from 150 to 250 ℃. However, the grains were somewhat melted and connected to each other when the temperature was increased to 300 ℃. Apparently, the morphology became smoother and the grain boundary became indistinguishable as the temperature was raised up to 300 and 350 ℃. It suggested that there was a structural transition, despite lack of notable change from the XRD patterns. We calculated the crystal size by Scherrer's formula from XRD data. The crystal size of pH 9 films annealed at 150, 200, 250, 300, and 350 ℃ for 30 min were 26.4, 25.9, 26.0, 17.7, 17.6, and 20.1 nm, respectively. The as-deposited pH 9 film revealed a grain size about 21.4 nm. The crystal size was

slightly reduced, which could be caused by possible structural transition. Evolution in resistivity induced by annealing is presented in Fig 3.13. The resistivities values were decreasing as the temperature was increased. Its value decreased substantially when the temperature was increased to 350 ℃. The resistivity of pH 9 as-deposited film was 0.206 log (Ωcm) and then decreased to -3,402 log (Ωcm) after annealing at 350 ℃ for 30 min. The resistivity decreased about three magnitudes of orders. The results implied that the grain size was less-affected on the resistivity of pH 9 films, and the annealing process apparently improved the conductivity of the electrodeposited Cu_2O film. Relevant crystal size and resistivity variation of pH 9 films with different annealing temperatures are summarized in Table 3.1.

On the other hand, the grain size of pH 11 films appeared decreased and became rough after annealing (Fig 3.14). The as-deposited Cu_2O film had the smoothest structure, and the grains after annealing became sharp with increased grain boundaries. These results suggested that there was a structural transition possibly at 300 ℃, which was similar to the pH 9 films. However, their morphologies were obviously different. The grain sizes calculated from XRD were 27.5, 22.0, 20.3, 19.0, and 16.3 nm at different temperatures for 30 min. The as-deposited pH 11 film with grain size about 32.1 nm. This result implied that the crystal size of pH 11 films was decreased, which agreed well with the transition we observed from the SEM images. Furthermore, the resistivities of pH 11 films were increasing as the temperature increased except the sample annealed at 350 ℃ (Fig 3.15). The resistivity for the as-deposited pH 11 films was acceptable at -3.318 log (Ωcm). However, the annealing process did not improve its conductivity at all. Our results suggested that the possible structural transition after annealing caused the reduced grain size decreased, that lead to the smaller conductivity decreased. Relevant crystal size and resistivity variation of pH 11 films with different annealing temperatures are summarized in Table 3.2.

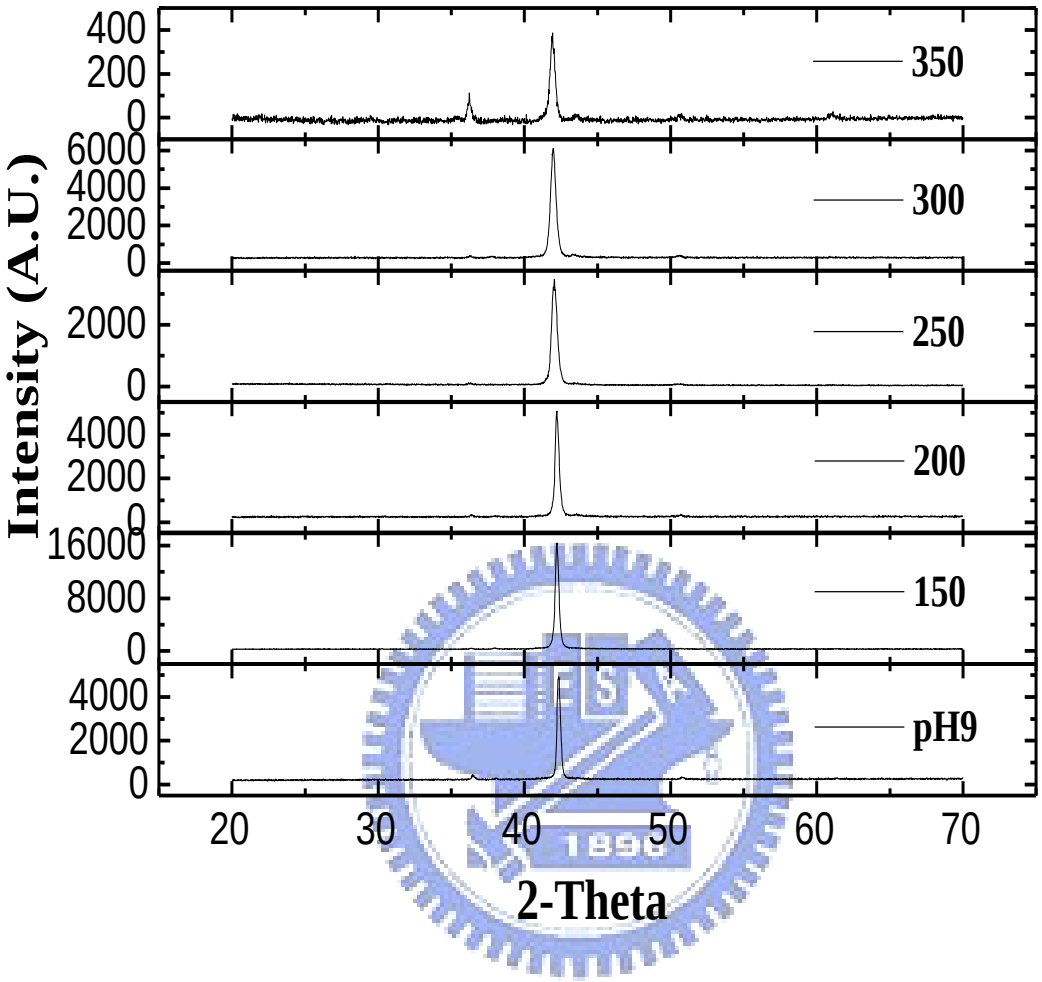

Figure 3.9 XRD patterns of Cu_2O films electrodeposited in pH 9 bath annealed for 30 min in temperatures from 150 to 350 ℃.

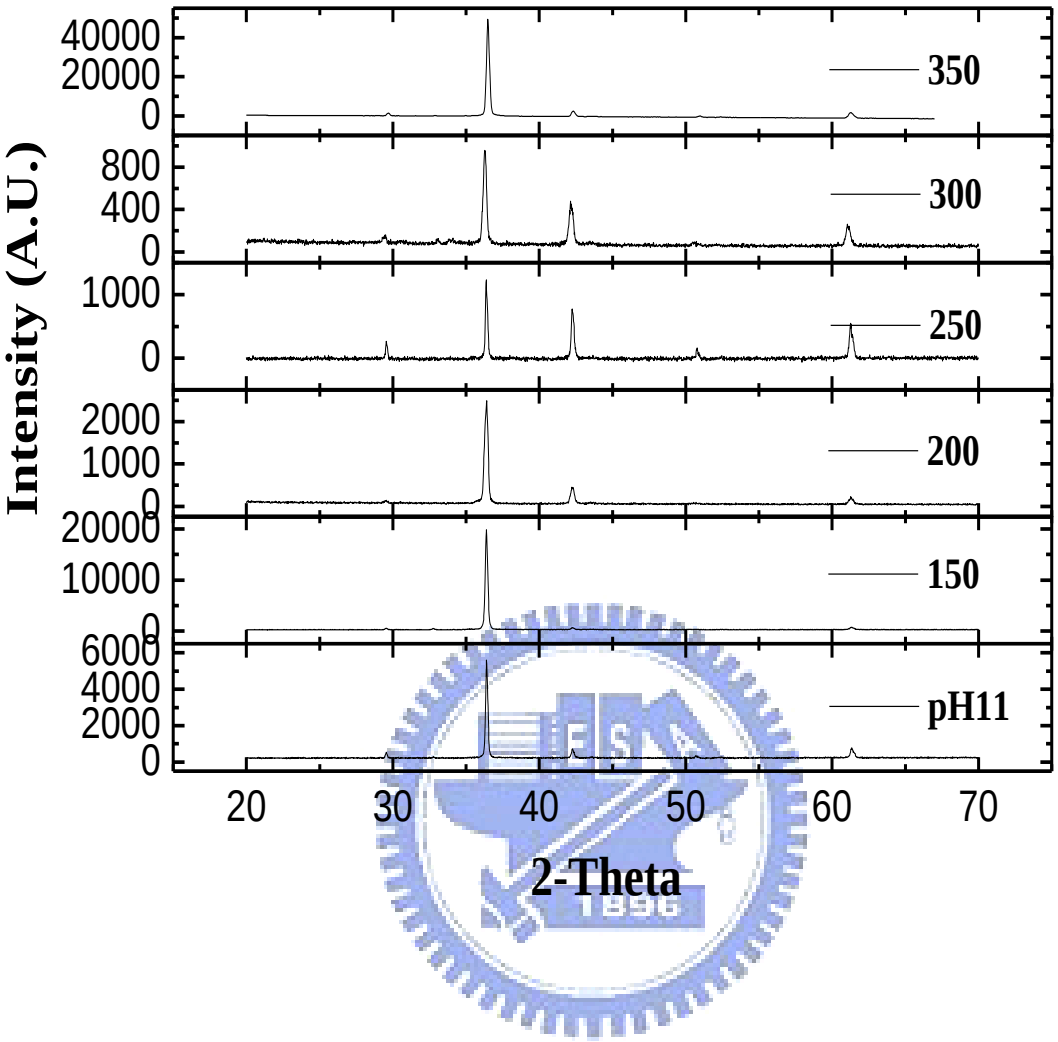

Figure 3.10 XRD patterns of Cu_2O films electrodeposited in pH 11 bath annealed 30 min in temperatures from 150 to 350 ℃.

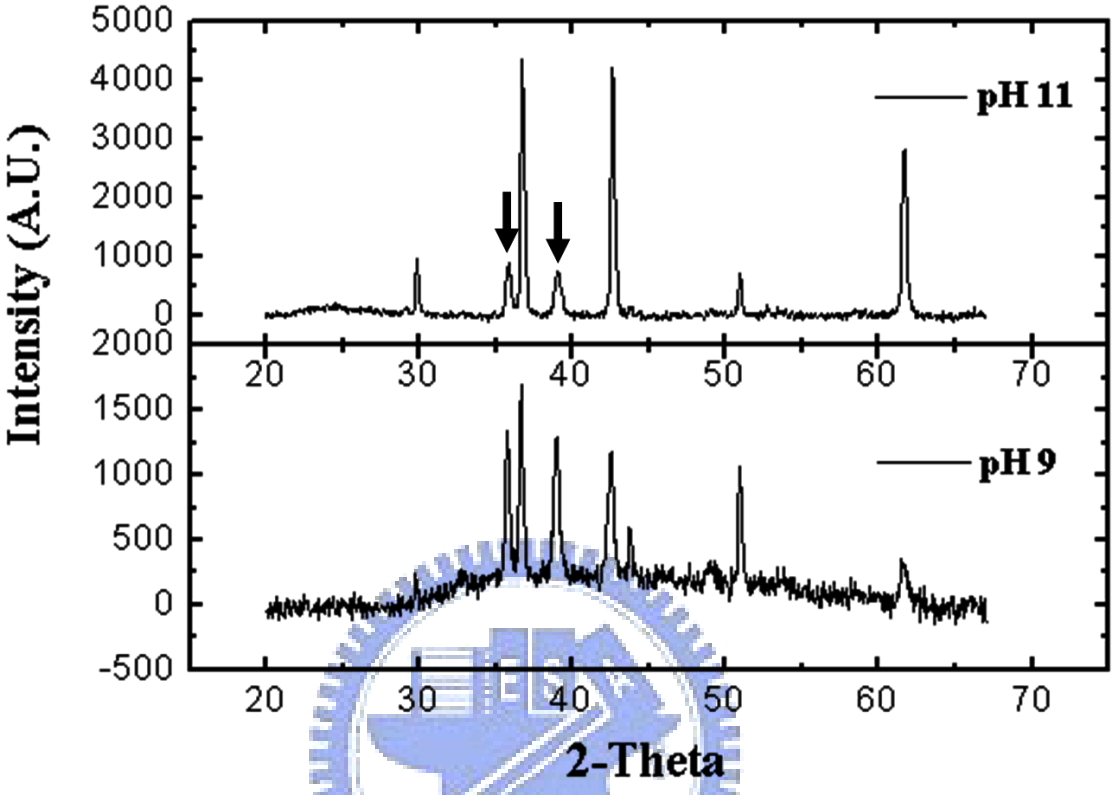

Figure 3.11 XRD patterns of Cu_2O film electrodeposited in pH 9 and 11 bath annealed in 450 ℃ for 10 min.

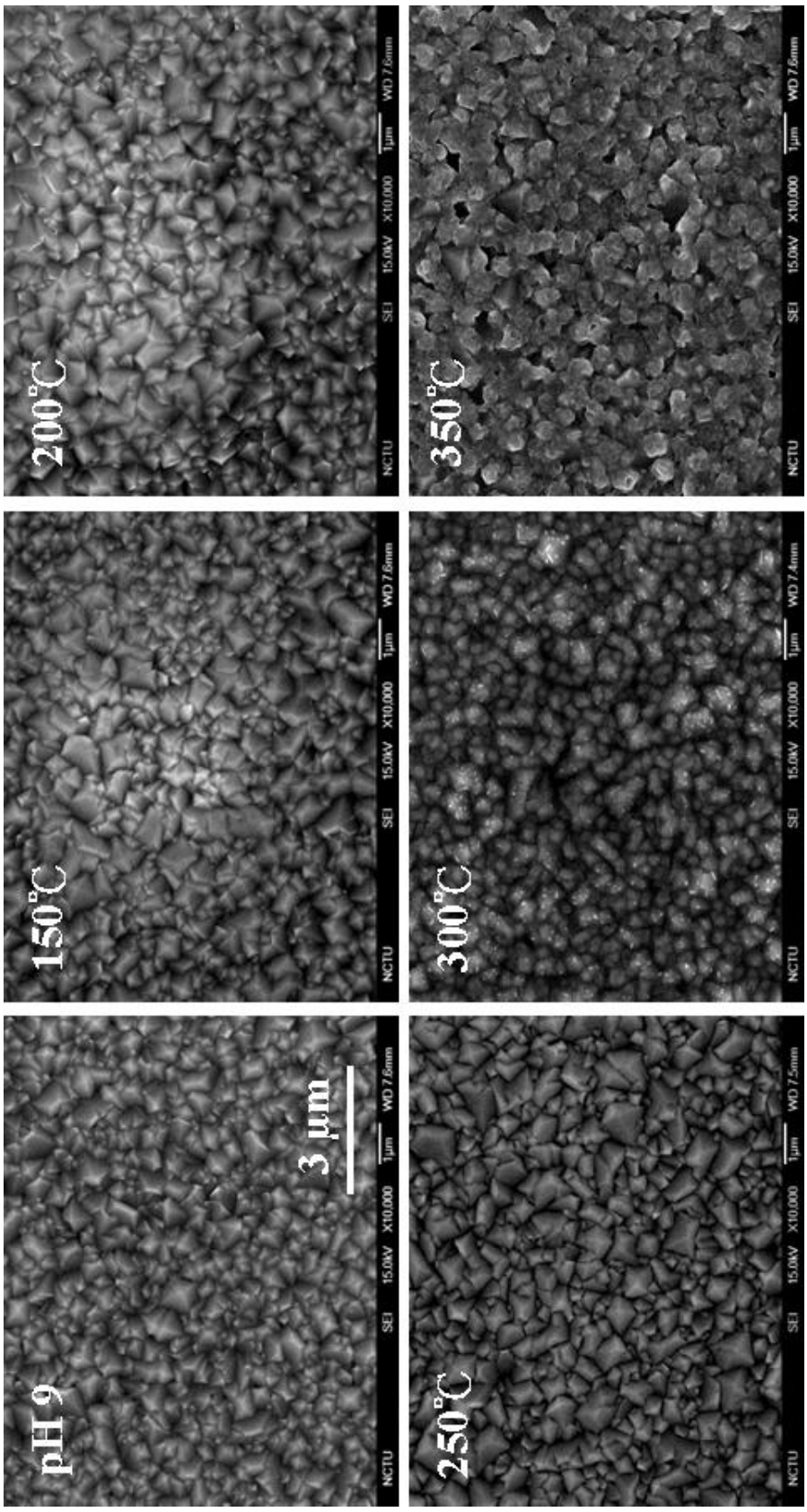

Figure 3.12 SEM images of Cu_2O film electrodeposited in pH 9 bath and annealed at different temperatures for 30 min.

Table 3.1 Crystal size (nm) and resistivity (log (Ω cm)) of Cu_2O pH 9 films annealed in different temperatures for 30 min.

pH 9	As-deposited	150 ℃	200 ℃	250 ℃	300 ℃	350 ℃
Crystal size	26.4	25.0	26.0	17.7	17.6	20.1
Resistivity	0.206	0.162	0.099	-0.108	-0.438	-3.402

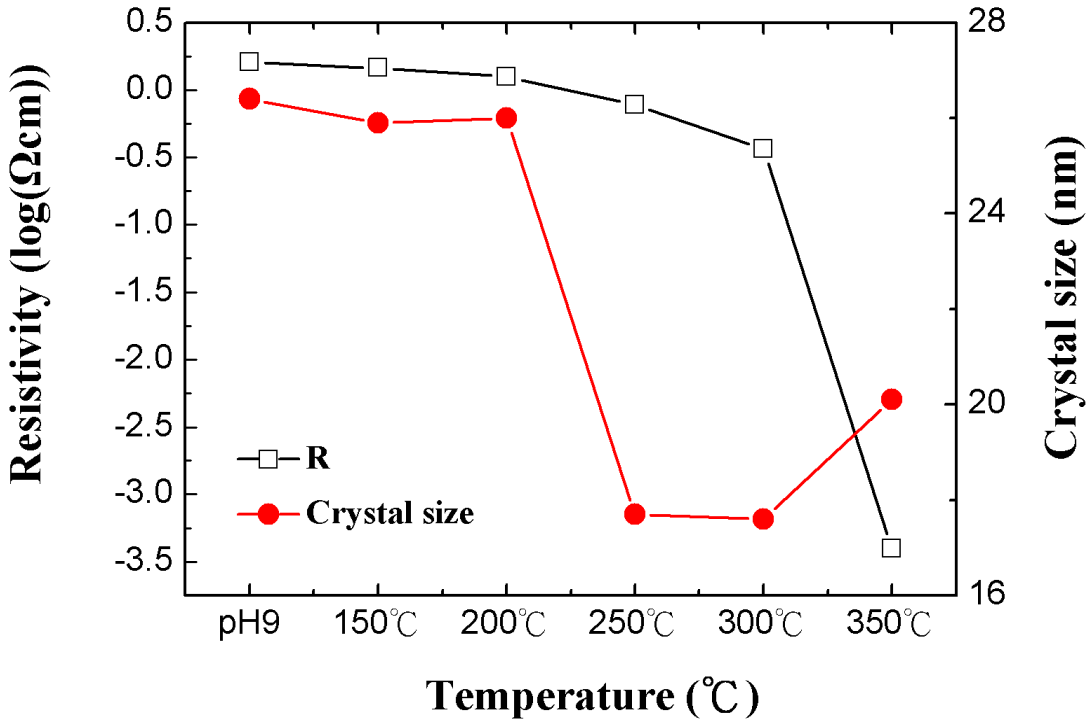

Figure 3.13 Variation of resistivity and crystal size of Cu_2O pH 9 films with annealing temperatures.

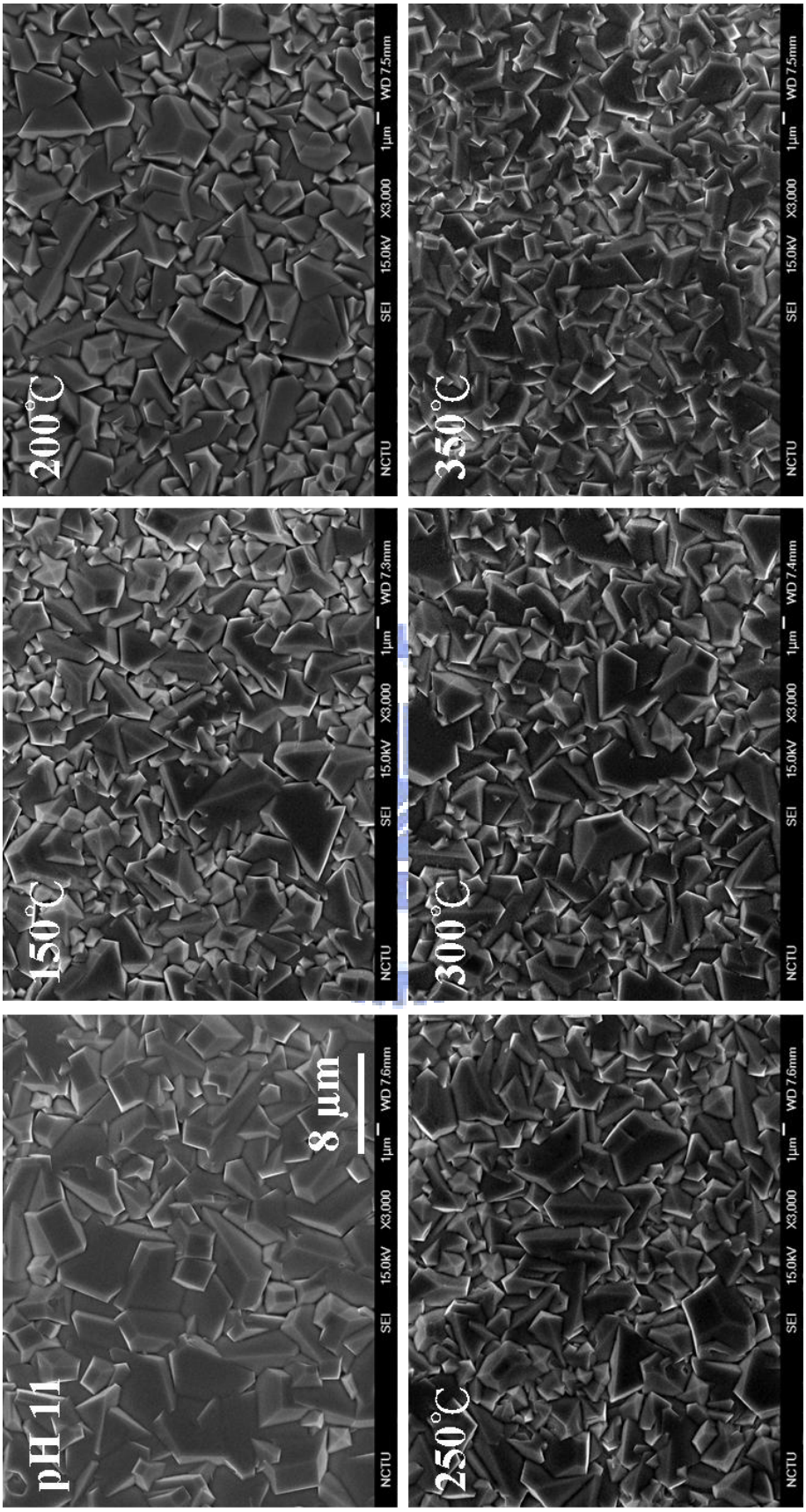

Figure 3.14 SEM images of Cu_2O film electrodeposited in pH 11 bath and annealed at different temperatures for 30 min.

Table 3.2 Crystal size (nm) and resistivity (log (Ω cm)) of Cu_2O pH 11 films annealed in different temperatures for 30 min.

pH 11	As-deposited	150 ℃	200 ℃	250 ℃	300 ℃	350 ℃
Crystal size	32.1	27.5	22.0	20.3	19.0	16.3
Resistivity	-3.318	-2.509	-2.304	-1.944	-1.783	-1.879

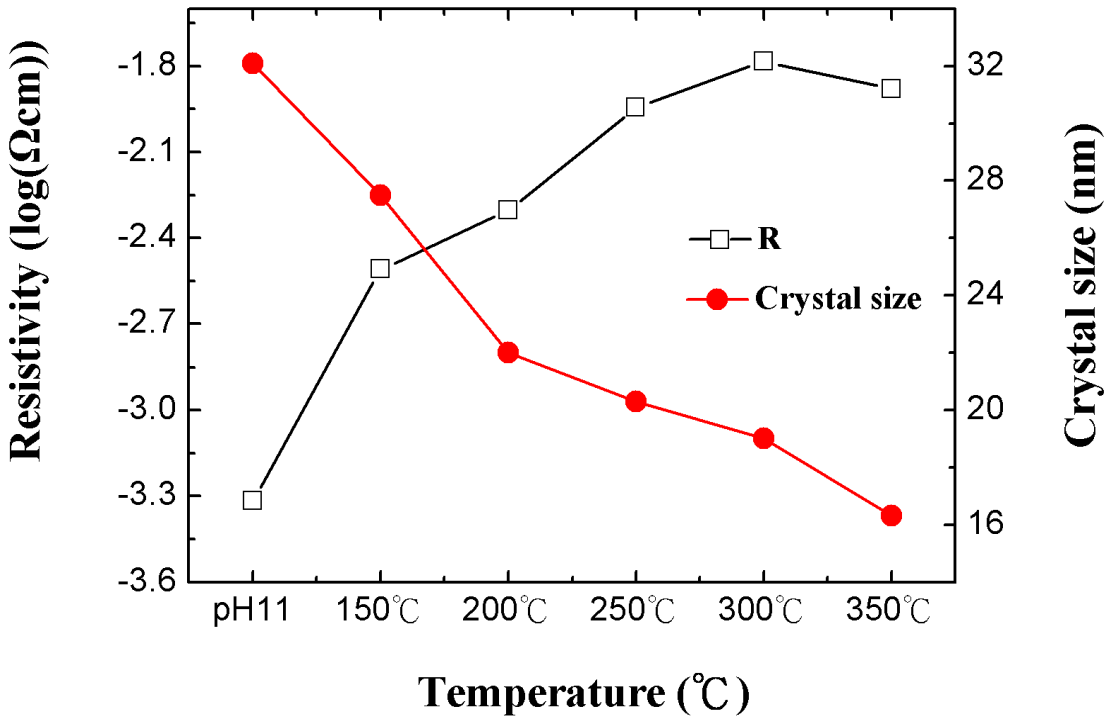

Figure 3.15 Variation of resistivity and crystal size of Cu_2O pH 11 films with annealing temperatures.

B. Effect of annealing times

The annealing time effect for the Cu_2O revealed negligible change at lower temperatures. However, as the temperature was increased, the annealing time effect became notable. Here we discussed the films annealed in 350 ℃. The XRD of Cu_2O films annealing for 10, 30, and 60 min at 350 ℃ are presented in Fig 3.16 and 3.17. As the time was increased, the Cu_2O films were still stable and did not oxidize to CuO.

The SEM images of Cu_2O films annealing for 10, 30, and 60 min at 350 ℃ are presented in Fig 3.18 and 3.19. The morphology of pH 9 film annealed for 10 min revealed possibly melted and rejoined grains, when the annealing time was increased to 30 min, the grains were all mixed up but with a smaller and irregular grain boundary. When the time was extended to 60 min, the grain looked re-crystallized on the surface but the edge became sharp again. The results suggested a possible structural transition. However, the preferred orientation of pH 9 film did not change upon annealing. On the hand, the pH 11 films annealed for 10 and 30 min did not produce any difference in their morphology. When the annealing time was extended to 60 min, the grains became melted together and their boundaries appeared irregular.

The resistivity of Cu_2O films after annealing at different temperatures and time are presented in Fig 3.20 and 3.21. The resistivity of pH 9 films showed notable improvement after annealing 30 min. When the annealing time was extended to 60 min, the resistivity was increased at 300 and 350 ℃ (Fig 3.20). The results implied that the annealing process successfully reduced the defects inside the Cu_2O lattice. However, the annealing process also induced possible a structural transition which reduced the grain size of Cu_2O film and caused the resistivity increased. The resistivity of pH 9 films varied with different temperatures and annealing times are

summarized in Table 3.3.

The resistivity variation of pH 11 films revealed an opposite trend to that of pH 9 films (Fig 3.21). The resistivity was increased at first and then decreased at 350 ℃. These results were likely caused by structural transition at 350 ℃. The resistivity of pH 11 films annealing at different temperatures and annealing times are summarized in Table 3.4.

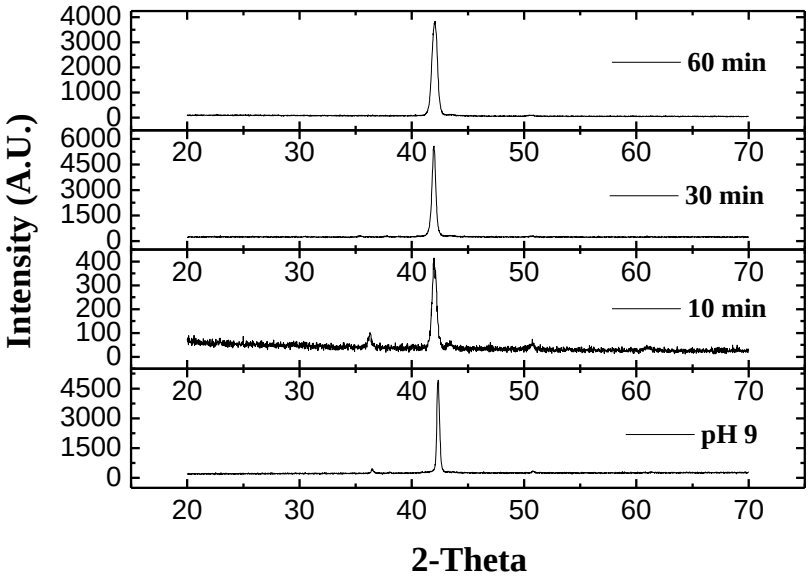

Figure 3.16 XRD patterns of Cu_2O films deposited in pH 9 annealed at 350 ℃ for 10, 30, and 60 min.

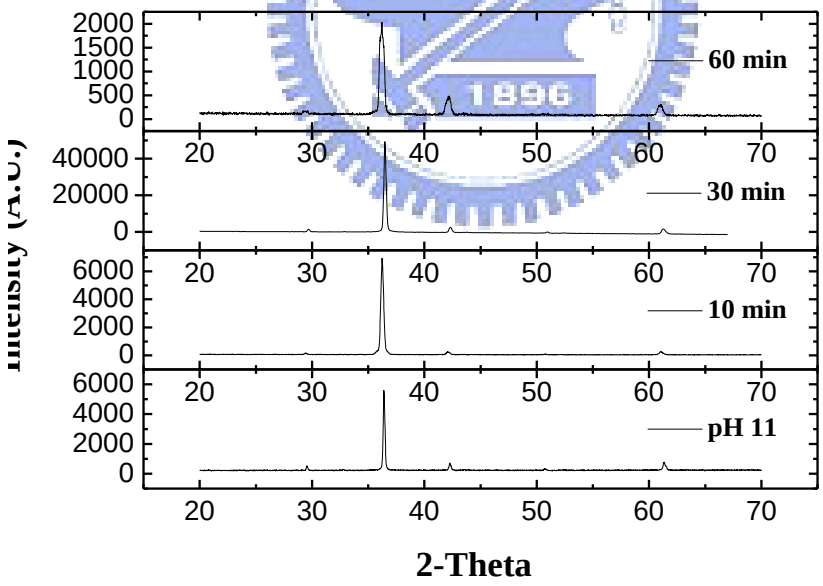

Figure 3.17 XRD patterns of Cu_2O films deposited in pH 11 annealed at 350 ℃ for 10, 30, and 60 min.

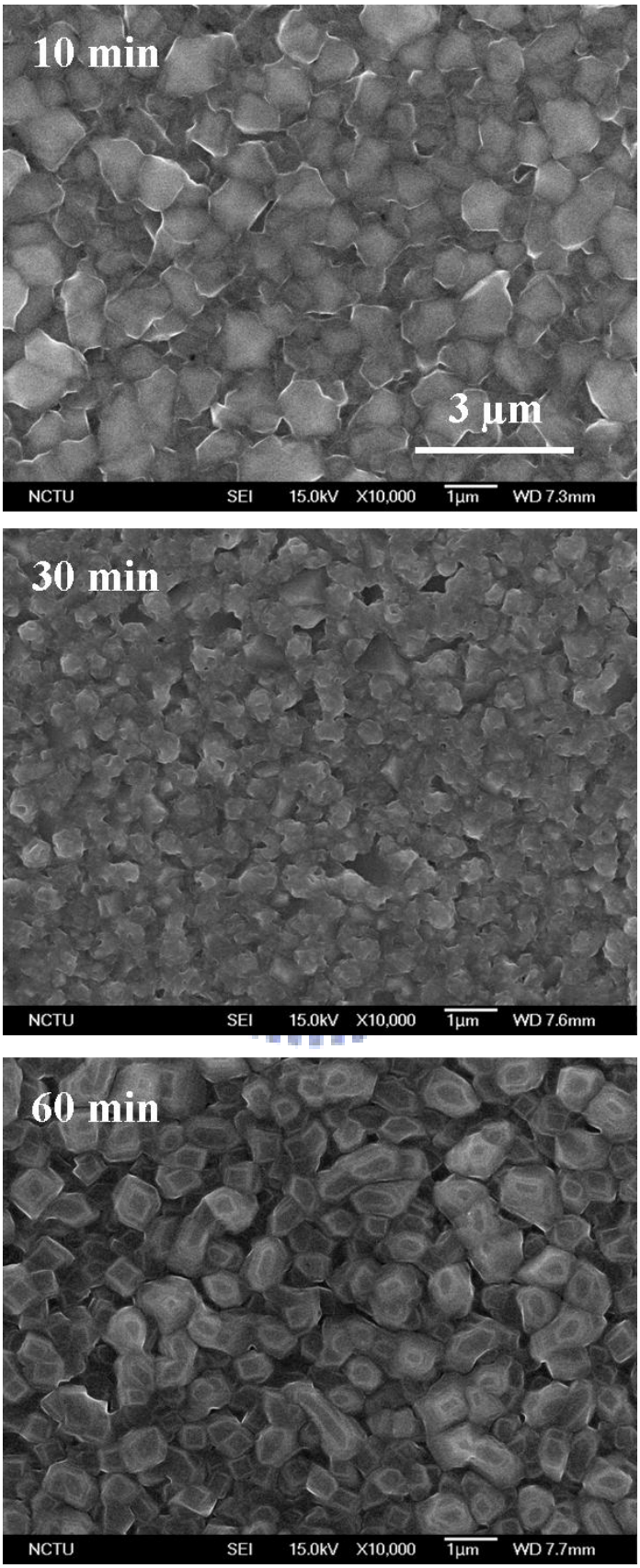

Figure 3.18 SEM images of Cu_2O film electrodeposited in pH 9 bath and annealed in 350 ℃ and with 10, 30, and 60 min.

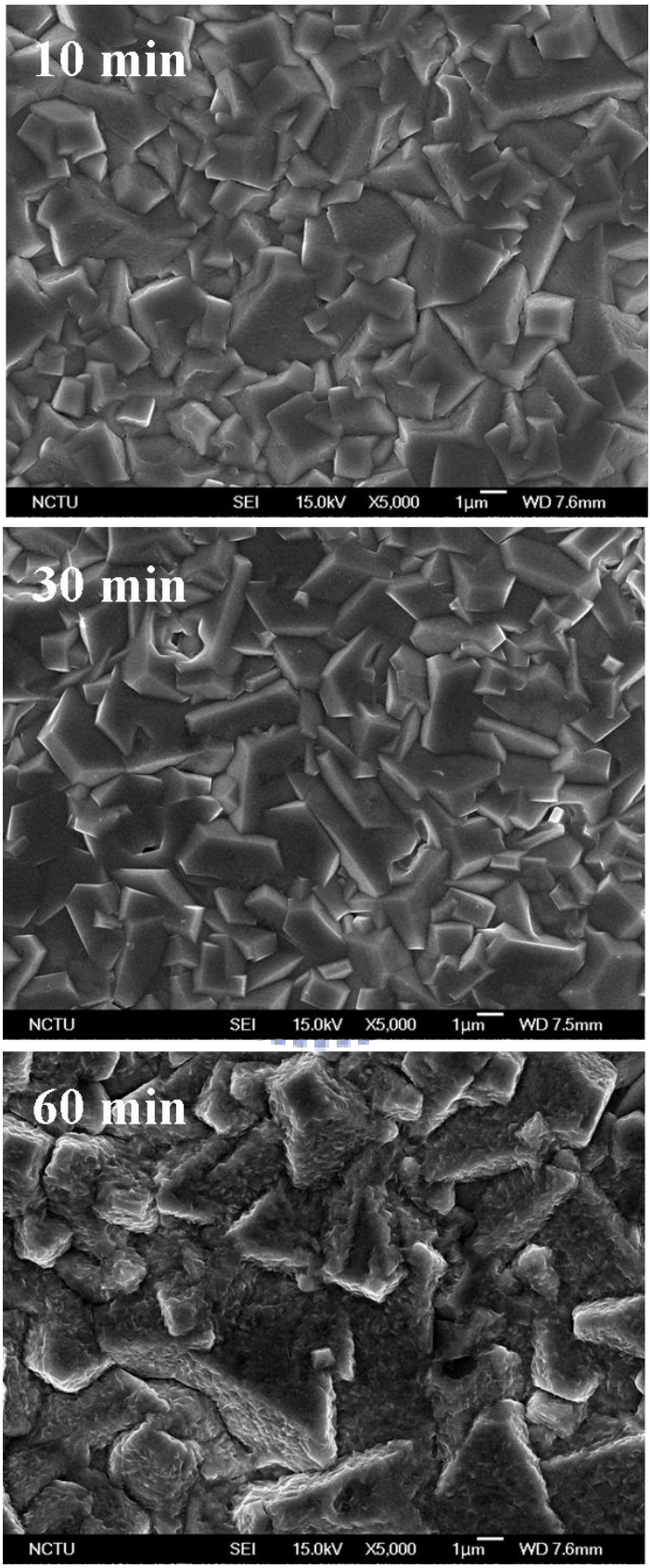

Figure 3.19 SEM images of Cu_2O film electrodeposited in pH 11 bath and annealed in 350 ℃ and with 10, 30, and 60 min.

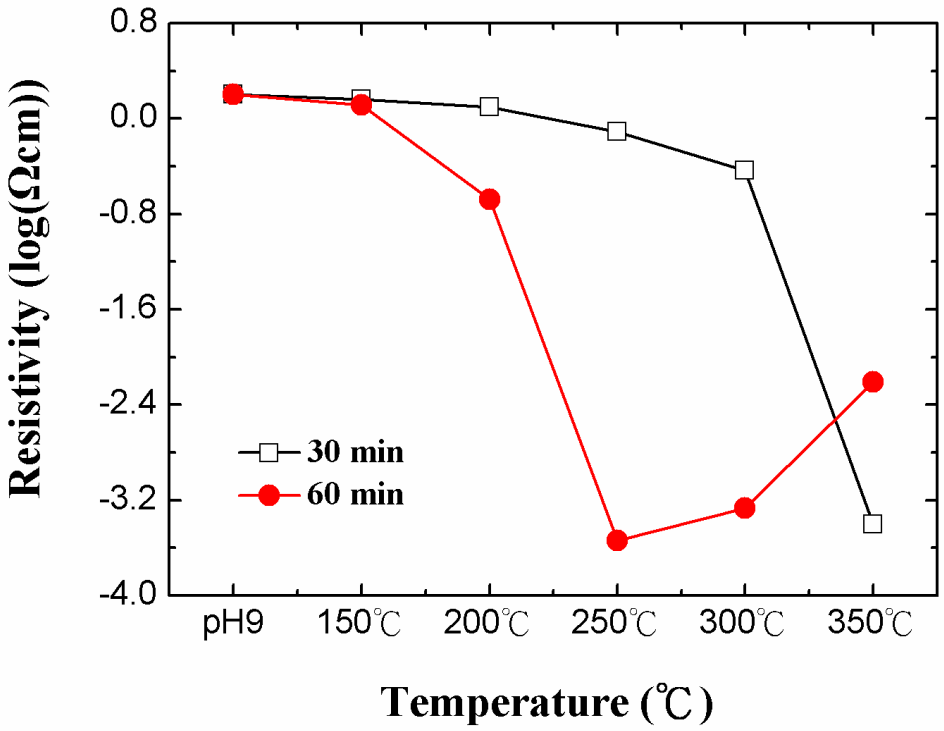

Figure 3.20 Resistivity for the Cu_2O films from pH 9 that was annealed for different time; annealed for 30 (solid symbols) and 60 min (open symbols), respectively.

Table 3.3 Resistivity (log (Ω cm)) of Cu_2O pH 9 films annealed in different temperatures for 30 and 60 min.

pH 9	As-deposited	150 ℃	200 ℃	250 ℃	300 ℃	350 ℃
30 min	0.206	0.162	0.099	-0.108	-0.438	-3.402
60 min	0.206	0.115	-0.675	-3.538	-3.270	-2.212

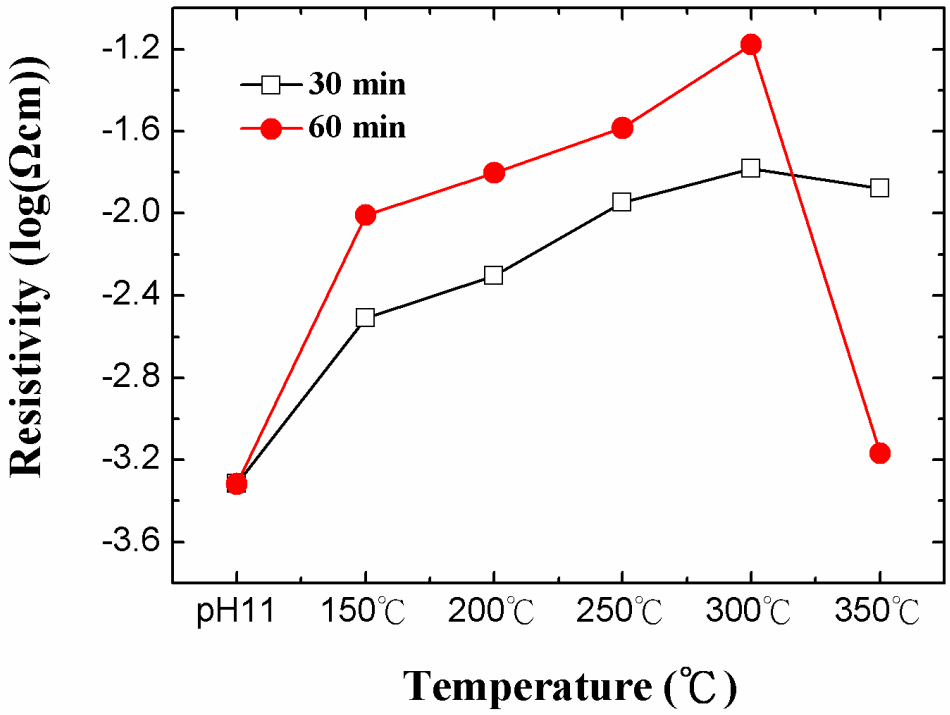

Figure 3.21 Resistivity for the Cu_2O films from pH 11 that was annealed for different time; annealed for 30 (solid symbols) and 60 min (open symbols), respectively.

Table 3.4 Resistivity (log (Ω cm)) of Cu_2O pH 11 films annealed in different temperatures for 30 and 60 min.

pH 11	As-deposited	150 ℃	200 ℃	250 ℃	300 ℃	350 ℃
30 min	-3.318	-2.509	-2.304	-1.944	-1.783	-1.879
60 min	-3.318	-2.008	-1.801	-1.585	-1.178	-3.167

3.4. Conclusions

The annealing effect in our system did not increase the grain size as we hoped. There was a possible structural transition. The Cu_2O films after annealing revealed reduced grain size and notable morphology change. The resistivity for the pH 9 films was decreased, but the resistivity for the pH 11 films was increased. However, both films improved their conductivity at 350 ℃. The resistivity of pH 9 film annealed at 350 ℃ for 30 min had the best conductivity with a resistivity of 3.96×10^{-4} Ωcm. Its conductivity was even better than the pH 11 films.

Chapter 4

Photoelectrochemical Properties of Cuprous Oxide

4.1. Introduction

Results from material characterizations on the Cu_2O films have been discussed in chapter 3. Their photoelectrochemical properties are presented here. We studied the hydrogen evolution capability of Cu_2O films using a semiconductor-electrolyte cell, and evaluated its stability under extensive light illumination.

4.2. Experimental

4.2.1. Setup

Photoelectrochemical analysis was conducted by a three-electrode arrangement. The Cu_2O films discussed in Chapter 3 were served as the working electrode. We used a platinum foil and Ag/AgCl (KCl saturated) as the counter and reference electrode, respectively. The electrolyte was 0.5 M Na_2SO_4 solution, which is commonly used in a semiconductor-electrolyte cell or water splitting reaction. The electrolyte was pre-purged with N_2 gas for 30 min before the measurement in order to eliminate any impurity or oxidant in the electrolyte. A 100 W halogen lamp (OSRAM, HLX64625) was used as the light source and it was positioned at 15 cm away from the working electrode. The photocurrent was detected by a SOLAR TRON-SIC1287. Fig 4.1

provide the photograph of the photoelectrochemical setup.

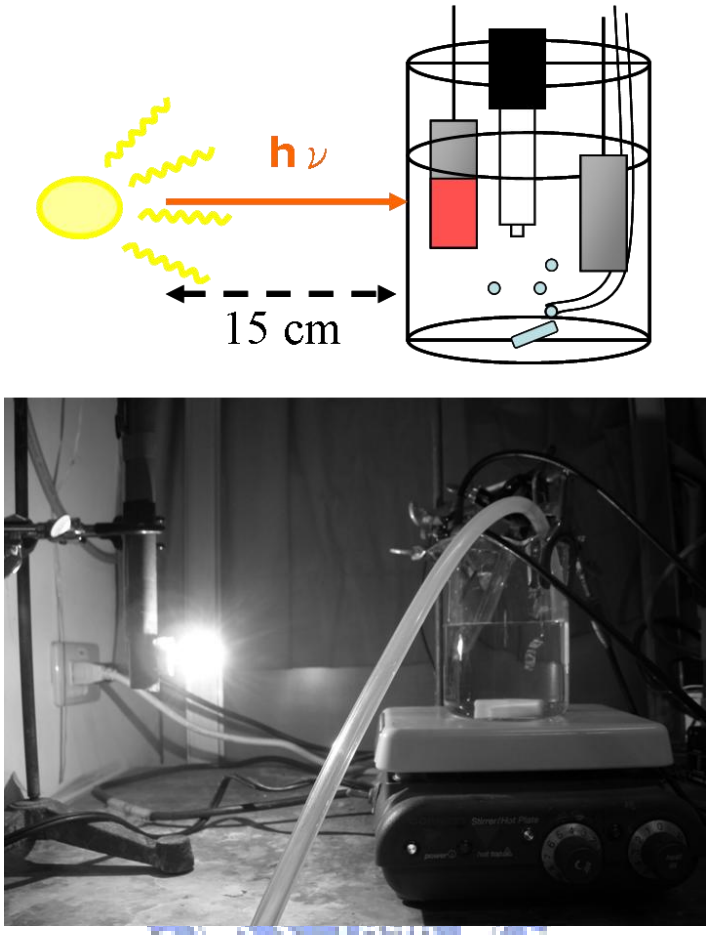

Figure 4.1 The scheme and the photoelectrochemical setup.

4.2.2. Photoelectrochemical measurement

The photoelectrochemical properties of Cu_2O were recorded by illuminating the Cu_2O films under a constant bias of -0.3 V (versus Ag/AgCl) for 1 h. The supporting bias was employed because the established inefficiency of Cu_2O to oxidize water according to previous studies. It is noted that from previous studies, the Cu_2O was stable under this bias. The range of potentiodynamic analysis started from 0 to -0.8 V (vs. Ag/AgCl) at a 5 $mVsec^{-1}$ scanning rate and the light was chopped every 5 sec. Evaluation on the stability was carried out in potentiostatic measurement under -0.3 V for 5 h.

4.3. Results and discussion

4.3.1. As-deposited cuprous oxide film

A. Stability Test

The stability of Cu_2O is always a concern. Because of possible chemical dissolution, photolysis of water using the Cu_2O was still being debated. Therefore, validation of the stability of Cu_2O in our system was the first thing we needed. We examined its stability by performing a long term stability test. We measured the photocurrent of Cu_2O films with or without illumination and supplied a -0.3 V (vs. Ag/AgCl) bias for 5 h. The results are presented in Fig 4.2. The fluctuating currents in both Fig 4.2a and 4.2b were the dark currents for the as-deposited pH 9 and 11 film, respectively. They were measured under -0.3 V without illumination. We observed that only under a constant illumination we revealed a stable output. Both pH 9 and pH 11 films exhibited a stable output with negligible degradation for at least for 5 h. The average current density for the films deposited from pH 9 and pH 11 were -29.4 and -66.5 μAcm^{-2}, respectively.

We examined the Cu_2O electrode after illumination by XRD and SEM. From XRD patterns presented in Fig 4.3a and Fig 4.4a, we did not observe any impurity from in both films. This indicated the Cu_2O films were stable in our electrolyte either with or without illumination. The stability of Cu_2O lasted at least for 5 h. The SEM images of pH 9 films (Fig 4.3b) exhibited no change either with or without illumination after for 5 h. The surface of pH 11 films (Fig 4.4b) appeared slightly corroded after the reaction, which may due to the vigorous output of photocurrent. Unfortunately, we did not find any differences from the XRD pattern.

a)

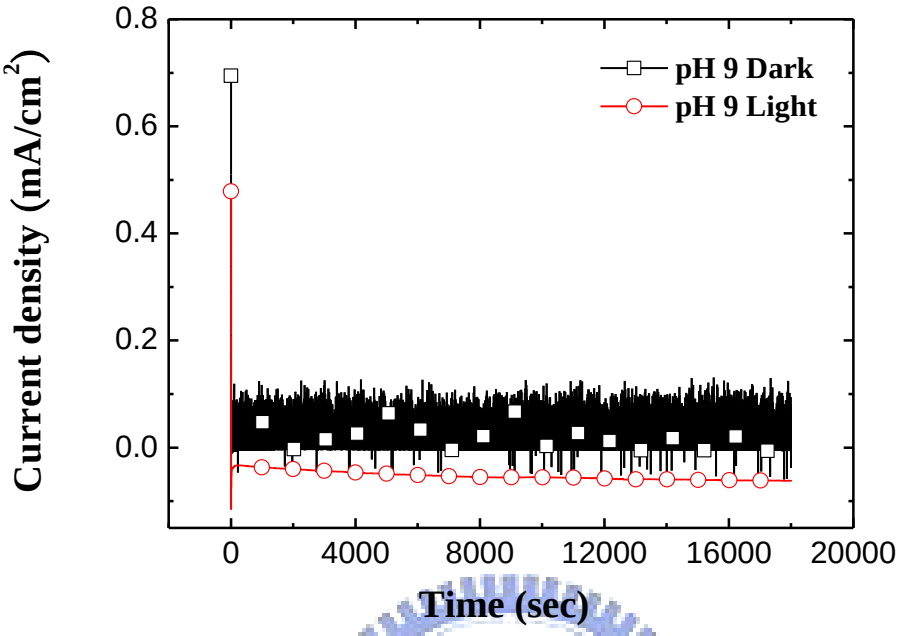

b)

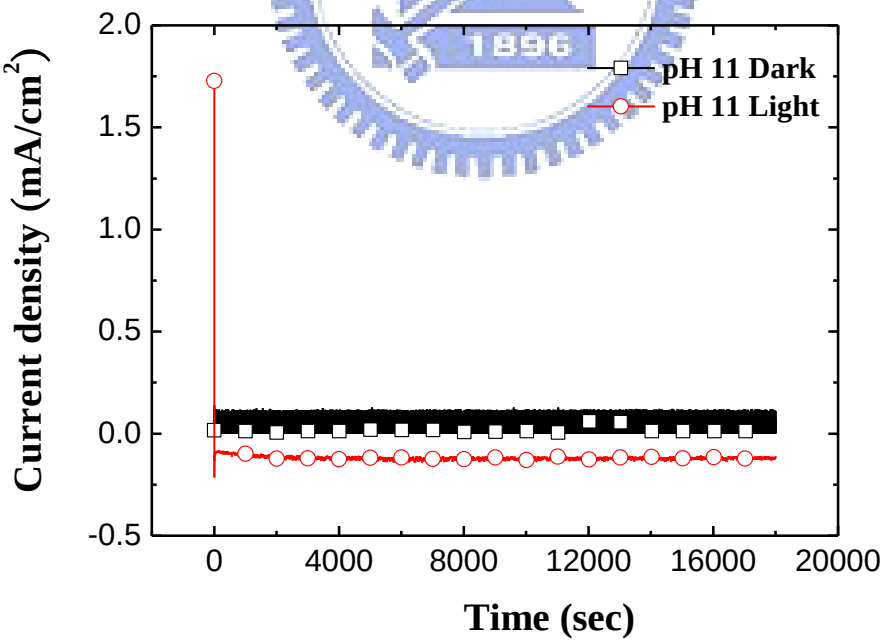

Figure 4.2 I-t curves of a) pH 9 and b) pH 11 films under potentiostatic measurements at -0.3 V for 5 h.

a)

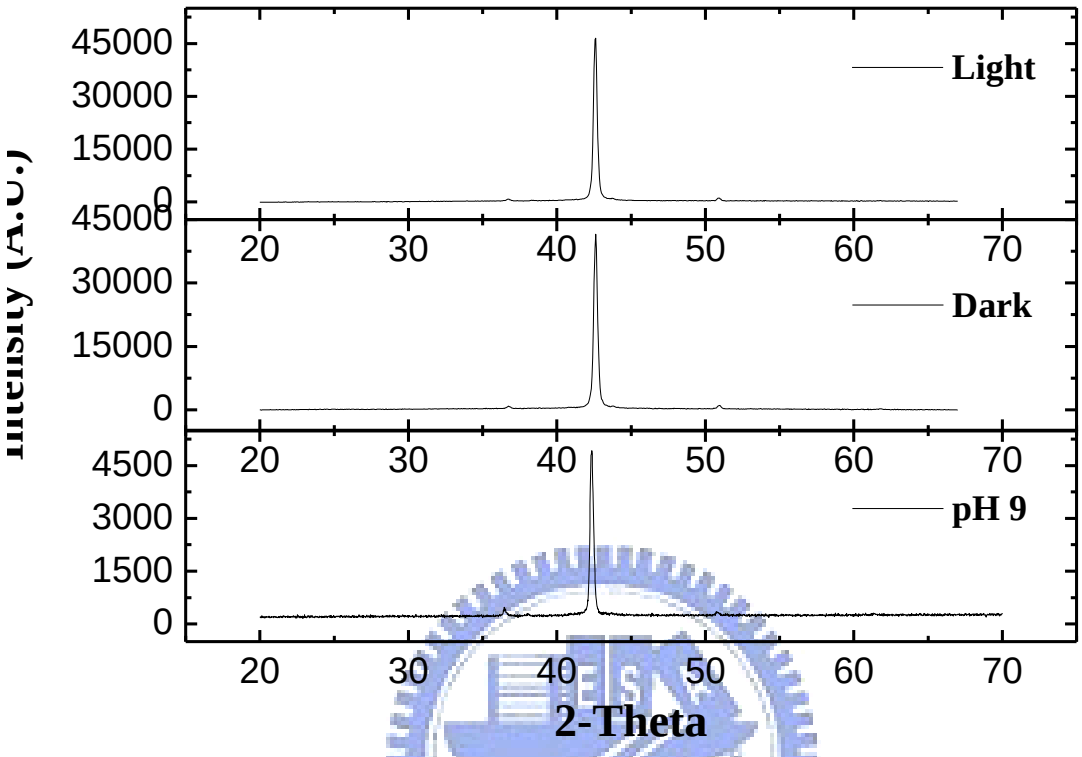

b)

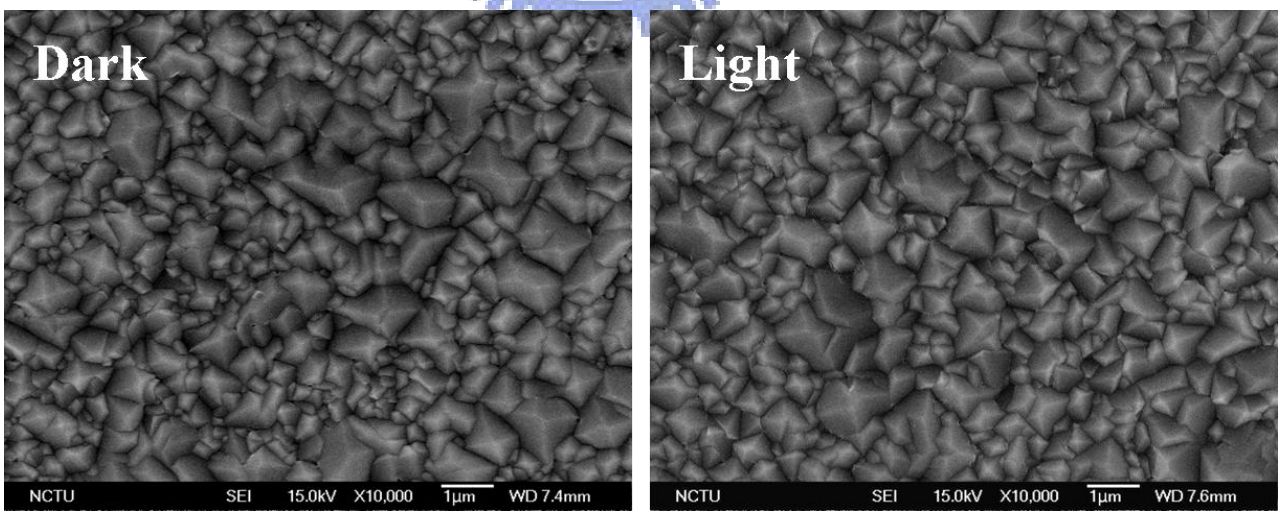

Fig 4.3 a) XRD patterns and b) SEM images of pH 9 films before and after potentiostatic measurements at -0.3 V for 5 h with and without illumination.

a)

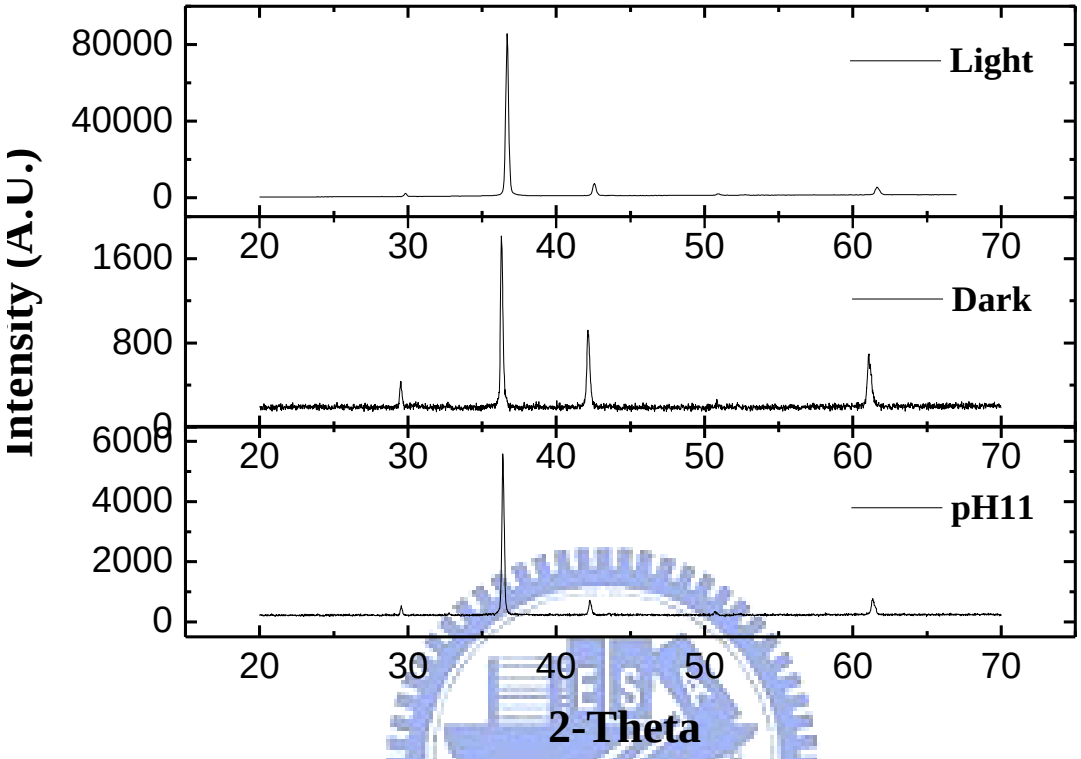

b)

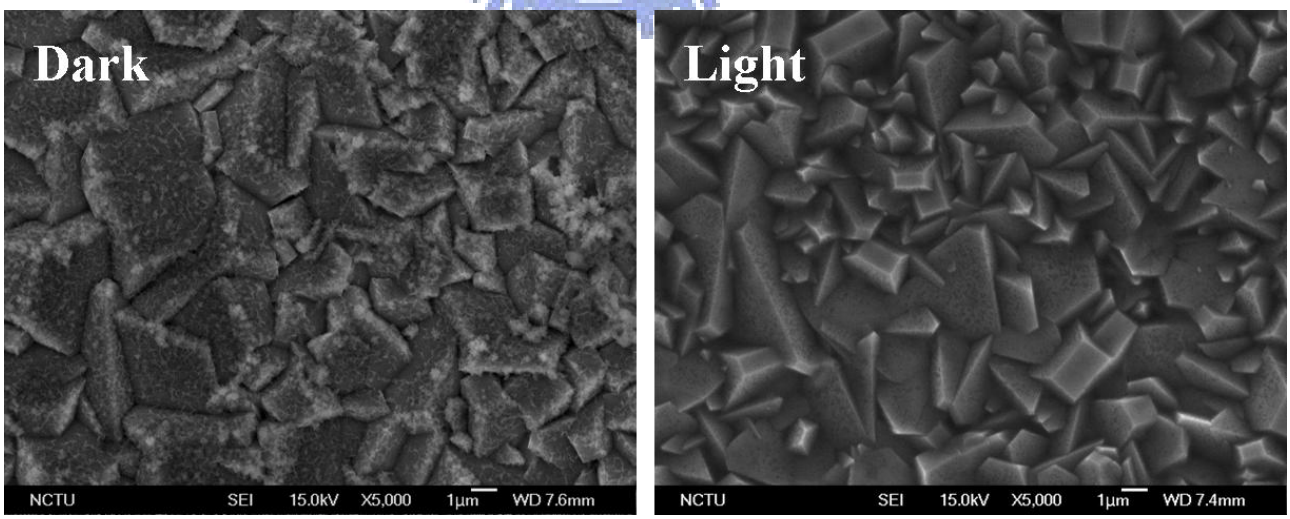

Fig 4.4 a) XRD patterns and b) SEM images of pH 11 films before and after potentiostatic measurements at -0.3 V for 5 h with and without illumination.

B. Photo-Responses Characterizations

The Cu_2O is a non-stoichiometic semiconductor. Its photoelectrochemical property depends on the concentration of copper vacancies and oxygen vacancies. The copper vacancies induced a p-type character and oxygen vacancies induced a n-type character. We electrodeposited the Cu_2O films in different pH environments which rendered different copper vacancies in the films. Furthermore, the process during electrodeposition had to be strictly controlled because the vacancies in the Cu_2O were changing easily. Not only the pH value was expected to affect the composition of Cu_2O, but also the deposition temperature, concentration of electrolyte, and any factors which were likely to affect the deposition rate and grain growth.

Comparison in the photoelectrochemical performances for the as-deposited pH 9 and pH 11 films under -0.3 V is shown in Fig 4.5. Both dark currents were fluctuating violently implying that the Cu_2O was inefficient to reduce H_2O without illumination at -0.3 V. This unsettled current output suggested that there were some reactions on the Cu_2O electrode surface. We observed that the photocurrents from films deposited in pH 11 bath had a better performance than that of pH 9 films. The results indicated the ability of photoelectrolysis water between these two films had a large distance. This implied that the Cu_2O electrodeposited in higher pH value could get a better performance.

The photocurrent of pH 11 film was much larger than the pH 9 film. This result may be due to the grain size differences in these two films. From Chapter 3, the grain size for the as-deposited pH 9 film was under 1 μm. On the other hand, the grain size for the pH 11 film was distributed from 1 to 8 μm. Most electron-hole recombination occurred at the grain boundary areas. It would reduce the energy conversion efficiency and also affect the conductivity of the semiconductor. Therefore, the grain

size could be the main effect affecting the efficiency. The resistivity measurements also agreed with this result. The resistivity for the as-deposited pH 9 and pH 11 films were 0.206 and -3.318 log (Ω cm), respectively.

Furthermore, the difference of Cu vacancy distribution should also be considered. However, the effect of vacancy distribution was hardly identified. The Cu_2O deposited in higher pH environment was expected to contain a higher concentration of O and had more Cu vacancies in its lattice, which exhibited a better p-type character. It might be another reason that the Cu_2O deposited in pH 11 bath had a better performance.

Additionally, in order to confirm how different the pH value of deposition bath would affect its photoelectrochemical properties, we prepared the films electrodeposited in the bath at pH 7. The photoelectrochemical properties of the Cu_2O electrodes were studied by a linear sweep voltammetry with chopped illumination (Fig 4.6). The results demonstrated that the films deposited in pH 11 bath had a strong response to light, implying that it was a well-fabricated p-type semiconductor. The films deposited in pH 9 and 7 exhibited steady responses with illumination until the bias was larger than -0.3 V, and the responses were both weak. However, the pH 9 film performed slightly better than pH 7. We concluded that the pH environment for electrodeposited Cu_2O was related to the structure and photoelectrochemical ability of Cu_2O. At a higher pH value, as a better p-type Cu_2O was obtained.

Unfortunately, we could not compare these two films directly in the following section. These two films had different preferred orientations and thicknesses. Their resistivities and grain sizes were also different. Therefore, the photocurrent for these two films after annealing treatments were not be compared together.

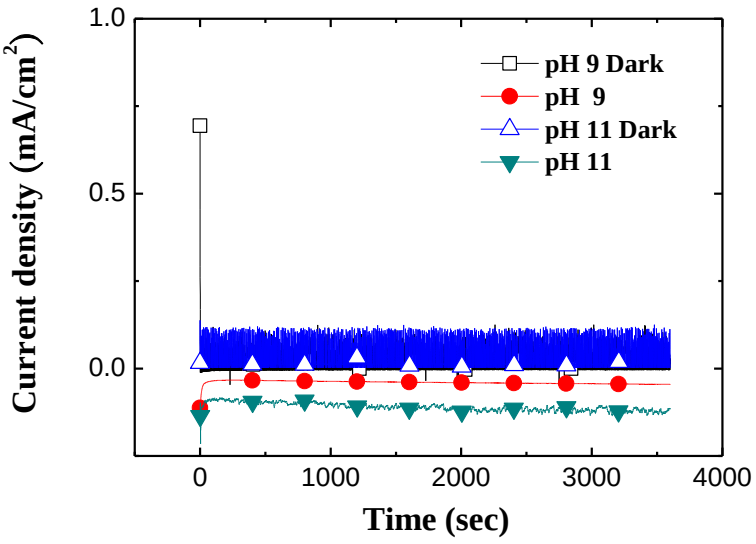

Figure 4.5 Potentiostatic curves of as-deposited pH 9 and 11 films under -0.3 V with or without illumination.

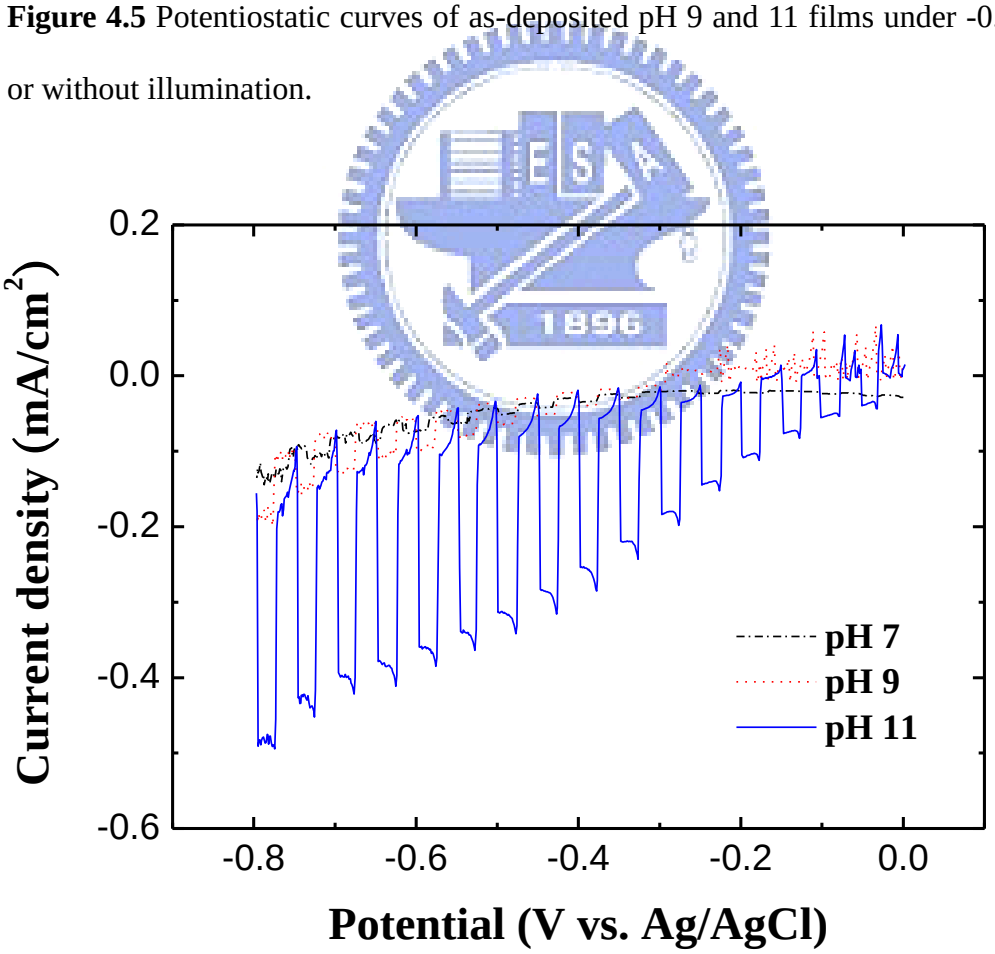

Figure 4.6 LSV curves with chopped illumination of pH 7, 9, and 11 films. The scan rate was 5 mVsec^{-1}.

4.3.2. Annealed Cuprous Oxide Films from pH 9 Bath

A. Effect of Annealing Temperatures

The photoelectrochemical measurements for the annealed pH 9 films are presented in Fig 4.7. The measurements were under -0.3 V in constant illumination for 1 h. The average photocurrents for the annealed Cu_2O are summarized from the potentiostatic measurements, and presented in Fig 4.7b. The average currents were 10.19, -23.78, -22.72, -33.58, and -72.27 μAcm^{-2} for pH 9 films annealed at 150, 200, 250, 300, and 350 ℃ for 30 min, respectively. The average current for the as-deposited pH 9 film was -28.59 μAcm^{-2}. The photocurrent of pH 9 films after annealing increased as the annealing temperature was increased. Although, at first the film annealed at 150 ℃ reveled no p-type character. The photocurrent presented in Fig 4.7a displayed a very unstable current which fluctuated strongly. However, the performances for the annealed pH 9 films were enhanced by annealing temperature. The resistivity of the annealed pH 9 films was decreased as the annealing temperature was increased, which agreed with the photocurrents. We assumed that the film annealed at 150 ℃ produced a damaged interface between the Cu_2O and stainless steel. As the temperature was increased, the contact at the interface may be reconstructed by inter diffusion. The film annealed at the highest temperature, 350℃, revealed the best performance.

B. Effect of Annealing Time

In Fig 4.8, we summarized the pH 9 films annealed at different temperatures for 10, 30, and 60 min, respectively. Their results exhibited similar curves like before.

They both became worse at the temperature 150 ℃ and then the photocurrents were increased as the temperature was increased. The annealing effect at 150 ℃ did not show any improvement but more damages. We assumed that the contact of Cu_2O annealed at 150 ℃ became poor. However, the crystallinity was only slightly improved. The interface may reconstruct by diffusion at higher temperatures. The average current densities for all samples are summarized in Table 4.1. The annealed pH 9 film became better as the temperature was increased, implying that the annealing process was effectively improving the crystallinity and conductivity. The results agreed with what we confirmed in the chapter 3.

a)

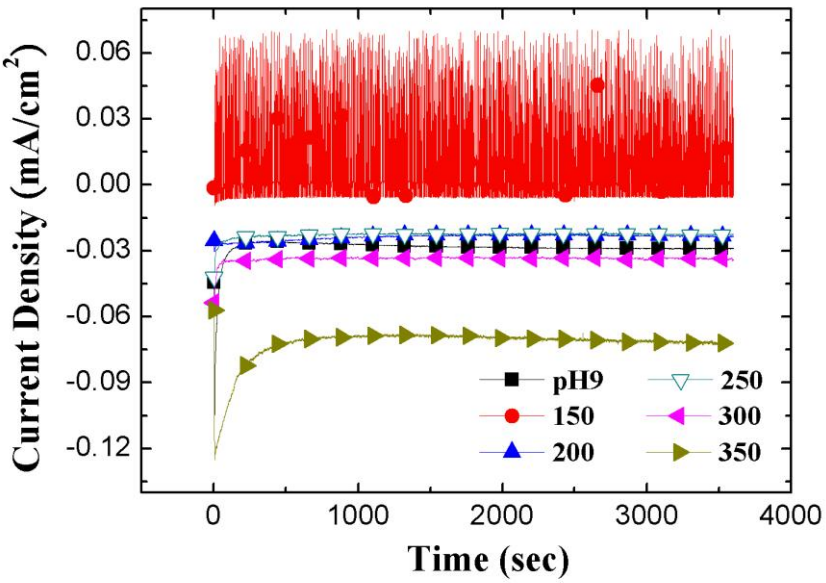

b)

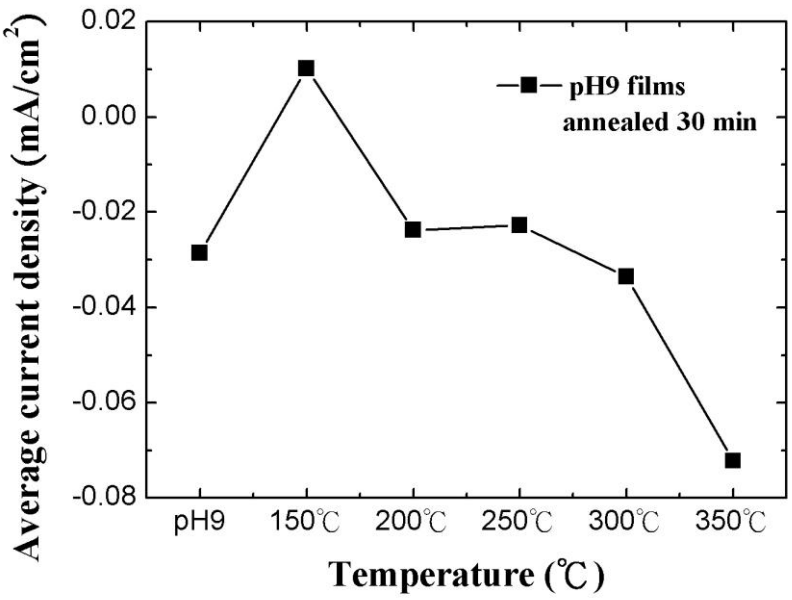

Figure 4.7 a) I-t curves and b) average current density of pH 9 films annealed at different temperatures for 30 min under potentiostatic measurements at -0.3 V and illumination for 1 h.

Table 4.1 Average current density (μAcm^{-2}) of pH 9 annealed at different temperatures and annealing times under potentiostatic measurements at -0.3 V and illumination for 1 h.

Time	150 ℃	200 ℃	250 ℃	300 ℃	350 ℃
10 min	7.53	-10.98	-13.02	-21.40	-51.69
30 min	10.19	-23.78	-22.72	-33.58	-72.27
60 min	3.48	-11.19	-25.94	-28.40	-141.13

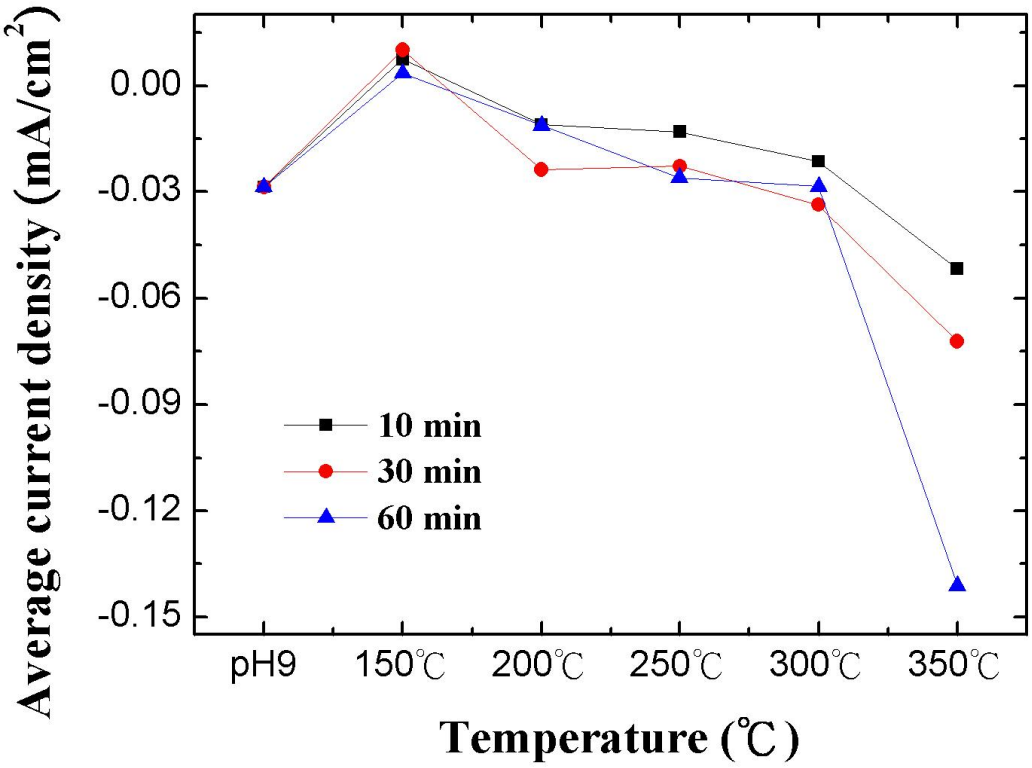

Figure 4.8 Average current density of pH 9 annealed at different temperatures and annealing times under potentiostatic measurements at -0.3 V and illumination for 1 h.

4.3.3. Annealed Cuprous Oxide Film from pH 11 Bath

A. Effect of Annealing Temperatures

The photoelectrochemical measurements for the pH 11 films annealed for 30 min are presented in Fig 4.9. The average photocurrents were -81.7, -32.5, -53.7, -41.2, and -66.7 μAcm^{-2} for pH 11 films annealed from 150 to 350 ℃, respectively (Fig 4.9b). The photocurrent for the as-deposited pH 11 film was -60.9 μAcm^{-2}. These values did not increase as the temperature was increased and it was not a steady trend.

The trend displayed a rocky curve, which revealed the best performance at 150 ℃. However, from the results of Chapter 3, we had realized that the pH 11 samples had a special trend after annealing. The resistivity for the pH 11 Cu_2O films was increased as the temperature was increased to 300 ℃, then abruptly decreased at temperature up to 350 ℃. And its grain size was decreased as the temperature was increased. However, the photocurrent exhibited neither trend of resistivity nor grain size. At this moment, we could not conclude the trend for the annealing effect yet. After all, the photoelectrochemical performance reflected the quality of the Cu_2O films.

B. Effect of Annealing Time

In Fig 4.10, we present the pH 11 films annealed at different temperatures and annealing times, and the average current densities are summarized in Table 4.2. These results presented a similar curve like time effect. According to the results of Chapter 3, the pH 11 films after annealing went through a structural transition. The resistivity was getting worse as the annealing time was increased except at 350 ℃ (Fig 3.21). The grain size was also decreased after annealing. Again, we could not conclude how the re-crystallization would affect on their photoelectrochemical properties yet. However, the degree of the resistivity reduction was not as much as the resistivity improvement of pH 9 films. In fact, the worst conductivity of pH 11 film annealed at 300 ℃ was still better than the pH 9 film annealed at the temperature less than 300 ℃. The results indicated we could not conclude the annealing effect on pH 11 film yet. The variation of photocurrent was negligible. However, the trend for the photocurrent revealed a slight decrease at 300 ℃ and then increased again at 350 ℃, which agreed with the resistivity of annealed pH 11 films.

a)

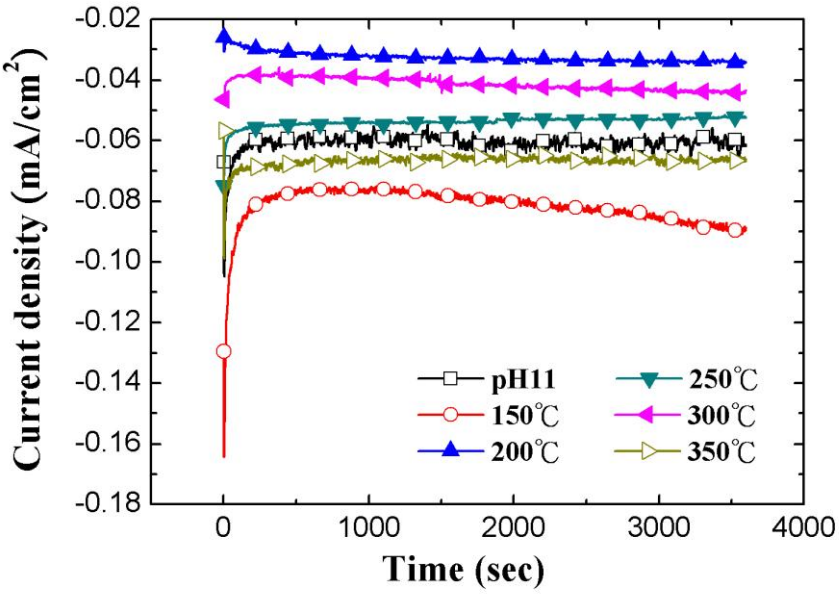

b)

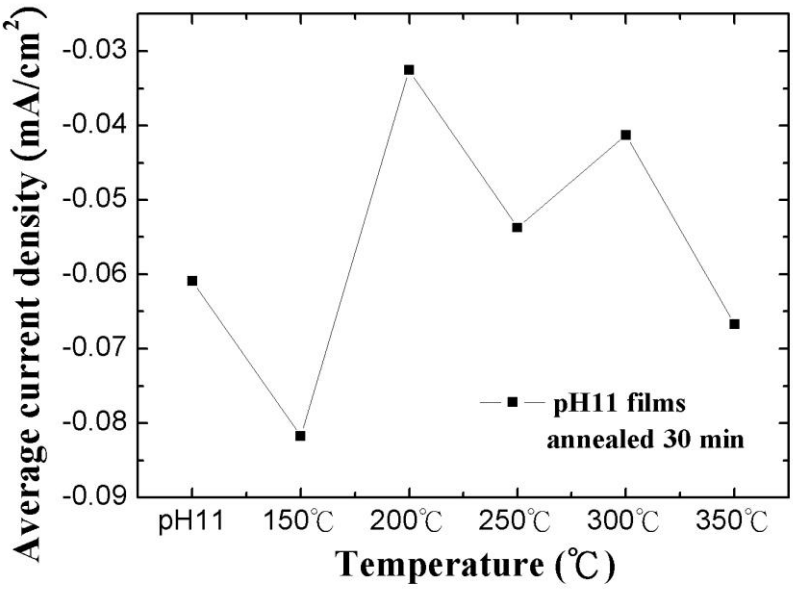

Figure 4.9 a) I-t curves and b) The average current density of pH 9 annealed at different temperatures for 30 min under potentiostatic measurements at -0.3 V and illumination for 1 h.

Table 4.2 Average current density (μAcm^{-2}) of pH 11 annealed at different temperatures and annealing times under potentiostatic measurements at -0.3 V and illumination for 1 h.

Time	150 ℃	200 ℃	250 ℃	300 ℃	350 ℃
10 min	-47.20	-29.70	-26.79	-13.01	-51.83
30 min	-81.75	-32.54	-53.73	-41.24	-66.71
60 min	-61.12	-32.79	-53.44	-55.22	-119.03

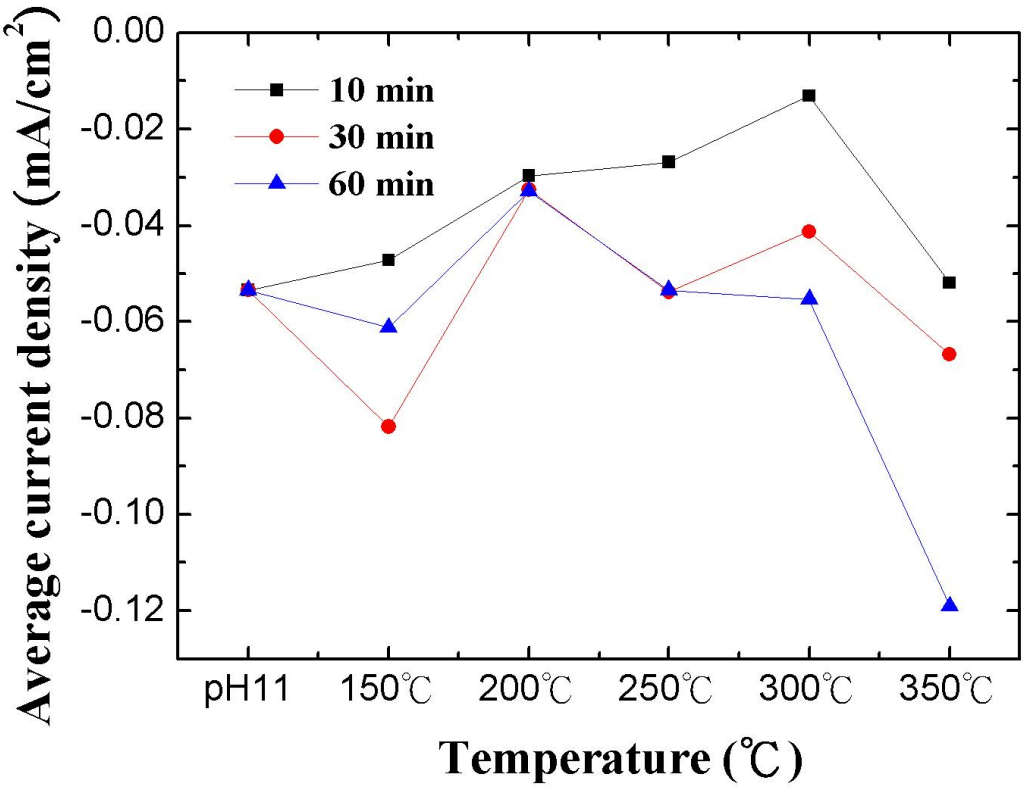

Figure 4.10 Average current density of pH 11 annealed at different temperatures and annealing times under potentiostatic measurements at -0.3 V and illumination for 1 h.

4.4. Materials Characterizations after

We examined the Cu_2O films after photoelectrochemical reactions by XRD (Fig 4.11). We did not found any impurity after light illumination for 1 h. As we concluded previously, the Cu_2O was stable in our system.

However, we did find evidence of transformation after reaction from the pH 11 films annealing at 350 ℃ for 60 min, as shown in SEM images (Fig 4.12). We observed that there were small cubes appeared on the surface. Because we did not observe any impurity from the XRD patterns, we assumed these cubes were possibly still Cu_2O. There appearance was similar to those from chemical route. These cubes implied that the Cu_2O could re-crystallize at the surface. This behavior has not been mentioned in previous studies.

The phenomenon was only observed on pH 11 films undergoing annealing at 300 ℃ for 30 and 60 min, and films annealed at 350 ℃ for 30 and 60 min after photoelectrochemical measurements. This indicated that it only occurred on the pH 11 films after annealing at high temperature, but did not take place on the pH 9 films. The surface of pH 9 annealed at 350 ℃ for 60 min after reaction is displayed in Fig 4.13.

Photoelectrochemical measurements with and without illumination on pH 11 films which annealed at 350 ℃ for 60 min were conducted, with SEM images shown in Fig 4.14. We prepared the films before and after illumination for 10 min. The results demonstrated that after illumination for 10 min we could find small cubes formed on the surface, indicating that the reaction at the surface became re-crystallized. On the other hand, the film without illumination (Fig 4.15) did not reveal any transformations for 30 min. We prolonged the reaction to 150 min, and the result is presented in Fig 4.15c. The films appeared destructed after reaction by

forming new compounds. We examined the films after 150 min without illumination by XRD (Fig 4.16) and the results confirmed the presence of Cu.

Our results implied that only the films under illumination would form cubes on the surface. Otherwise the Cu was reduced by the overpotential. However, both phenomenons were observed on the films after annealing at high temperature. We did not observe any cube or Cu formation on the as-deposited Cu_2O films (Fig 4.3 and 4.4). It implied that the surface of Cu_2O film after annealing might be more active. The pH value of 0.5 M Na_2SO_4 was 6.5. According to the pourbaix diagram (Fig 4.17), under -0.3 V (vs. Ag/AgCl) the Cu_2O would be reduced to Cu. It could be the reason that we observed Cu formation at films without illumination. On the other hand, the cubes formation on the surface could be caused by the re-crystallization of Cu_2O. However, the exact nature of this cube formation is unknown.

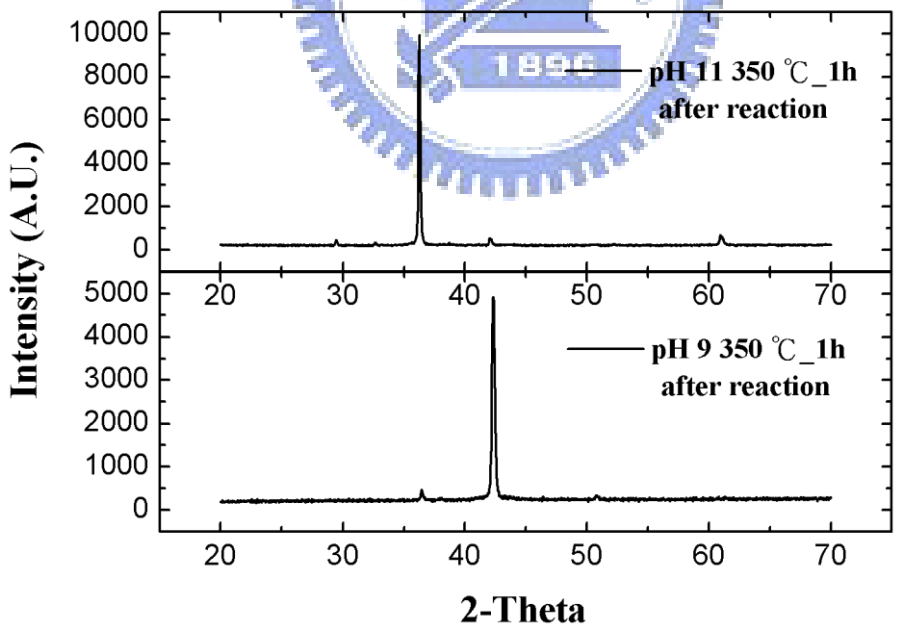

Figure 4.11 XRD patterns of pH 9 and pH 11 films which were both annealed at 350 ℃ for 1 h and after photoelectrochemical measurements of illumination for 1 h with -0.3 V.

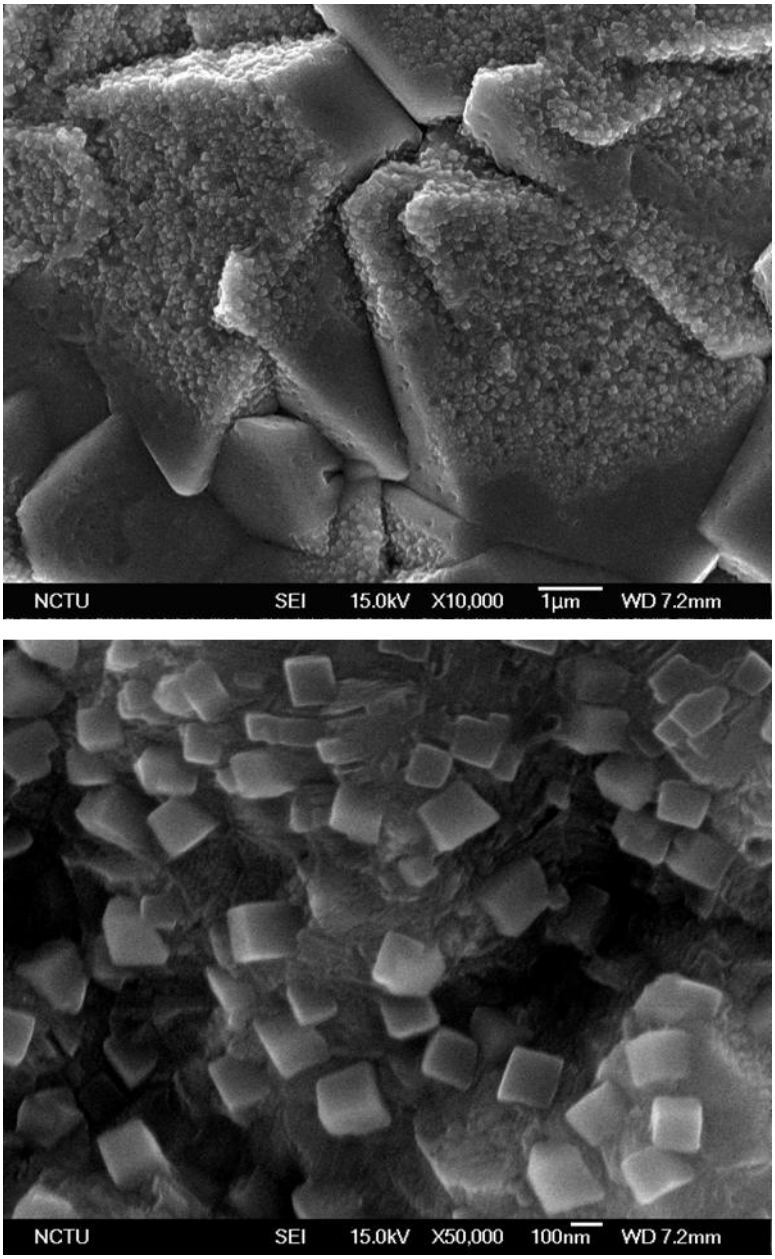

Figure 4.12 SEM images of pH 11 film which was annealed at 350 ℃ for 1 h and after a photoelectrochemical measurement of illumination for 1 h under -0.3 V. The second image is a magnified view of the surface.

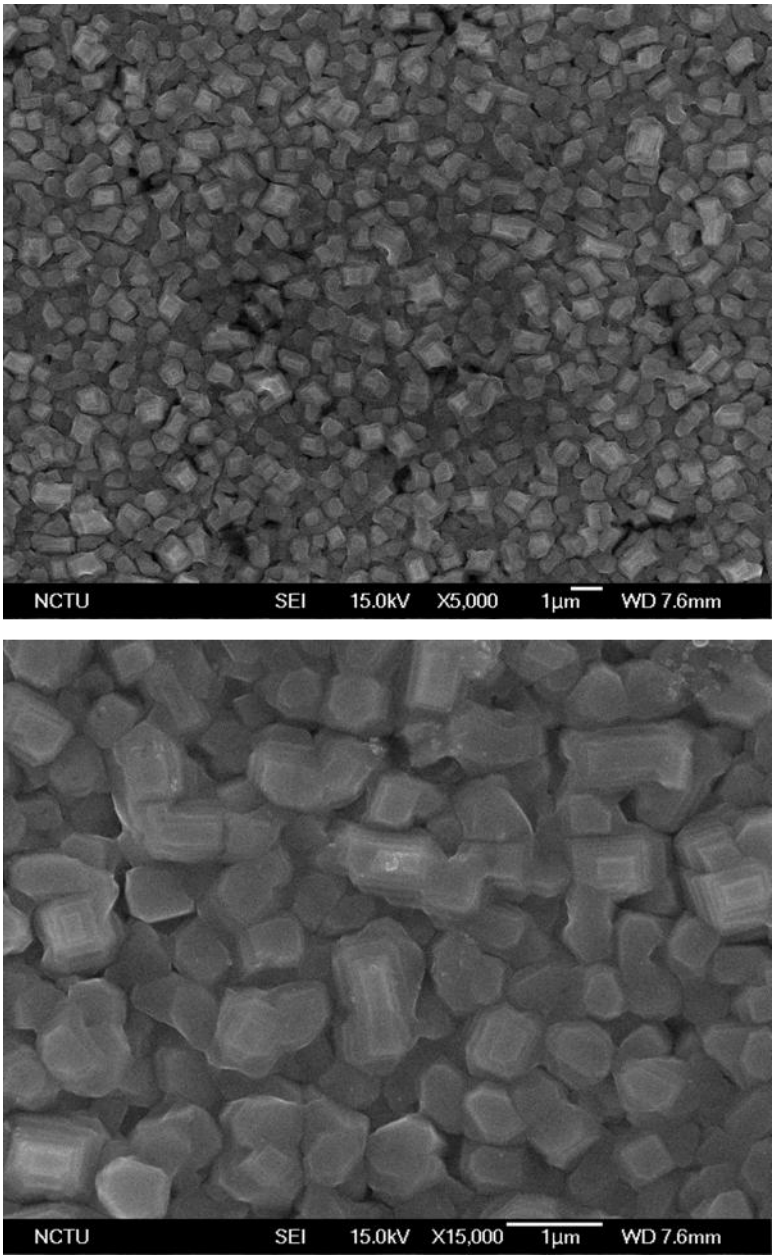

Figure 4.13 SEM images of pH 9 film which was annealed at 350 ℃ for 1 h and after a photoelectrochemical measurement of illumination for 1 h under -0.3 V. The second image is a magnified view of the surface.

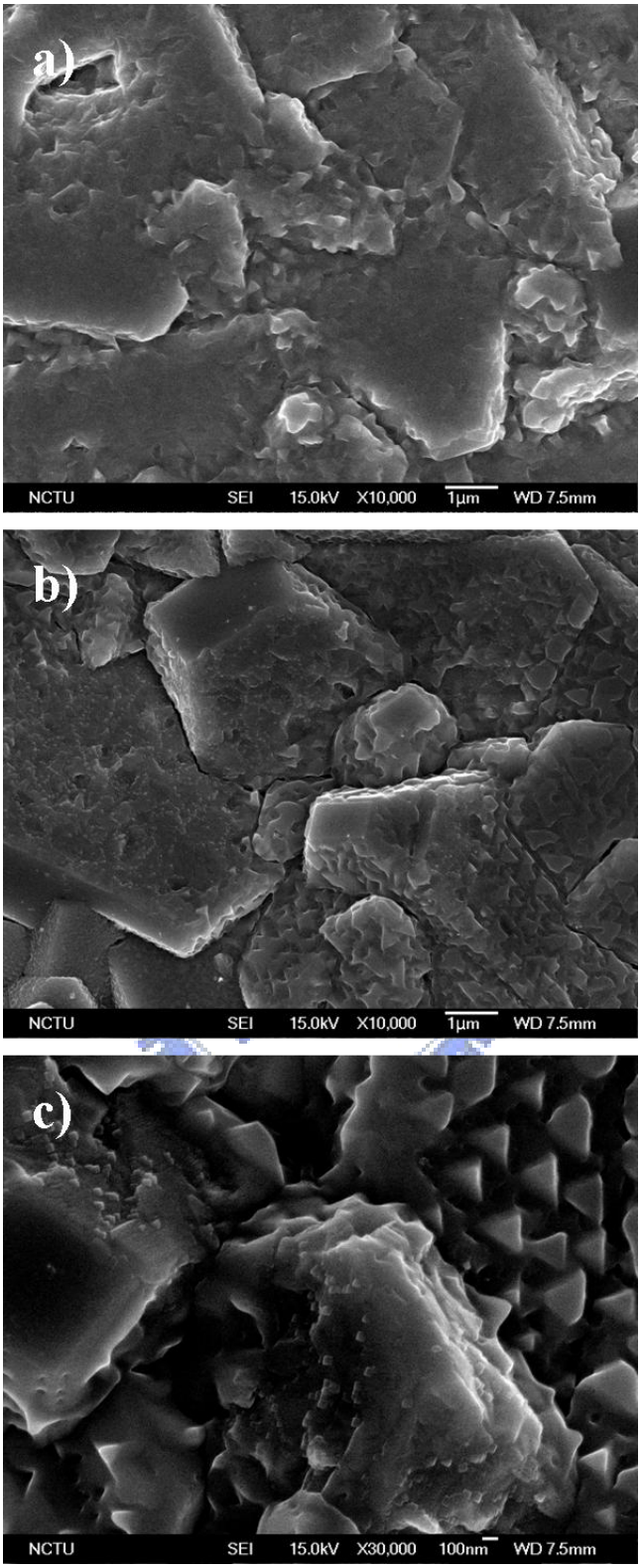

Figure 4.14 SEM images on the surface of pH 11 film which was annealed at 350 ℃ for 1 h; a) after annealing, b) after photoelectrochemical measurement for 10 min illumination under -0.3 V, and c) a magnified view of (b).

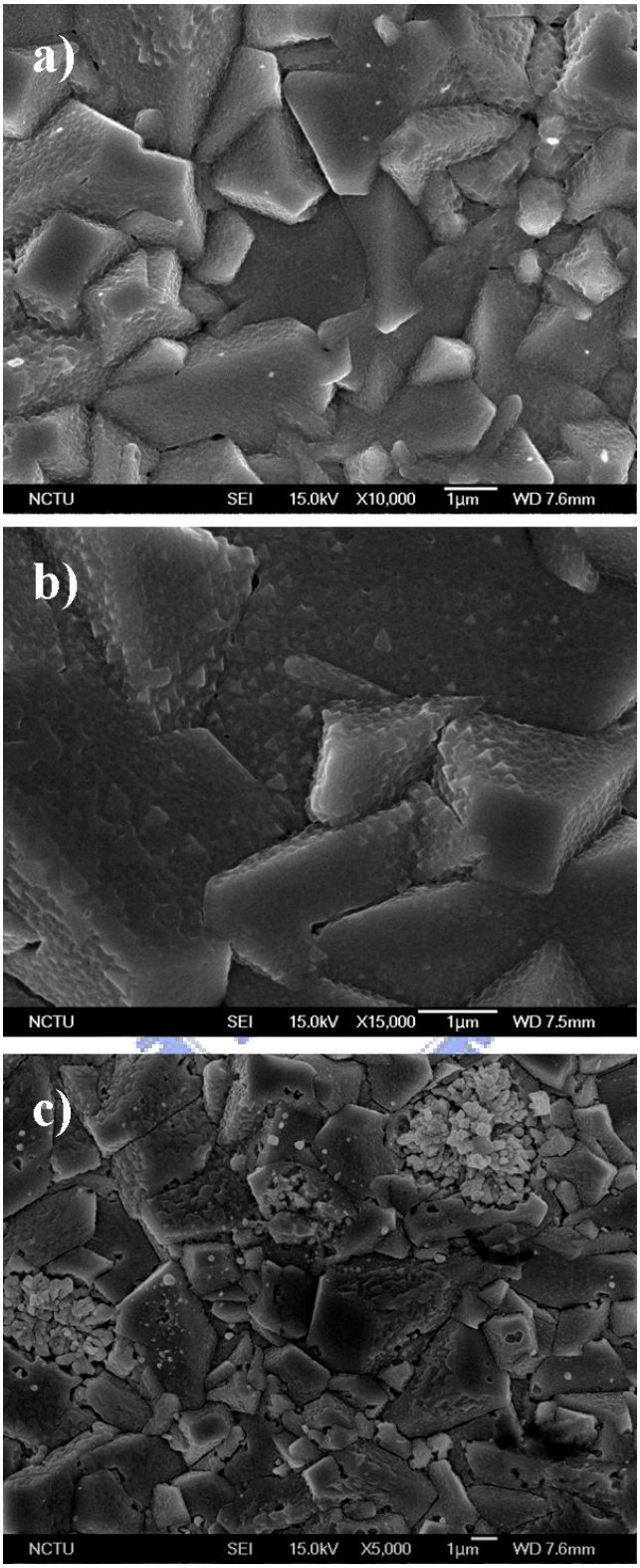

Figure 4.15 SEM images on the surface of pH 11 film which was annealed at 350 ℃ for 1 h; a) after annealing, b) after photoelectrochemical measurement for 30 min without illumination under -0.3 V, and c) after photoelectrochemical measurement for 150 min without illumination under -0.3 V.

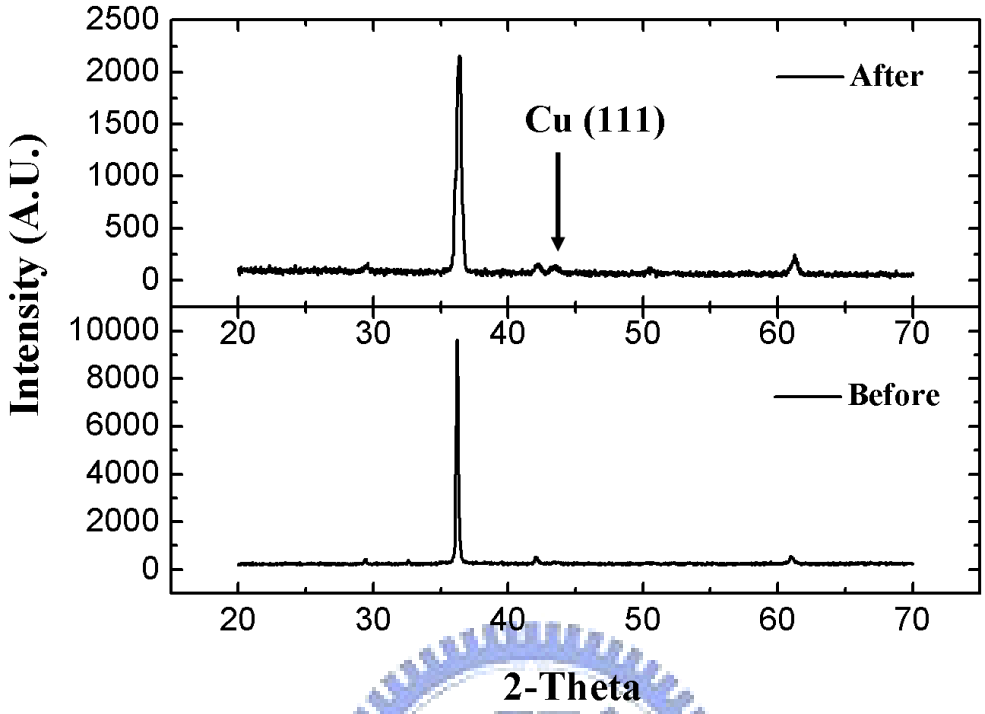

Figure 4.16 XRD patterns of pH 11 film which was annealed at 350 ℃ for 1 h before and after photoelectrochemical measurement for 150 min without illumination under -0.3 V.

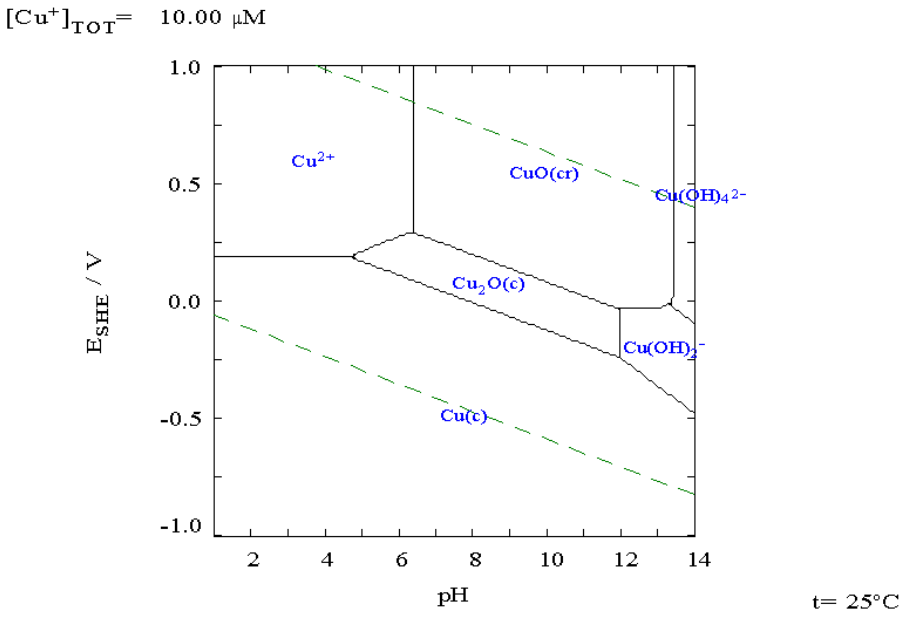

Figure 4.17 Pourbaix diagram of Cu_2O.

4.5. Conclusions

The as-deposited pH 9 film revealed poor conductivity before the annealing process. The conductivity after annealing was as good as the pH 11 films. The improvement was also confirmed by the photocurrent. The results suggested that the resistivity of Cu_2O film was the primary factor affecting its photoelectrochemical properties. After all, the annealing process was an effective treatment to improve the crystallinity of Cu_2O.

References

[1] Rakhshani AE. Preparation, characteristics and photovoltaic properties of cuprous oxide-a review. Solid-State Electronics. 1986;29(1):7-17.

[2] Yin M, Wu CK, Lou Y, Burda C, Koberstein JT, Zhu Y, O'Brien S. Copper oxide nanocrystals. J Am Chem Soc. 2005;127:9506-9511.

[3] Zhang J, Liu J, Peng Q, Wang X, Li Y. Nearly Monodisperse Cu_2O and CuO nanospheres: preparation and applications for sensitive gas sensors. Chem Mater. 2006;18:867-871.

[4] Gou L, Murphy CJ. Controlling the size of Cu_2O nanocubes from 200 to 25 nm. J Mater Chem. 2004;14:735-738.

[5] Kuo CH, Chen CH, Huang MH. Seed-mediated synthesis of monodispersed Cu_2O nanocubes with five different size ranges from 40 to 420 nm. Adv Funct Mater. 2007;17:3773-3780.

[6] Yang Z, Chiang CK, Chang HT. Synthesis of fluorescent and photovoltaic Cu_2O nanocubes. Nanotechnology. 2008;19:025604.

[7] He P, Shen X, Gao H. Size-controlled preparation of Cu_2O octahedron nanocrystals and syudies on their optical absorption. J Colloid Interface Sci. 2005;284:510-515.

[8] Xu H, Wang W, Zhu W. Shape evolution and size controllable synthesis of Cu_2O octahedral and their morphology dependent photocatalytic properties. J Phys Chem B. 2006;110:13829-13834.

[9] Wang W, Wang G, Wang X, Zhan Y, Liu Y, Zheng C. Synthesis and characterization of Cu_2O nanowires by a novel reduction route. Adv Mater. 2002;14(1):67-69.

[10] Cao M, Hu C, Wang Y, Guo Y, Guo C, Wang E. A controllable synthetic route to cu, Cu_2O, and CuO nanotubes and nanorods. Chem Commun. 2003:1884-1885.

[11] Paunovic M, Schlesinger M. Fundamentals of Electrochemical Deposition. John Wiley & Sons. 2006

[12] Pandey RK. Handbook of Semiconductor Electrodeposition. Marcel Dekker. 1996

[13] Zhou Y, Switzer JA. Electrochemical deposition and microstructure of copper (I) oxide films. Scripta Materialia. 1998;38(11):1731-1738.

[14] Liu R, Oba F, Bohannan EW, Ernst F, Switzer JA. Shape control in epitaxial electrodeposition: Cu_2O nanocubes on InP(001). Chem Mater. 2003;15:4882-4885.

[15] Joseph S, Kamath PV. Electrodeposition of Cu_2O coatings on stainless steel substrates. J Electrochem Soc. 2007;154(7):E102-E106.

[16] Barton JK, Vertegel AA, Bohannan EW, Switzer JA. Epitaxial electrodeposition of copper(I) oxide on sigle-crystal copper. Chem Mater. 2001;13:952-959.

[17] Wang LC, de Tacconi NR, Chenthamarakshan CR, Rajeshwar K, Tao M. Electrodeposited copper oxide films: Effect of bath pH on grain orientation and orientation-dependent interfacial behavior. Thin Solid Films. 2007;515:3090-3095.

[18] Lee J, Tak Y. Electrochemical deposition of a single phase of pure Cu_2O films by current modulation methods. Electrochem Solid St. 2000;3(2):69-72.

[19] Huang L, Wang H, Wang Z, Mitra A, Zhao D, Yan Y. Cuprite nanowires by electrodeposition from lyotropic reverse hexagonal liquid crystalline phase. Chem Mater. 2002;14:876-880.

[20] Siegried MJ, Choi KS. Electrochemical crystallization of cuprous oxide with systematic shape evolution. Adv Mater. 2004;16(19):1743-1746.

[21] Siegried MJ, Choi KS. Directing the architecture of cuprous oxide crystals during electrochemical growth. Angew Chem Int Ed. 2005;44:3218-3223.

[22] Siegried MJ, Choi KS. Elucidating the effect of additives on the growth and stability of Cu_2O surfaces via shape transformation of pre-grown crystals. J Am Chem Soc. 2006;128:10356-10357.

[23] Sun F, Guo Y, Song W, Zhao J, Tang L, Wang Z. Morphological control of Cu_2O micro-nanostructure film by electrodeposition. Journal of Cryst Growth. 2007;304:425-429.

[24] Schiavello M. Photoelectrochemistry, Photocatalysis and Photoreactors Fundamentals and Developments. D Reidel. 1985

[25] Pleskov YV, Gurevich. Semiconductor Photoelectrochemistry. Plenum. 1985

[26] Bard AJ, Fox MA. Artificial photosynthesis: solar splitting of water to hydrogen and oxygen. Acc Chem Res. 1995;28:141-145.

[27] Hara M, Kondo T, Komoda M, Ikeda S, Shinohara K, Tanaka A, Kondo JN, Domen K. Cu_2O as a photocatalyst for overall water splitting under visible light irradiation. Chem Commun. 1998:357-358.

[28] de Jongh PE, Vanmaekelbergh D, Kelly JJ. Cu_2O: a catalyst for the photochemical decomposition of water? Chem Commun. 1999:1069-1070.

[29] Somasundaram S, Chenthamarakshan CRN, de Tacconi NR, Rajeshwar K. Photocatalytic production of hydrogen from electrodeposited p-Cu_2O film and sacrificial electron donors. Int J Hydrogen Energy. 2007;32:4661-4669.

[30] Nian JN, Hu CC, Teng H. Electrodeposited p-type Cu_2O for H_2 evolution from photoelectrolysis of water under visible light illumination. Int J Hydrogen

Energy. 2008;33:2897-2903.
[31] Kakuta S, Abe T. Structural characterization of Cu_2O after the evolution of H_2 under visible light irradiation. Electrochem Solid St. 2009;12(3):1-3.
[32] Han X, Han K, Tao M. n-Type Cu_2O by electrochemical doping with Cl. Electrochem Solid St. 2009;12(4):H89-H91.
[33] McShane CM, Choi KS. Photocurrent enhancement of n-type Cu_2O electrodes achieved by controlling dendritic branching growth. J Am Chem Soc. 2009;131:2561-2569.